CONTRAST ENHANCEMENT AND ARTIFACT REDUCTION IN STEADY-STATE MAGNETIC RESONANCE IMAGING

A DISSERTATION

SUBMITTED TO THE DEPARTMENT OF ELECTRICAL ENGINEERING

AND THE COMMITTEE ON GRADUATE STUDIES

OF STANFORD UNIVERSITY

IN PARTIAL FULFILLMENT OF THE REQUIREMENTS

FOR THE DEGREE OF

DOCTOR OF PHILOSOPHY

Neal Kepler Bangerter

August 2004

I certify that I have read this dissertation and that, in my opinion, it is fully adequate in scope and quality as a dissertation for the degree of Doctor of Philosophy.

Dwight G. Nishimura
(Principal Advisor)

I certify that I have read this dissertation and that, in my opinion, it is fully adequate in scope and quality as a dissertation for the degree of Doctor of Philosophy.

John M. Pauly

I certify that I have read this dissertation and that, in my opinion, it is fully adequate in scope and quality as a dissertation for the degree of Doctor of Philosophy.

Garry E. Gold

Approved for the University Committee on Graduate Studies:

Abstract

Magnetic resonance imaging (MRI) is a noninvasive and highly flexible medical imaging technique that yields excellent soft tissue contrast. Unlike x-ray imaging methods, such as x-ray CT, MRI does not rely on ionizing radiation for image generation. Images are instead formed by measuring the radio-frequency signal of excited nuclear spins in the presence of a strong homogenous polarizing magnetic field. A set of weaker switched gradient magnets produces time-varying magnetic fields that aid in spatial localization for image formation.

The past decade has seen significant improvements in the gradient hardware available for MRI. Newer gradient sets can produce higher fields than their predecessors, and ramp on and off much more rapidly. These advances have made feasible a class of steady-state MRI techniques that were formerly impractical. Fully-refocused, or balanced, steady state free-precession (SSFP) MRI yields high signal-to-noise ratio (SNR) images in very short scan times, and is consequently a topic of considerable current research. Balanced SSFP imaging shows promise for a broad range of applications, including simple 2D and 3D anatomical imaging, real-time cardiac MRI, and peripheral angiography.

One drawback of balanced SSFP imaging is its high sensitivity to magnetic field inhomogeneity. Severe image artifacts result if the magnetic field variations are too large across the body to be imaged. Several methods have been proposed which combine data from multiple "phase-cycled" SSFP images to eliminate this sensitivity. A statistical analysis framework for studying the SNR characteristics of these methods is described in this dissertation, and an alternate combination method introduced.

The new technique yields significantly higher SNR than the other methods while achieving good image artifact reduction.

The past decade has also seen the introduction of several steady-state "catalyzation" methods which, when combined with certain magnetization-preparation techniques, aid in the manipulation of SSFP contrast. This dissertation presents some new applications of magnetization-prepared SSFP imaging to CSF-suppressed neurological imaging. Specifically, a fast 2D multi-slice fluid-suppressed SSFP technique is presented, and *in vivo* results are shown in the human brain.

Another promising application of balanced SSFP imaging is in peripheral angiography. To accurately depict the vessels of the lower leg, foot, or hand, the typically bright MR signals from lipid (such as bone marrow) and fluid (such as synovial fluid) need to be suppressed. Signal independence of blood flow velocities, good arterial/muscle contrast, and arterial/venous separation are also desirable. This dissertation presents a novel magnetization-prepared 3D SSFP technique for fat- and fluid-suppressed peripheral angiography. High SNR flow-independent MR angiograms with excellent blood/muscle contrast and arterial/venous separation are achieved in very short scan times with the new technique.

Acknowledgments

When I arrived at Stanford almost six years ago, I was excited at the prospect of working towards a Ph.D., but had given very little thought to what my research area might be. During my first year, I was fortunate enough to stumble upon EE 369B, taught that quarter by John Pauly. I loved the course, and soon learned that the grad student (so I had assumed) who took over while John was out of town for a couple of lectures was Dwight Nishimura–a name I was familiar with from the cover of my course book. By the end of the subsequent quarter, I had joined Dwight's research group (and was no longer mistaking him for a grad student).

I don't believe I could have been more fortunate in my choice of research area or group. The last six years have been a tremendous experience. I have made lifelong friends, worked on fascinating projects with amazing people, and thoroughly enjoyed myself in the process. I am reluctant to attempt to name all of those people who have contributed to making MRSRL such a great place, as I would certainly miss some. Instead, I acknowledge and thank all of those I've worked and interacted with over the last six years. You have all contributed to make my experience at Stanford a rewarding one.

I gratefully acknowledge my fellow students in the group, from whom I have learned a great deal. They are too numerous to name here, so I thank all of the old, present, and new "labguys", as well as the Packard crowd. I will, however, single out Brian Hargreaves and Shreyas Vasanawala. Brian has been somewhat of a mentor to me during my time at Stanford. He has tirelessly helped me talk through research issues, lent valuable insights, and pointed me in the right direction. Shreyas is also

responsible for much of the direction my research has taken, and I'm thankful to have been able to build on some of the work he did.

I am grateful to my defense and reading committee members: Tony Fraser-Smith, Dwight Nishimura, John Pauly, Garry Gold, and Al Macovski. All of them have been valuable advisors and collaborators. I owe special thanks to Garry, who has the added distinction of having saved my ankle from a potentially debilitating disease. I also wish to thank Steve Conolly and Bob Hu for many valuable and enjoyable discussions.

I'd be remiss if I didn't single out Dwight and John once again. Dwight has advised, counseled, taught, and put up with me during my time at Stanford. He is universally liked and respected, both by his colleagues and by his students. I have found this reputation to be very well deserved, and consider myself lucky to have worked with him. I thank John for sparking my interest in MRI, and constantly challenging me with new ideas and insights.

Financial support for my work at Stanford has come from a number of sources. I thank GE Medical Systems, the Stanford Graduate Fellowship Program, William K. Bowes Jr., and the National Institute of Health.

I would not have had the opportunity to be at Stanford were it not for the support and love of my family. Mom and Dad have provided me with a love of education and ample opportunities to pursue my dreams, and I thank them for all they've done for me. My children Tanner, Joel, and Seth have provided me with happiness and a welcome diversion when I come home. I am deeply grateful to my wife Lee for her companionship, support, encouragement, and love throughout.

Lastly, I thank God for the blessings in my life that have allowed me to have this wonderful experience at Stanford.

NEAL KEPLER BANGERTER
Mercer Island, WA
May 6, 2004

Contents

x

List of Tables

List of Figures

Chapter 1

Introduction

The twentieth century saw incredible advances in the ability to form images of the living human body. Roentgen's discovery of x-rays in 1895 and his subsequent use of them to form the first x-ray (an image of his wife Bertha's hand, wearing a ring) in November of 1895 ushered in the era of medical imaging. So powerful and useful was the new technology that x-rays were already being used clinically in the United States less than a year after their discovery in Germany.

Throughout the last century, x-ray techniques have been expanded and improved. Today, almost every hospital in the world can perform simple plain-film anatomical x-rays, and computerized x-ray tomography (x-ray CT) has further expanded the range of x-ray imaging applications. Advances in beam and sensor technology have also improve x-ray CT soft-tissue contrast. Other techniques using ionizing radiation, such as positron emission tomography (PET) and single photon emission computed tomography (SPECT), have made their way into clinical usage. Ultrasound, which relies on the diverse reflective properties of different tissues to ultrasonic waves for image formation, has proved invaluable for medical imaging.

The discovery in 1946 of the phenomenon of nuclear magnetic resonance (NMR) in condensed matter by Felix Bloch and Edward Purcell laid the theoretical framework for a new medical imaging technique, commonly referred to as magnetic resonance

imaging (MRI). In 1973, the first anatomical images were obtained by Paul Lauterbur. Over the next decade, the technique was expanded and improved. By the late 1980's, MRI was in widespread clinical usage, and in 2002 more than 60 million MRI examinations were performed worldwide. Felix Bloch and Edward Purcell were awarded the Nobel Prize in Physics in 1952 for their discovery. Paul Lauterbur and Peter Mansfield, another early pioneer in the field, shared the 2003 Nobel Prize in Physiology and Medicine for their contributions to magnetic resonance imaging.

The development of magnetic resonance imaging has been exciting for a number of reasons. First, MRI does not make use of ionizing radiation, and is completely non-invasive. Imaging relies on a strong uniform polarizing magnetic field, smaller "gradient" magnetic fields, and radio-frequency magnetic fields, none of which damages the tissues of the body. Furthermore, many different imaging parameters and methods are available to change image contrast. Excellent soft-tissue anatomical contrast can be obtained, as well as images of metabolic activity and even blood flow velocities.

One of the drawbacks of many magnetic resonance imaging techniques is the length of time needed to acquire an image. Patient comfort and the ability to maintain a stationary position can be concerns during long scans. Likewise, magnet utilization costs can be significant. In addition to research on new contrast generation mechanisms, significant effort has been expended in speeding up image acquisition. A major limiting factor in MRI acquisition speed is the switching speed and power of the gradient magnet hardware. The past decade has seen significant improvements in this hardware. Newer gradient sets can produce higher fields than their predecessors, and ramp on and off much more rapidly. These advances have made feasible a class of steady-state MRI techniques that was formerly impractical: fully-refocused, or balanced, steady-state free-precession (SSFP) MRI. Balanced SSFP MRI is capable of yielding high signal-to-noise ratio (SNR) images in very short scan times, and shows promise for a broad range of applications. The development, improvement, and analysis of balanced SSFP techniques is consequently a very active field of current research, and is the primary focus of this dissertation.

The organization of this work is as follows:

Chapter 2: Magnetic Resonance Imaging Fundamentals

This chapter provides a general background of the theoretical basis for magnetic resonance imaging. While no attempt is made to be exhaustive, enough of the fundamental concepts essential to magnetic resonance imaging are covered to provide a basic foundation for the work that follows. These include the concepts of polarization, spin precession, excitation, relaxation, and MR signal generation and detection. Frequency encoding, phase encoding, and contrast generation mechanisms are also briefly introduced, along with a discussion of image noise.

Chapter 3: Steady-State Free Precession (SSFP)

As stated, this work concerns itself primarily with the development, improvement, and analysis of a broad class of MRI methods known as balanced steady-state free precession, or SSFP. This chapter builds on the fundamental concepts of MRI presented in Chapter 2, and describes the characteristics of fully-refocused SSFP sequences. In particular, those aspects of SSFP imaging relevant to the chapters that follow are given special attention. These include SSFP off-resonance spectra and the origin of banding artifacts, phase-cycling, transient signal evolution, steady-state catalyzation, and oscillating-equilibrium SSFP.

Chapter 4: Multiple-Acquisition SSFP

Balanced SSFP sequences may suffer from severe banding artifacts arising from magnetic field inhomogeneity. While several methods have been proposed to eliminate these artifacts, it is of great practical importance to consider the SNR performance of each method, as well as each method's effectiveness at removing banding artifacts. In this chapter, a new method for eliminating banding artifact in SSFP is proposed. A detailed analysis of the SNR characteristics, banding artifact reduction, and contrast of each method is also presented.

Chapter 5: 2D Fluid-Attenuated Inversion Recovery SSFP

Fluid-attenuated neuroimaging techniques are helpful in detecting lesions on the human brain. In this chapter, a fast new method of acquiring fluid-suppressed brain images is presented and analyzed. The sequence combines inversion-recovery (IR) prepared SSFP for fluid suppression and the sum-of-squares technique introduced in Chapter 4 for eliminating banding artifacts. High SNR anatomical images, acquired very rapidly, are shown in both the normal brain and a patient with multiple sclerosis.

Chapter 6: 3D Flow-Independent Peripheral Angiography with SSFP

To accurately depict the vessels of the lower leg, foot, or hand, bright MR signal from lipid (such as bone marrow) and long-T1 fluid (such as synovial fluid and edema) needs to be suppressed. Signal independence on blood flow velocities, good arterial/muscle contrast, and arterial/venous separation are also desirable. A new magnetization-prepared 3D SSFP sequence for flow-independent peripheral angiography is presented in this chapter. The technique combines a number of component techniques (phase-sensitive fat detection, IR, T2-Prep, square-spiral phase-encode ordering) to achieve excellent peripheral angiograms in very short scan times. Each technique is described, and results presented in the lower leg and foot.

Chapter 7: Summary and Recommendations

The contributions presented in this dissertation are briefly summarized, and recommendations for future work in each area outlined.

Chapter 2

Magnetic Resonance Imaging Fundamentals

The aim of this chapter is to provide a brief review of the fundamental concepts and physics that make magnetic resonance imaging possible. Emphasis has been placed on presenting an intuitive overview of the basic concepts, rather than on developing a rigorous mathematical framework for MRI. There are several books on the subject that provide mathematical treatments of magnetic resonance imaging [1,2], and the interested reader is referred to these. Here is presented a brief overview of key concepts adequate for understanding the research presented in this dissertation. Where further mathematical development is required, (i.e., the derivation of transient signal evolution in SSFP imaging), it will be treated in context at the appropriate point. Many of the sections were inspired by the excellent descriptions of MR concepts given in [3].
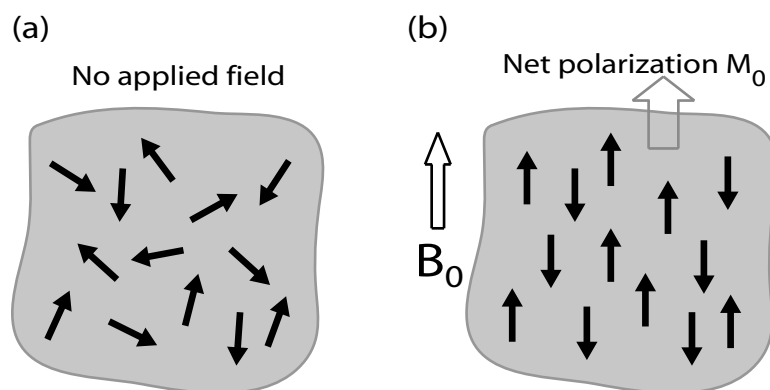
Figure 2.1: In the absence of an external magnetic field, the magnetic moments of hydrogen nuclei are randomly oriented, as shown in (a), and no net polarization is seen across the body. In the presence of a magnetic field $\mathbf{B_0}$, the spins align either parallel or antiparallel to the direction of the applied field, as illustrated in (b). Slightly more spins align in the parallel direction, resulting in a small net magnetization $\mathbf{M_0}$.

2.1 Spin Physics

2.1.1 Polarization

Protons and neutrons possess an inherent quality called spin angular momentum. In an atomic nucleus with an even combined number of protons and neutrons, the net magnetic moment of the nucleus is zero. However, nuclei with an odd combined number of protons and neutrons have an unpaired component of spin angular momentum. This gives rise to a small net magnetic moment: the nucleus acts as a tiny magnetic dipole.

The hydrogen nucleus in its most abundant form contains a single proton, and therefore exhibits a small dipole moment. Hydrogen is very abundant in organic tissue, in the form of water and other organic compounds. It is this happy abundance of hydrogen nuclei that makes magnetic resonance imaging as we know it possible.

Consider a body containing a large number of hydrogen nuclei. In the absence of an external magnetic field, the orientation of the magnetic moment of each nucleus

will be more or less random. Macroscopically, this leads to an internal cancellation of the small moments of each nucleus, and no net polarization is seen across the body. This is illustrated in Figure 2.1a.

However, if a magnetic field $\mathbf{B_0}$ is applied to the body, the spins align either parallel or antiparallel to the field, as shown in Figure 2.1b. The parallel orientation is slightly lower in energy than the antiparallel state. Although spins tend to occupy the lowest energy state available, thermal energy is sufficient to keep the two states almost evenly populated. However, slightly more still tend to align parallel, or longitudinal, to the applied field $\mathbf{B_0}$, and a small net magnetic moment $\mathbf{M_0}$ remains in the direction of $\mathbf{B_0}$.

Going forward, this macroscopic net magnetic moment $\mathbf{M_0}$ across a localized collection of nuclei with similar properties will be termed a "spin". References will often be made to a "spin" of a particular tissue at a particular location. This is a useful simplification: what is actually meant is a collection of nuclei exhibiting a net magnetic moment or polarization. As seen in the figures, this magnetic moment is graphically depicted by an arrow in the direction of polarization.

2.1.2 Precession

Assume now that a spin, in the presence of the polarizing field $\mathbf{B_0}$, is made to point in a direction other than longitudinal to $\mathbf{B_0}$. Classically a torque on the dipole moment (or spin) is expected. The spin begins to precess, or nutate, about the direction of $\mathbf{B_0}$ (the longitudinal direction, or z-axis in the diagrams). This is illustrated graphically in Figure 2.2, and is analogous to a spinning top precessing in a gravitational field.

The frequency at which the spin precesses is linearly proportional to the applied magnetic field, in this case $\mathbf{B_0}$. The proportionality constant relating the applied magnetic field to the frequency of precession is called the *gyromagnetic ratio*, and is denoted by γ. The gyromagnetic ratio is dependent on the type of nucleus. The actual frequency at which a spin precesses is termed the *Larmor frequency.* For a hydrogen nucleus subjected to a polarizing field strength of 1.5 Tesla, the Larmor frequency

(a)   (b)
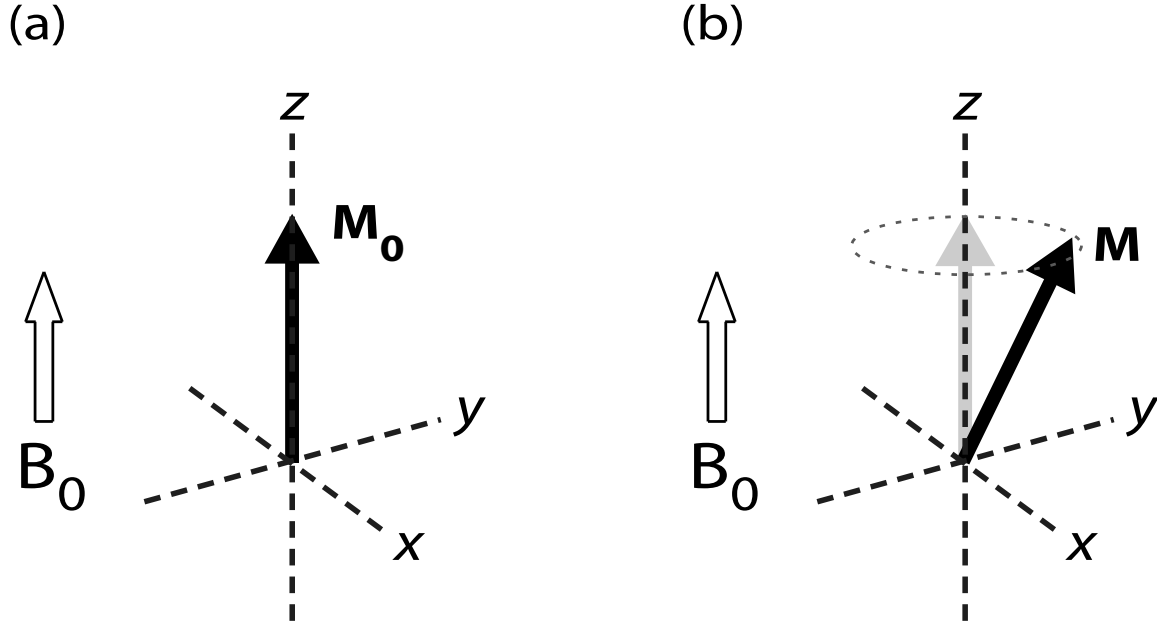
Figure 2.2: (a) In equilibrium, the net magnetization $\mathbf{M_0}$ (or *spin*) is oriented in the direction of the polarizing field $\mathbf{B_0}$. (b) If the spin is caused to move out of its equilibrium position, it begins to precess about the direction of $\mathbf{B_0}$ at the Larmor frequency.

is 63.87 MHz. Most of the results presented in this dissertation were obtained on a magnetic resonance imaging machine with main field strength $\mathbf{B_0}$ of 1.5 T.

2.1.3 Excitation

Spins can be tipped off-axis, or *excited*, by an incident radio-frequency field tuned to the Larmor frequency and polarized in the plane transverse to the direction of $\mathbf{B_0}$. This is illustrated in Figure 2.3a. In the figure, the incident RF wave is polarized in the xy plane. The spin $\mathbf{M}$ exhibits *nuclear magnetic resonance* at the Larmor frequency. The applied radio-frequency field causes the spin to spiral downward, yielding a component of the magnetization in the transverse plane.
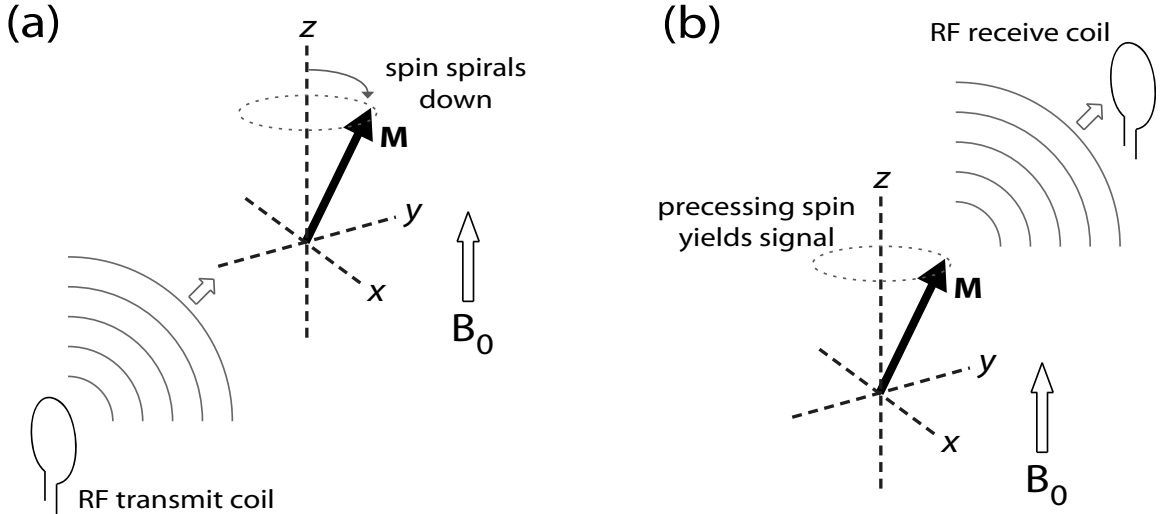
Figure 2.3: (a) A radio-frequency field tuned to the Larmor frequency and polarized in the plane transverse to the direction of $\mathbf{B_0}$ causes the spin to spiral out of its equilibrium position, effectively tipping it out of its equilibrium direction. (b) After the spin is tipped off axis, spin precession leads to a detectable RF signal at the Larmor frequency.

Once tipped, the spin will continue to precess at the Larmor frequency. This precessing dipole moment generates a fluctuating electromagnetic field, which leads to a detectable radio-frequency signal. This signal can be detected with a receive coil and ultimately used to form an image. The strength of the generated radio-frequency signal is proportional to the component of $\mathbf{M}$ in the transverse plane, M_{xy} in the diagram. The exciting radio-frequency field is often termed $\mathbf{B_1}$.

In the absence of any continued radio-frequency signal, the spin will gradually return to its equilibrium state longitudinal to $\mathbf{B_0}$ and the MR signal will decay away. This phenomenon, known as *relaxation*, will be described in more detail below. First, however, the configuration of a typical MRI scanner is described, and an overview given of how the MR signal is used to form an image.

Superconducting polarizing magnet

B_0

Conventional gradient magnets
and RF transmit/receive coil
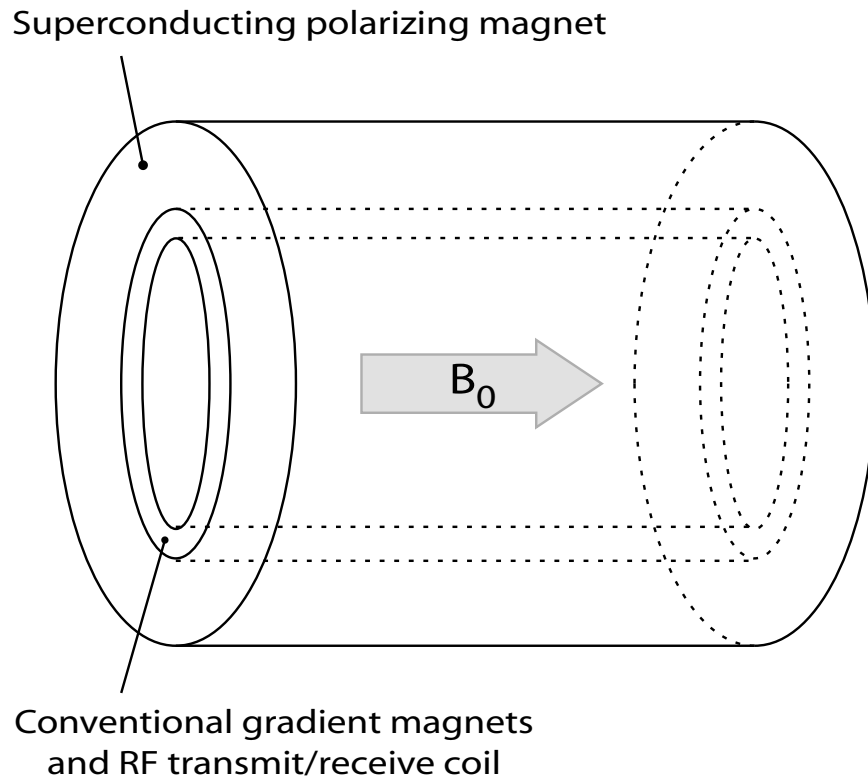
Figure 2.4: The polarizing field $\mathbf{B_0}$ is typically created with a large superconducting solenoidal magnet. Conventional magnets to create field gradients are fitted inside the bore of the superconducting magnet, along with an RF transmit and receive coil. The body to be imaged is placed in the bore of the magnet.

2.2   MRI Hardware Configuration

An actual MR machine typically creates the polarizing field $\mathbf{B_0}$ with a large super-conducting solenoidal magnet (Figure 2.4). The person or body to be imaged is placed in the center bore of the magnet. An RF transmit and receive coil is generally fitted concentric to the main solenoid inside the bore. Several other conventional electromagnets, termed *gradient* magnets, are also fitted just inside the magnet bore. The main superconducting magnet is designed to be extremely uniform (generally to within a few parts per million) across an imaging region in the center. The gradient

magnets produce slight variations to the polarizing field $\mathbf{B_0}$, as will be discussed in more detail below.

2.3 Spatial Encoding

When a body to be imaged is placed in the bore of the scanner and an RF field $\mathbf{B_1}$ applied to tip the spins, the spins begin to precess and emit a signal at the Larmor frequency, as discussed. However, all of the spins are now emitting signal at the same frequency. One would like to be able to distinguish the signal from spins at different locations within the body in order to form an image; in other words, one would like to perform some type of spatial encoding.

Spatial encoding in MRI is accomplished by some combination of three mechanisms: slice-selective excitation, frequency encoding, and phase encoding.

2.3.1 Slice-selective Excitation

Slice-selective excitation is the ability to selectively excite, or tip, spins in a certain slice or slab of the body to be imaged. When the RF field $\mathbf{B_1}$ is applied in the presence of the polarizing field, all of the spins in the imaging volume that are subjected to the RF pulse tip off axis and begin to precess, yielding signal. If, however, the gradient magnets are used to produce a gradient in the magnetic field along a certain direction, spins at different spatial locations will resonate at different frequencies, depending on the local magnetic field they see.

This can be exploited to excite only spins in a certain slice or slab. For example, suppose that the gradient magnets are used to produce a small linear gradient in the magnetic field along the magnet bore, which we will call the z-axis. While this gradient is applied, the RF pulse is played tuned to the Larmor frequency of the main field $\mathbf{B_0}$. Due to the varying magnetic field along the z-axis, only spins in the vicinity of the z location where the local magnetic field is approximately $\mathbf{B_0}$ will
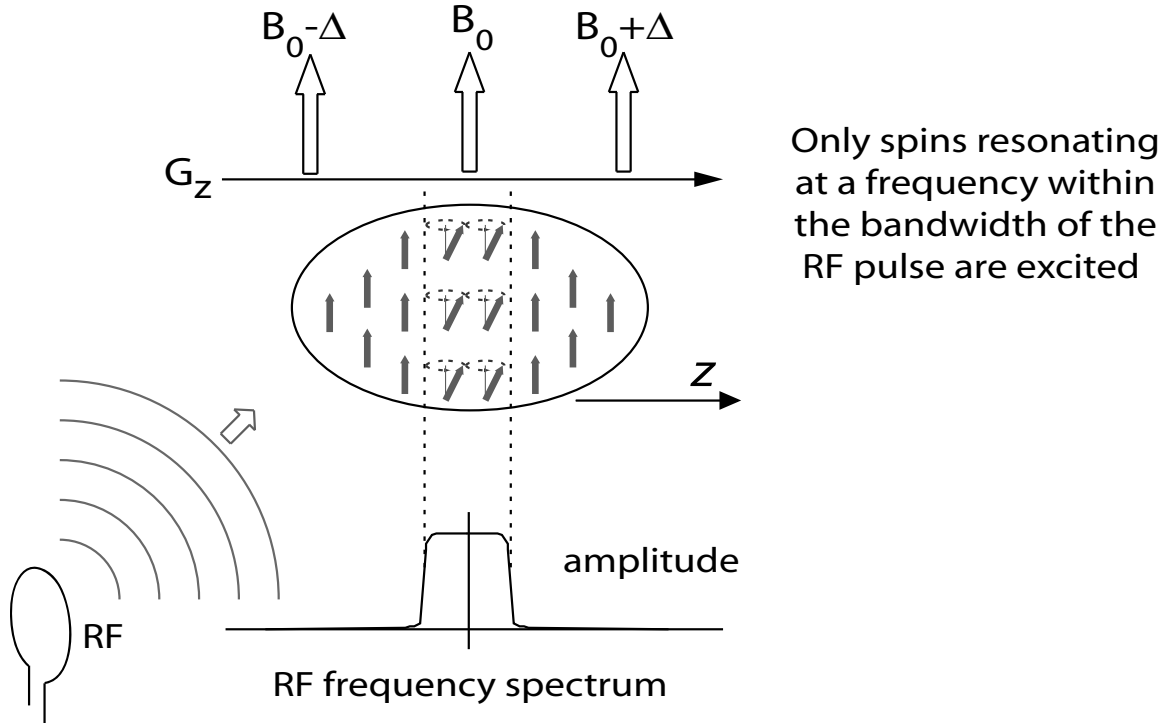
Figure 2.5: It is often useful to excite spins in a slice or slab, rather than exciting the whole volume. An applied magnetic field gradient G_z varies the resonant frequency of spins along the z-axis. If a radio-frequency signal centered at the Larmor frequency with limited bandwidth is played in conjunction with such a gradient field, only spins resonating at a frequency within the bandwidth of the RF pulse will be excited.

be excited and begin to emit signal. Spins at other locations, where the gradient magnetic field alters their resonant frequency, will not resonate and will consequently remain unexcited. This is illustrated in Figure 2.5.

The thickness of the slab may be controlled by either varying the bandwidth of the RF pulse or by varying the magnitude of the slice-selective gradient field. A larger gradient field will produce a thinner excited slab if the RF pulse bandwidth is held constant. Decreasing the bandwidth of the RF pulse will likewise lead to a thinner slab excitation if the gradient field is held constant.

In this way, a three-dimensional spatial localization problem can be reduced to two dimensions (e.g., imaging a thin slice of the volume), or a smaller three-dimensional

volume (a slab) excited within the body. 2D magnetic resonance imaging makes extensive use of slice-selective excitations. Many 3D MRI techniques make use of thicker slab-selective excitation to limit the signal-yielding volume.

2.3.2 Frequency Encoding

Consider a two-dimensional array of excited spins in the polarizing field $\mathbf{B_0}$ (as is the case when a thin slice-selective excitation has been performed). Now suppose a spatially varying gradient field is applied while the MR signal is sampled, as shown in Figure 2.6a. In this example, the excited slice is an xy plane, and the gradient field (denoted G_x) induces a linear variation in magnetic field in the x direction.

Spins at different x locations now see different local magnetic fields, and consequently precess at different frequencies. By analyzing the frequency components of the sampled MR signal, the amount of signal arising from spins at different x locations may be ascertained. In other words, x spin location has been encoded in the signal frequency. This is referred to as *frequency encoding*. One spatial dimension can be encoded in frequency, and subsequently resolved from the detected MR signal.

2.3.3 Phase Encoding

If the gradient field is applied for a fixed period of time *prior* to signal sampling, a different effect is observed. Suppose the gradient field G_y induces a linear variation in magnetic field in the y direction (Figure 2.6b). Spins at different y locations precess at different frequencies during the duration of the gradient field. When the gradient field G_y is turned off, spins at different y locations will have acquired different relative phases. Spin location along y has now been encoded in phase.
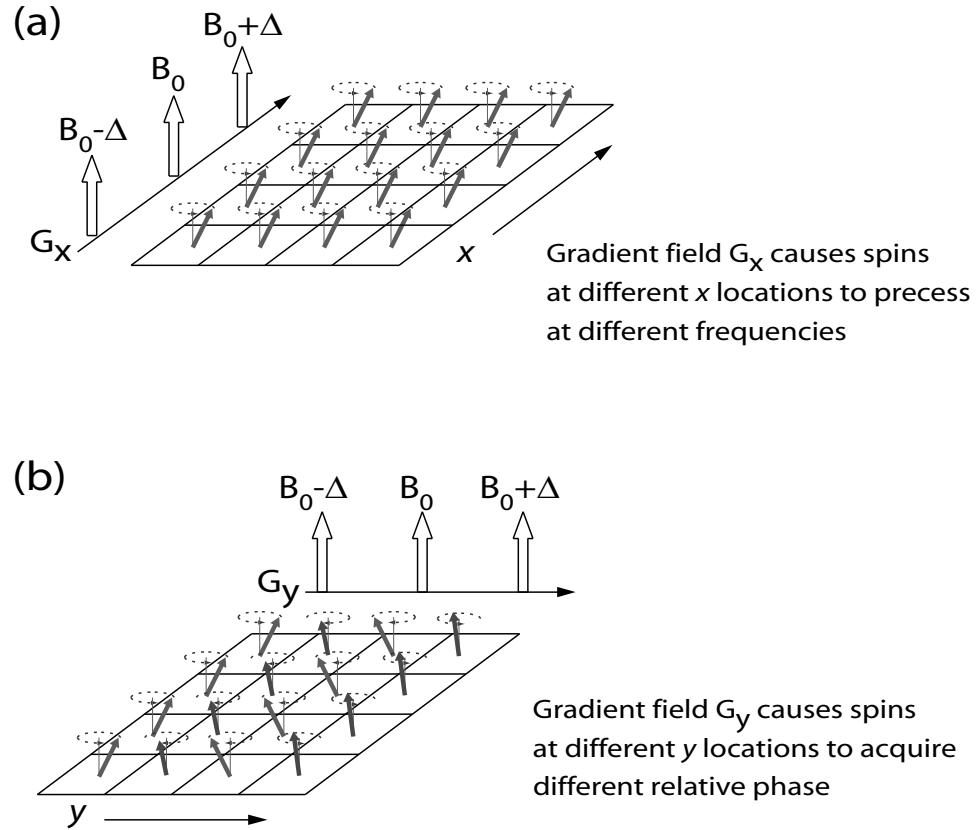
Figure 2.6: (a) A gradient field G_x played during signal sampling (or *readout*) causes spins at different x locations to resonate at different frequencies, encoding x spatial location in the frequency of the sampled signal. (b) A gradient field G_y played for a fixed period of time prior to readout causes spins at different y locations to accrue different relative phase. This encodes y spatial location in the phase of the sampled signal.

2.4   Image Formation

Repeated application of excitation (possibly slice-selective), phase encoding, and signal sampling concurrent with frequency encoding eventually yields all of the data necessary to reconstruct an image. How many such repetitions are required depends on the dimensionality of the image and the matrix size. While the mathematical complexities of image formation will not be discussed here, a set of basic rules governing scan repetitions is given.

In general, one dimension is fully resolved by frequency encoding during signal sampling after each excitation. Formation of a 1D image therefore requires only a single excitation, followed by a sampling period. A frequency-encoding, or *readout*, gradient is applied during the signal sampling period. If N pixels are to be resolved along the single dimension, the signal must be sampled at least N times during the sampling period.

In order to form a 2D image, repeated excitation/phase-encode/readout steps must be performed, each with a different phase encoding gradient played prior to signal readout. If an $M \times N$ image is required, M excitations must be performed, each followed by a readout with at least N sample points. 3D images can be formed by adding even more repetitions. An $L \times M \times N$ image would require $L \times M$ excitation/phase-encode/readout steps.

For a detailed discussion of MR signal sampling criteria, phase-encoding gradient requirements, and a more mathematical description of MR image formation, please see [3].
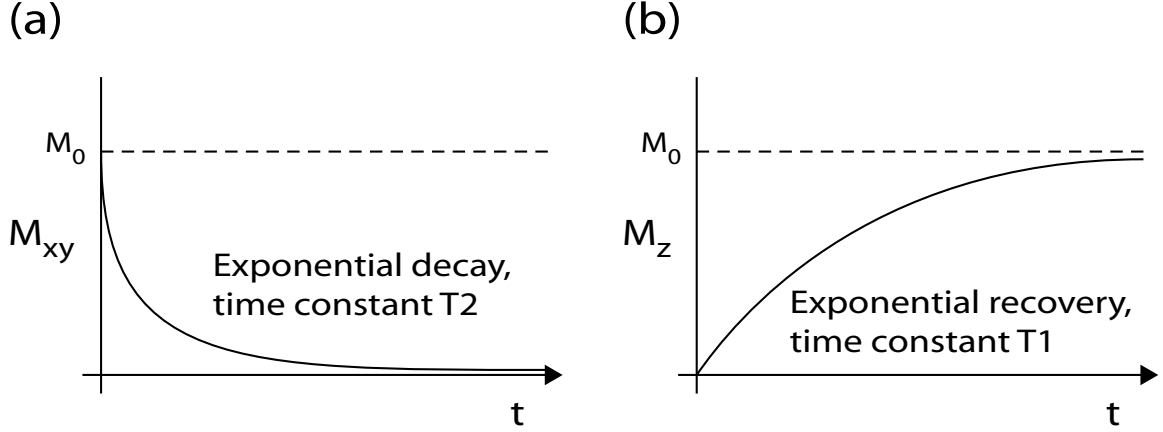
Figure 2.7: (a) The magnitude of the RF signal from a spin is proportional to its transverse component M_{xy}. After excitation, the spin *relaxes* back to its equilibrium position $\mathbf{M_0}$. The transverse component of the spin decays exponentially with time constant T_2. (b) The longitudinal component *recovers* exponentially with time constant T_1.

2.5 Contrast Generation

2.5.1 Relaxation

If all spins gave identical MR signal and the signal did not decay significantly before or during sampling, image formation with phase and frequency encoding would yield contrast based on the density of spins at different locations. However, spins gradually return to their equilibrium (non-precessing) orientation following excitation, leading to a decay in the MR signal. Furthermore, spins in different tissues return to equilibrium at different rates.

The magnitude of the MR signal from a spin corresponds to its transverse component M_{xy}. The transverse component of $\mathbf{M}$ decays exponentially with time constant T_2. For example, after a 90° excitation (where the entire spin is tipped into the transverse plane), M_{xy} is given by

$$M_{xy} = M_0 e^{-t/T_2}.$$

(2.1)

Tissue	T1 (ms)	T2 (ms)
Gray Matter	920	100
White Matter	790	92
MS Lesion	1300	200
CSF / Synovial Fluid	4000	2000
Arterial Blood	1000	200
Venous Blood	1000	100
Muscle	870	47
Fat	270	85

Table 2.1: Selected values at 1.5 T of T_1 and T_2 for relevant tissues. Note that values are approximate. There can be significant variations in T_1 and T_2 based on location in the body, physiological function, pathology, temperature, and a host of other factors.

This signal decay as a function of time is illustrated in Figure 2.7a. T_2 is highly tissue dependent. Some values for various body tissues are shown in Table 2.1.

M_z, the longitudinal component of $\mathbf{M}$, *recovers* exponentially to its equilibrium value of M_0. Following a 90° excitation, M_z is given by

$$M_z = M_0(1 - e^{-t/T_1}).\tag{2.2}$$

This is depicted in Figure 2.7b. T_1, like T_2, is tissue dependent. T_1 is also dependent on field strength. Values for select tissues at a field strength of 1.5 Tesla are shown in Table 2.1.

2.5.2 The Bloch Equation

The dynamics of spin precession and relaxation can be captured in a single phenomenological differential equation known as the Bloch equation. Let γ represent the gyromagnetic ratio, $\mathbf{B}$ the magnetic field vector seen by a spin, T_1 and T_2 the longitudinal and transverse relaxation time constants respectively, and M_0 the equilibirum
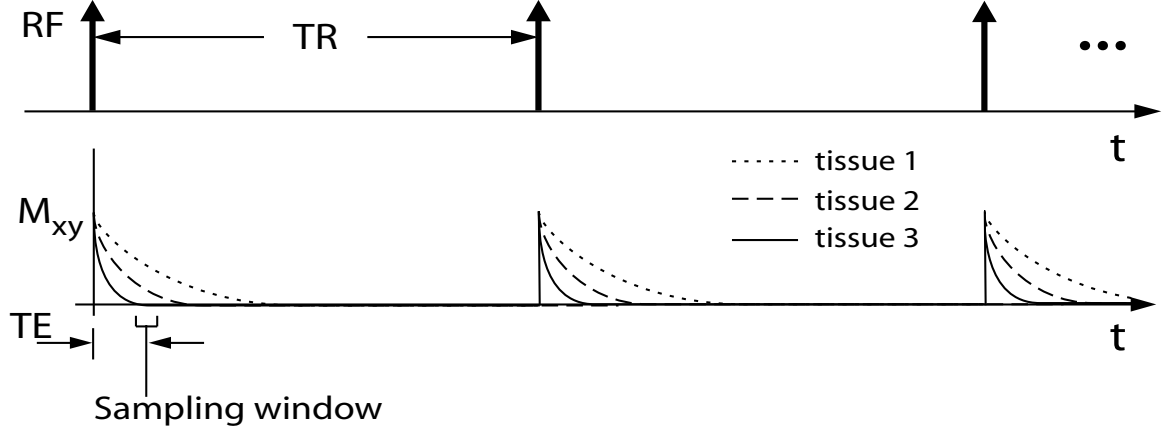
Figure 2.8: A long repetition time TR between excitations allows near-complete spin relaxation. The delay after each excitation prior to signal sampling (or *echo time* TE), can then be adjusted to yield varying degrees of T_2-weighted contrast.

magnetization due to the main polarizing field. Then:

$$\frac{d\mathbf{M}}{dt} = \mathbf{M} \times \gamma\mathbf{B} - \frac{M_x\mathbf{i} + M_y\mathbf{j}}{T_2} - \frac{(M_z - M_0)\mathbf{k}}{T_1}, \tag{2.3}$$

where $\mathbf{i}$, $\mathbf{j}$, and $\mathbf{k}$ are unit vectors in the x, y, and z directions respectively.

Precession of the spin at the Larmor frequency is described by the cross-product term in the Bloch equation, while transverse and longitudinal relaxation are described by the terms containing T_2 and T_1 respectively.

2.5.3 Contrast Generation Examples

Differences in tissue T_1 and T_2 can be exploited to generate MR image contrast. For example, suppose that a long repetition time TR is used between excitations, sufficient for near-complete longitudinal (T_1) recovery between excitations. Suppose further that we sample the signal during a window centered around a delay of time TE after each excitation, as illustrated in Figure 2.8. TE is referred to as the *echo*

time. By varying the length of TE, different kinds of contrast based on tissue T_2 can be generated.

If the signal is sampled after a relatively long TE, only spins with relatively long T_2 will still be producing signal, and will have a much stronger weighting in the image than short T_2 tissues. By varying TE, different degrees of so-called T_2-*weighted contrast* can be generated.

Consider now the case where the repetition time TR is shortened to allow only partial longitudinal recovery between excitations. After a series of excitations, one would expect to detect signal only from tissues with relatively rapid longitudinal recovery, or T_1. Signal from longer-T_1 tissues would be attenuated due to the incomplete longitudinal recovery between excitations. This is known as T_1-*weighted contrast*. In this case, TR is generally chosen to be on the order of T_1 of the tissues one wishes to see, and the echo time TE is typically kept short to avoid T_2 weighting.

2.6 Variations from Perfection

This chapter has thus far ignored any imperfections in the imaging process that could degrade image quality. There are, in reality, numerous factors that pull magnetic resonance imaging systems away from the ideal. These include effects from non-stationary spins (which can, incidentally, also be used to advantage), signal decay during the sampling interval, limitations to transmit and receive coil sensitivities, noise in the electrical systems and body, and a host of confounding factors relating to spins that do not precess at exactly the appropriate frequency (broadly termed *off-resonance*).

Both off-resonance and signal noise are important to later chapters of this dissertation, and are therefore described briefly below.

2.6.1 Off-Resonance

Thus far it has been assumed that the polarizing magnetic field $\mathbf{B_0}$ seen by the body to be imaged is perfectly uniform, and that any variations to it are created by an ideal set of linear gradient magnets. This is generally far from correct. Several factors can create non-uniformities in the polarizing magnetic field, causing spins at different locations to precess at frequencies other than the ideal. These include variations in the main polarizing field, susceptibility-induced field variations, and something known as chemical shift.

Main Field Inhomogeneity

Limitations in magnet technology make it virtually impossible to design and fabricate a polarizing magnet that is perfectly uniform. In order to get the magnetic field as uniform as possible over an imaging volume, small shim coils are added to help cancel any non-uniformity. However, even after extensive shimming, some field inhomogeneity inevitably remains. These field variations, although often quite small, introduce error into the imaging process.

Susceptibility-Induced Field Variations

Perhaps more troublesome in many applications than main-field inhomogeneity are resonant frequency variations arising from differences in bulk magnetic susceptibility across the body. These variations are highly dependent on the geometry and composition of what is being imaged, and are therefore much less predictable than main-field variations. While dynamic shimming can be performed after placement of the body in the magnet, these variations may still be several parts per million or more. Particularly problematic are regions with air/tissue boundaries, or boundaries between other tissues with very different susceptibilities. Irregular geometry compounds the problem— in the feet, for example.

Chemical Shift

The magnetic field experienced by certain nuclei can be slightly smaller than expected due to electronic shielding of the nucleus. The most relevant of these effects for this dissertation is the electronic shielding experienced by hydrogen nuclei in lipids (or fats). While the amount of shielding varies with different types of lipid, a chemical shift in resonant frequency of approximately 3.5 parts per million is often assumed. At a field strength of 1.5 Tesla, this corresponds to a reduction in resonant frequency by approximately 230 Hz. In other words, lipid spins precess about 230 Hz slower than water spins exposed to the same external field.

2.6.2   Image Noise

The main source of noise in conventional MR imaging arises from random electrical fluctuations in the imaging body due to the Brownian motion of electrons in conductive tissues. While electrical noise from the receive coil is also present, body noise generally dominates in conventional MR imaging. Exceptions to this occur when coils with a very small volume of sensitivity are used, leading to reduced body noise (and consequently electrical noise dominance), or when imaging is performed at low fields.

Quadrature detection of the MR signal yields both magnitude and phase information. The noise can be modelled as a complex (bi-variate) zero-mean Gaussian process. The real and imaginary components are independent, and each possess the same variance.

2.7   Summary

This concludes the review of the fundamental concepts that make magnetic resonance imaging possible. While not exhaustive, the overview presented should provide an adequate framework for the material that follows. As the research presented in this dissertation primarily deals with a class of MRI sequences known as fully-refocused,

or balanced, steady-state free precession (SSFP), the following chapter describes balanced SSFP in detail.

Chapter 3

Steady-State Free Precession (SSFP)

This dissertation concerns itself primarily with a class of MRI techniques known as fully-refocused, or balanced, steady-state free precession (SSFP). As previously mentioned, advances in the performance of MRI gradient hardware have made these sequences practical, and they are currently a topic of considerable research. Balanced SSFP shows strong potential for a broad range of applications, and can often achieve significant gains in both signal-to-noise ratio (SNR) and total scan time over other methods. This chapter is devoted to developing the essential concepts of SSFP, and presenting some of the existing SSFP techniques upon which subsequent chapters build. Note that for brevity, the "fully-refocused" or "balanced" is sometimes omitted.

3.1   Overview

Figure 3.1 shows what is termed a *pulse sequence diagram* for a typical 2D balanced SSFP sequence. The diagram shows the timing of the RF and gradient pulses used.

A series of RF pulses (of tip angle α and phase ϕ) are played at constant interval TR. Typical values of TR for SSFP are between 2 ms and 12 ms, depending on the
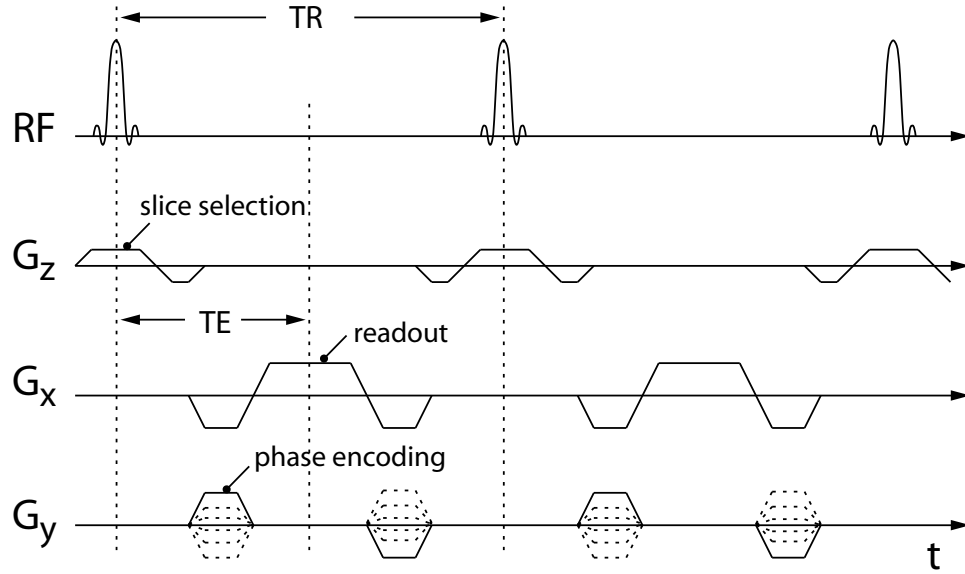
Figure 3.1: The balanced SSFP sequence employs a series of RF pulses played at constant interval TR, with TR typically between 3 and 12 ms. All gradient fields, including the slice-selective gradient, are fully refocused to eliminate coherences from excitation to excitation.

application. Recall that values for T_2 are greater than 40 ms for many common tissues, and values of T_1 are typically several hundred milliseconds or more. Consequently, there is very little time for spin relaxation between excitations, although spin free precession (hence the name) occurs during the TR interval. The signal is sampled on an interval centered about a delay of time TE after each excitation. For some applications, the phase profile of the signal is advantageous if the sampling window is centered between excitations, with TE = TR/2.

If one examines the signal magnitude from excitation to excitation, initial transient oscillations are observed, as spins do not have time to return to a near-equilibrium state prior to subsequent excitations. After a period of time (several times the longest T_1 present), the signal reaches a steady state, and stabilizes from excitation to excitation. It is during this steady state that imaging is performed in normal SSFP. The transient characteristics of SSFP sequences will be treated in a later section.

Notable in fully-refocused SSFP sequences is the "refocusing", or "balancing", of all gradient fields. This means that the area of each gradient field integrates to zero across any given TR, or, equivalently, that the zeroth moments of the gradient fields are nulled. As a consequence, the gradients have no net effect on spin precession from one excitation to the next: any phase accumulation across a TR due to gradient fields is "rewound" prior to the subsequent excitation[1].

The short TR of SSFP sequences allows extremely fast scan times, and the signal yield is often more than 30% higher than other steady-state MRI techniques, such as GRASS (hence their popularity). There are, however, some complicating issues, discussed below.

3.2   SSFP Spectra

If one simulates the excitation, relaxation, and precession during SSFP of spins at different off-resonance frequencies, a strong dependence of signal on off-resonance frequency emerges. That is, spins that precess different amounts from TR to TR will yield very different steady-state signals. Before moving on to a discussion of SSFP off-resonance characteristics, the mathematics for computing SSFP *off-resonance spectra* or *spectral profiles* are presented.

3.2.1   Simulating SSFP Spectra

Off-resonance spectra are typically computed as a function of one of two variables: (1) off-resonance frequency (relative to the center frequency defined by B_0), or relatedly (2) the free-precession angle β. The free-precession angle β is the angle through which a spin will precess over one TR relative to a spin at the center frequency. In this section, the latter convention is adopted, as it is free from dependence on TR.

---

[1] Note that this is only true for stationary spins. Spins undergoing motion can experience some net phase effects from excitation to excitation. Gradient fields are sometimes designed with higher order moment nulling to reduce coherences for moving spins.

Off-resonance spectra are a function of both the tissue parameters (T1, T2, and proton density ρ), and the sequence parameters TR, TE, and α. Denote the equilibrium magnetization vector of a tissue (the magnetization vector in the presence of only the polarizing field B_0) as M_0, and let M_1^- and M_1^+ denote the magnetizations immediately prior to and immediately after an RF excitation (or tip) respectively. Then

$$M_1^+ = RM_1^-, \tag{3.1}$$

where R is given by

$$R = \begin{bmatrix} \cos(\alpha)\sin^2(\phi) + \cos^2(\phi) & (1 - \cos(\alpha))\cos(\phi)\sin(\phi) & -\sin(\alpha)\sin(\phi) \\ (1 - \cos(\alpha))\cos(\phi)\sin(\phi) & \cos(\alpha)\cos^2(\phi) + \sin^2(\phi) & \sin(\alpha)\cos(\phi) \\ \sin(\alpha)\sin(\phi) & -\sin(\alpha)\cos(\phi) & \cos(\alpha) \end{bmatrix}, \tag{3.2}$$

and denotes a simple rotation by angle α about an axis in the XY plane that makes angle ϕ with the X-axis.

Immediately prior to the subsequent tip, the spin undergoes both T_1 and T_2 relaxation and off-resonance precession, such that:

$$M_2^- = PEM_1^+ + (I - E)M_0 = PERM_1^- + (I - E)M_0, \tag{3.3}$$

where the T_1 and T_2 relaxation matrix is described by

$$E = \begin{bmatrix} e^{-TR/T2} & 0 & 0 \\ 0 & e^{-TR/T2} & 0 \\ 0 & 0 & e^{-TR/T1} \end{bmatrix} \tag{3.4}$$

and the off-resonance precession is described by:

$$P = \begin{bmatrix} \cos(\beta) & \sin(\beta) & 0 \\ -\sin(\beta) & \cos(\beta) & 0 \\ 0 & 0 & 1 \end{bmatrix}. \tag{3.5}$$

In the steady state, $M_2^- = M_1^- \equiv M^-$, and

$$M^- = PERM^- + (I - E)M_0 \tag{3.6}$$

$$M^- = (I - PER)^{-1}(I - E)M_0. \tag{3.7}$$

M^+, the steady-state magnetization vector immediately after an RF excitation, is then given by

$$M^+ = RM^-. \tag{3.8}$$

The steady-state magnetization at the echo time TE is related to M^+ by

$$M_{TE} = P_{TE}E_{TE}M^+ + (I - E_{TE})M_0, \tag{3.9}$$

where E_{TE} and P_{TE} represent the relaxation and precession, respectively, that occur during a time TE, and are given by

$$E_{TE} = \begin{bmatrix} e^{-TE/T2} & 0 & 0 \\ 0 & e^{-TE/T2} & 0 \\ 0 & 0 & e^{-TE/T1} \end{bmatrix} \tag{3.10}$$

and

$$P_{TE} = \begin{bmatrix} \cos(\beta \cdot \frac{TE}{TR}) & \sin(\beta \cdot \frac{TE}{TR}) & 0 \\ -\sin(\beta \cdot \frac{TE}{TR}) & \cos(\beta \cdot \frac{TE}{TR}) & 0 \\ 0 & 0 & 1 \end{bmatrix}. \tag{3.11}$$

3.2.2 Phase-Cycling

A typical SSFP off-resonance spectrum is shown in Figure 3.2(a). The spectra are periodic in β (or off-resonance frequency), and typically have a passband section and a section of low signal each period. The low-signal section is the source of *off-resonance banding artifact*, which is treated in detail in Chapter 4. The signal phases shown in Figure 3.2 assume TE = TR/2. Note that at this symmetric echo time TE, the phase
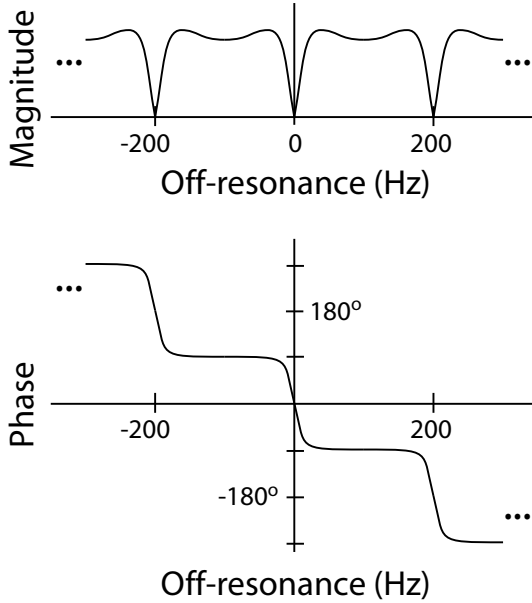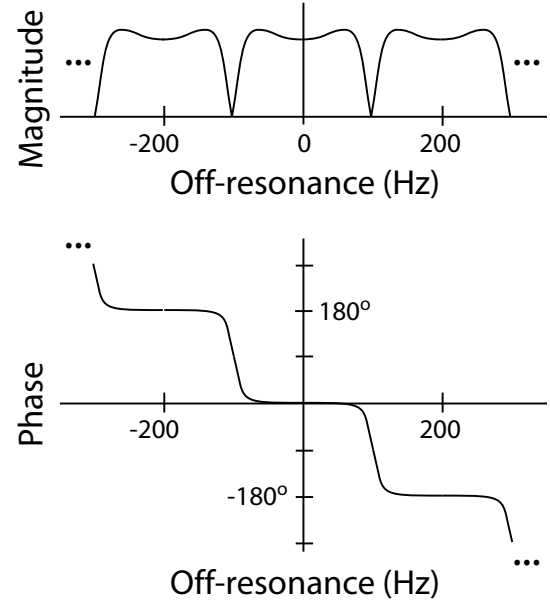
Figure 3.2: (a) The SSFP signal is a strong periodic function of local resonant frequency. Relatively broad sections of high signal are separated by sections of near-complete signal loss. (b) If the RF phase is incremented by a constant value $\Delta\phi$ from excitation to excitation, a shift is observed in the SSFP signal magnitude. Both (a) and (b) assume an echo time TE = TR/2, which leads to flat phase profiles across the passbands, as shown.

is relatively flat across the signal passband and transitions rapidly across the section of low signal. Subsequent passbands are 180° out of phase.

One useful variation on the normal SSFP sequence is *phase-cycled SSFP*. The spectrum shown in Figure 3.2(a) assumes constant RF phase ϕ from excitation to excitation. If the RF phase is instead incremented each excitation by a value $\Delta\phi$, a corresponding shift by $\Delta\phi$ occurs in the spectral magnitude (Figure 3.2(b)). The phase profile is likewise shifted, with an accompanying addition of constant phase.

Several of these shifted profiles can be acquired (each employing a different $\Delta\phi$), and reconstructed to eliminate artifact and improve SNR (Chapter 4).

SSFP Off-Resonance Profile Dependence
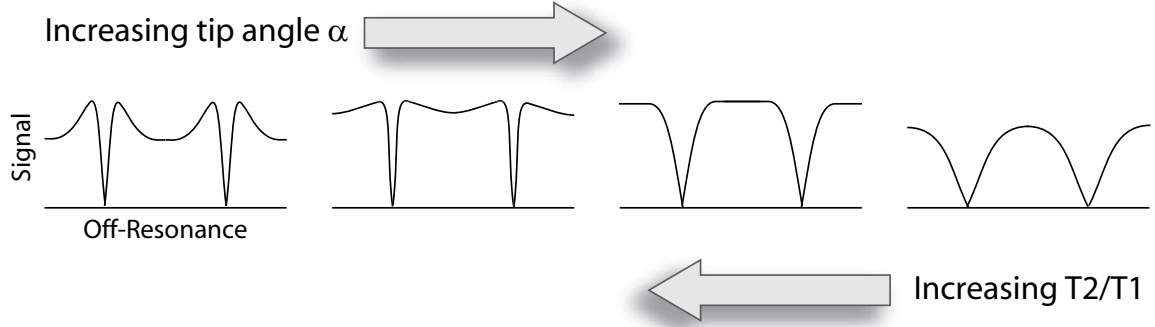
Figure 3.3: The shape of SSFP off-resonance profiles varies with tissue and scan parameters. As tip angle α is increased, profiles tend to lose their bimodal shape (shown at left) and evolve into a single rounded hump (shown at right). A corresponding effect is seen with decreasing T_2/T_1.

3.2.3 Spectral Dependence on Tissue and Scan Parameters

SSFP off-resonance profiles vary with tissue and scan parameters. As the tip angle α is increased, the profile becomes more rounded and loses the bimodal shape of lower tip angles (Figure 3.3). The dependence on tissue parameters is related to T_2/T_1. The effect of increasing T_2/T_1 is opposite to that of increasing α. As T_2/T_1 increases, the profile becomes more bimodal in shape, and the center of the passband dips down.

As TR increases, more relaxation occurs between excitations. This leads to less signal loss between passbands. However, the speed advantage of SSFP is lost at longer TRs, and the sequence resembles other gradient-recalled methods. Use of TE other than TE = TR/2 leads to a linearly sloping phase profile across the passband, rather than the flat phase profile resulting from TE = TR/2.
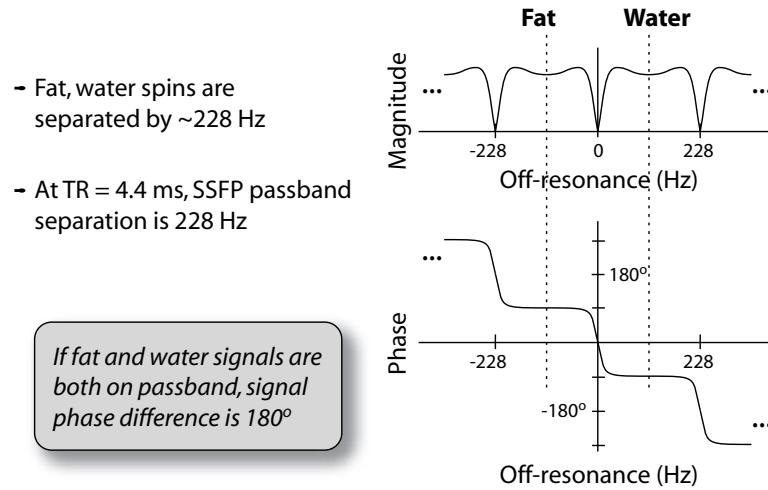
Figure 3.4: If a TR of 4.4 ms is used in SSFP, the center of subsequent passbands is separated by 228 Hz, which corresponds to the separation of water and fat spins at 1.5 T. A balanced echo time TE = TR/2 leads to flat phase profiles across the passbands, with adjacent passband phase separated by 180°. By placing fat and water spins in adjacent passbands, the phase difference between voxels containing fat and those containing water can be used to detect fat voxels and suppress them.

3.2.4   Some Applications of Spectral Profiles

The spectral characteristics of SSFP signal phase have been used in several novel ways. At a TR of 4.4 ms, the center of subsequent signal passbands is separated by 228 Hz. At 1.5 Tesla, lipid and water spins are separated in frequency by approximately 228 Hz. If lipid spins are made to fall in the center of an SSFP signal passband, water spins will fall in the center of the adjacent passband (Figure 3.4). Adjacent passbands are 180° out phase, leading to a 180° phase difference between fat and water pixels in our reconstructed image.

This phase-difference can be used to identify fat and water pixels [4, 5]. Pixels identified as lipid can then be zeroed out for fat suppression. The technique is sensitive to partial-volume effects (e.g., a pixel contains some fat and some water), but is
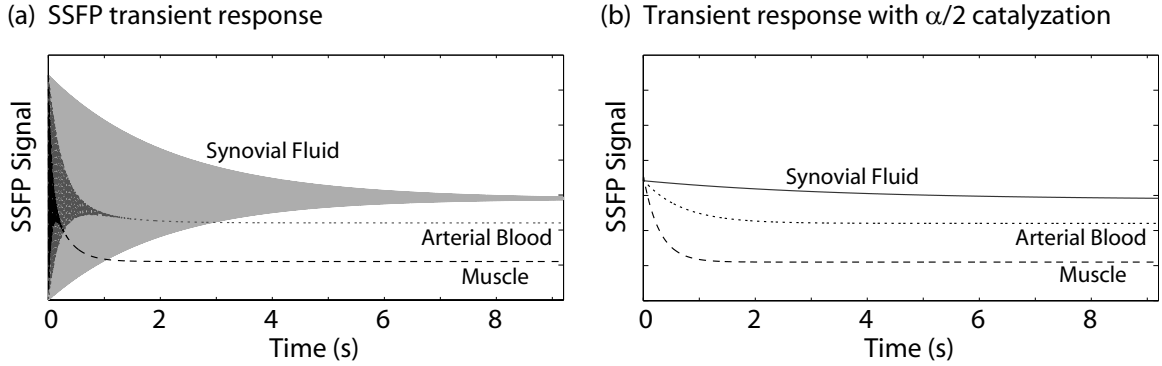
Figure 3.5: (a) The SSFP signal exhibits oscillatory and exponential transient behavior prior to establishing a steady state. Long-T_1 tissues, such as synovial fluid, may take more than 5 seconds to reach steady state. The oscillating signal is generally unusable for imaging. (b) Application of a *catalyzing* sequence prior to SSFP excitations reduces the transient oscillations and allows image acquisition to begin shortly after SSFP excitations begin.

sufficiently robust for many applications. The flow-independent angiography method presented in Chapter 6 makes use of this phase-sensitive fat detection.

Another interesting application makes use of the rapidly varying phase across the low-signal section of the profile. In this region, small changes in resonant frequency lead to large changes in signal phase. Increased blood-oxygenation in active regions of the brain leads to a slight variation in resonance frequency with respect to unactivated regions. The phase change in SSFP signal due to this shift in frequency has been successfully used to create "functional" contrast useful for studying brain activation [6].

3.3   Transient Response and Catalyzation

Figure 3.5(a) shows SSFP signal evolution as a function of time for several different tissues. The graphs were generated from the simulated SSFP center-passband signal at echo time TE = TR/2 from excitation to excitation. Notice that the signal exhibits severe transient oscillations prior to establishment of a steady state. The duration

of the transient oscillations is longer for longer T_1 tissues. The transient exhibits a smooth exponential approach to the steady-state signal in addition to the oscillatory component. If image data is acquired during the oscillating transient period, severe image artifacts can result.

The wait required before signal oscillations die down is undesirable for a number of reasons. First, overall scan time is increased due to the delay. Second, so-called *magnetization preparation* techniques, wherein prepulses are applied to manipulate the magnetization initial conditions for contrast generation, are made ineffective. By the time a steady state is established, the effects of any magnetization preparation have typically worn off.

Several techniques have been proposed that reduce the transient oscillations, resulting in signal evolution like that shown in Figure 3.5(b). These include application of a simple $\alpha/2$ pulse a time TR/2 prior to SSFP excitations [7], a linear ramp of pulses from 0 to α [8], and more complicated techniques effective across broader sections of the spectrum [9]. These techniques, called *steady-state catalyzation*, render the transient signal usable, and enable magnetization-prepared SSFP. Steady-state catalyzation is essential to the sequences presented in Chapters 5 and 6.

3.4 Contrast

The contrast of normal SSFP is defined by the signal levels for different tissues in the steady state, as shown in Figure 3.6. These steady-state signal levels are a (somewhat complicated) function of T_2/T_1. SSFP sequences are therefore commonly said to yield T_2/T_1 *contrast*. The off-resonance value used for computation of SSFP contrast is generally taken to be in the center of a spectral passband.

If steady-state catalyzation is used, the transient oscillations are essentially eliminated, as discussed. However, the smooth exponential approach to the steady-state is still present. If low spatial frequencies (i.e., the center of k-space) are acquired during
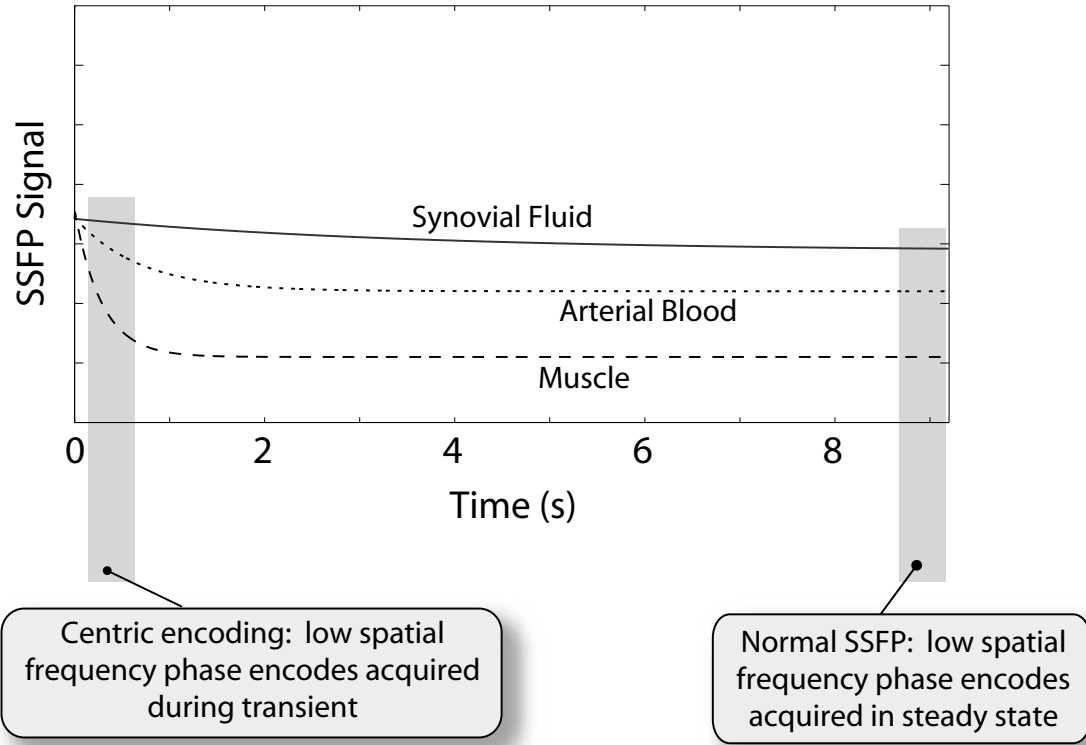
Figure 3.6: If low spatial frequency data is acquired during the transient period immediately after steady-state catalyzation, image contrast very different from that in the steady state may result. Magnetization-preparation sequences can be played prior to catalyzation, further modifying image contrast.

the transient period, different contrast results (Figure 3.6). Phase encode orderings that acquire low spatial frequency k-space first are termed *centric*.

If a centric ordering is used and no magnetization preparation is employed, contrast will be more proton-density weighted than T_2/T_1 weighted [10]. Magnetization preparation coupled with centric ordering and steady-state catalyzation allows flexibility in the generation of contrast.
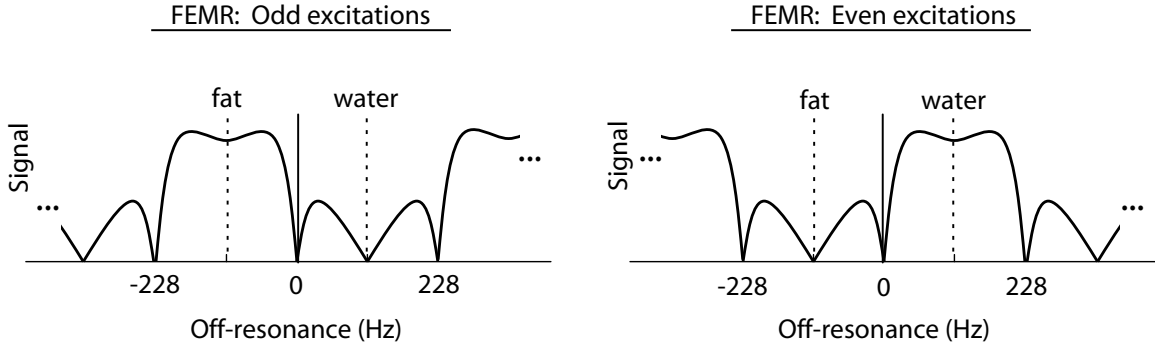
Figure 3.7: Periodic variations in tip angle and/or phase from excitation to excitation lead to oscillating equilibriums in SSFP. One such dual-equilibrium sequence is FEMR, used to simultaneously acquire fat and water images. In FEMR, the RF phase is alternated between 0° and 90° on subsequent excitations. A different equilibrium signal is then observed after odd- and even-numbered excitations. A fat image can then be acquired on odd-numbered excitations, and a water image acquired on even-numbered excitations.

3.5   Oscillating Steady-State SSFP

Thus far the discussion of SSFP sequences has been limited to the case where tip angle and TR are identical from excitation to excitation, and variations in tip phase are limited to a constant increment $\Delta\phi$. If instead periodic variations are introduced in tip angle, phase, and TR, an *oscillating equilibrium* results. Instead of a single steady-state signal being observed from excitation to excitation, periodic variations in the steady-state signal from excitation to excitation will result. If the variations in tip angle, phase, and TR are periodic every N excitations, the steady-state signal will share this periodicity.

An oscillating equilibrium sequence (with periodicity $N = 2$) has been effectively used for fat suppression [11]. The sequence alternates the RF phase between 0 and 90°, resulting in the dual equilibrium shown in Figure 3.7. Each of the spectra exhibits a passband and a stopband. Appropriate choice of repetition time TR allows water to be placed in a passband while fat is in a stopband. If signal is sampled during both equilibria, both a fat and water image can be reconstructed. FEMR has been

shown effective for suppressing fat in articular cartilage imaging [12–14]. Another
interesting dual-equilibrium sequence has been proposed for angiography [15].

The design of oscillating equilibrium SSFP sequences with desired spectral charac-
teristics is the subject of [16]. In this paper, an approach making use of the Shinnar-Le
Roux (SLR) transform is presented for synthesizing oscillating equilibrium sequences
based on periodic variations in tip angle and phase. An extension of this work is
presented in Appendix A. A complex-optimization method for sequence synthesis is
presented, allowing periodic variations in tip angle, phase, and TR.

Chapter 4

Multiple-Acquisition SSFP

4.1   Introduction

Refocused steady-state free precession (SSFP, TrueFISP, or FIESTA) imaging yields high signal in short scan times, but is limited by high sensitivity to local field variation, as discussed in the previous chapter [11, 17–26]. Characteristic banding artifacts may appear where local field variations are large, due to the strong dependence of signal strength on local resonant frequency. At certain off-resonant frequencies, signal nulls are observed, leading to bands of signal loss in the reconstructed image.

Field inhomogeneity can scale with main magnetic field strength B_0, leading to more pronounced banding artifact at higher field strengths. Likewise, as the sequence repetition time TR is increased, any off-resonance banding artifact will become more pronounced due to the increased off-resonance precession per TR. To eliminate off-resonance banding from an image, the resonant frequency across the field of view must be confined to a range of frequencies with width no larger than about 2/(3TR) [27]. Even with a very good shim, this requirement can be difficult to meet at higher field strengths, or in situations where a longer TR is required for higher resolution or due to SAR constraints.

A method for reducing or eliminating off-resonance banding in SSFP at higher field strengths and longer TRs would clearly be useful. Many applications could benefit from the contrast and fast scan times of SSFP, coupled with the enhanced signal of higher B_0 and increased flexibility in choice of TR to increase resolution or reduce SAR. Several such methods have been proposed which reduce the banding artifact by combining multiple SSFP acquisitions, each with a different RF phase increment from excitation to excitation [19, 22, 23, 25, 28]. These methods include maximum-intensity [22], complex-sum [25], and magnitude-sum [28] combination.

Gauging the performance of each of these methods poses some interesting problems, which can be divided into three groups:

(1) Banding artifact reduction: With each combination method, some residual banding artifact remains. How can the effectiveness of each method at removing off-resonance banding be measured? How does this effectiveness vary with scan parameters, such as flip angle and the relevant tissue parameters? Which technique most effectively removes banding for a given application?

(2) Signal-to-Noise Ratio: After using a multiple-acquisition technique to form an image, the SNR is a function of local resonance frequency. How can the SNR of a multiple-acquisition SSFP image be consistently defined and predicted? How do each of the techniques compare in terms of SNR efficiency?

(3) Contrast: What effect (if any) do the various combination techniques have on image contrast? Do they preserve fundamental SSFP contrast, and if not, how is the contrast modified?

This chapter describes the maximum-intensity and complex-sum SSFP combination techniques mentioned above, and introduces a sum-of-squares combination method. A general framework for analysing banding artifact reduction, SNR, and contrast of any multiple-acquisition technique is presented, and applied to the techniques considered. Results are then verified experimentally, comparing the actual contrast, banding, and SNR to that predicted by theory. Finally, theoretical comparisons of each technique across a range of sequence and tissue parameters are presented.
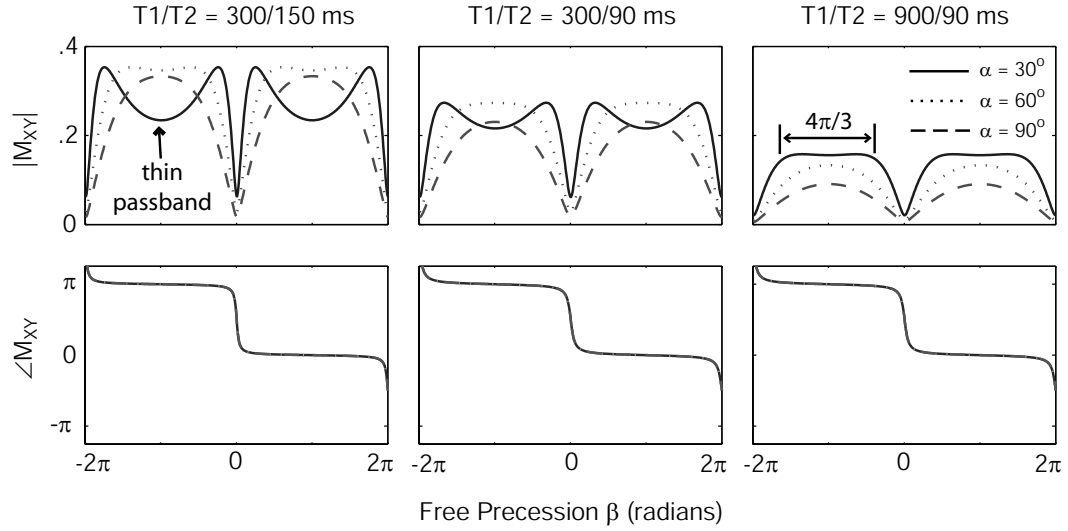
Figure 4.1: SSFP off-resonance signal profiles for several tissues. The magnitude and shape of SSFP spectral profiles is a strong function of T_1/T_2 and flip angle α. The shape of a profile varies little with TR, provided TR is small compared with T_2. All graphs shown employed TR/TE = 10/5 ms. For each tissue, profiles are computed for $\alpha = 30°, 60°$, and $90°$. Notice the variations in signal homogeneity and passband width with T_1/T_2 and flip angle.

4.2 Theory

4.2.1 Summary of Multiple-Acquisition Techniques

Figure 4.1 shows a series of SSFP off-resonance spectra for several tissue parameters and flip angles. As seen in the figure, the signal level is a strong function of free precession per TR (denoted by β), and a sharp signal null periodic in β is observed. This signal null is the source of off-resonance banding artifact. Furthermore, the shape of the off-resonance spectrum varies significantly with T_1, T_2, and flip angle α. One typically tries to limit α across the field of view to a flat region in the off-resonance spectrum, thus avoiding any signal nulls. This flat region has a width in general not greater than approximately $4\pi/3$ radians (Figure 4.1(c)), and for certain tissue and sequence parameters can be even thinner (Figure 4.1(a)).
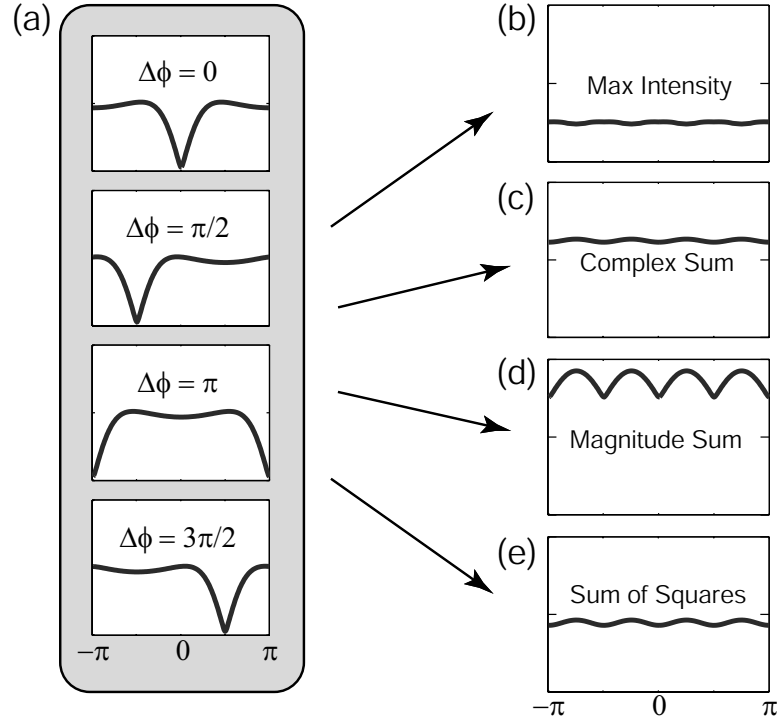
Figure 4.2: The magnitudes of the spectral profiles for single-acquisition phase-cycled SSFP are shown in (a) for $\Delta\phi = 0$, $\frac{\pi}{2}$, π, and $\frac{3\pi}{2}$. Notice the shifting of the profile by $\Delta\phi$ in each case. When phase-cycled images are combined, the more homogeneous spectral profiles shown in (b-e) are obtained.

The spectra shown in Figure 4.1 employ identical RF phase ϕ from excitation to excitation. If the phase is instead incremented by a constant value $\Delta\phi$ from excitation to excitation, the off-resonance profile is shifted by $\Delta\phi$ along the β axis, as shown in Figure 4.2(a) [19]. This shift in the off-resonance spectra with RF phase increment is what makes multiple-acquisition SSFP possible.

All of the multiple-acquisition combination methods analyzed in this chapter employ identical data-acquisition techniques, and differ only in reconstruction. A series of N SSFP acquisitions are obtained ($N \geq 2$), each acquisition employing a fixed RF phase increment $\Delta\phi = 2\pi n/N$ radians from excitation to excitation, where n ranges from 1 to N. Thus a set of N individual SSFP data sets is acquired, each with a shifted spectral profile as illustrated in Figure 4.2(a) for $N = 4$. Each of the methods

considered is differentiated by the manner in which the individual acquisitions are combined to form the reconstructed image.

Maximum-Intensity SSFP (MI-SSFP): Each of the N acquisitions is independently reconstructed. The final image is formed by assigning each pixel the maximum value of the corresponding pixels across the N acquired images. The flatness of the resultant off-resonance profile, and hence the method's effectiveness at removing banding, is clearly a function of both N and the shape of the component off-resonance spectra. For some tissue and sequence parameters, this technique performs quite well, even for $N = 2$. The resultant profile for $N = 4$, $T_1 = 600$ ms, $T_2 = 100$ ms, $\alpha = 30°$, and TR/TE = 3.6/1.8 ms is shown in Figure 4.2(b).

Complex-Sum SSFP (CS-SSFP): In this technique, the complex k-space data from each of the N acquisitions is summed, reconstructed, and the magnitude taken to yield the final image (or, equivalently, each acquisition is reconstructed and the resulting complex images summed, followed by a magnitude operation). Again, the flatness of the resultant off-resonance profile depends strongly on N and the shape of the off-resonance spectrum of an individual acquisition, which depends in turn on T_1, T_2, α, and (to a much smaller degree) TR. A sample profile is shown in Figure 4.2(c). As N gets large, the spectral profile of complex-sum SSFP converges to that of GRASS.

Magnitude-Sum SSFP (MS-SSFP): If each of the individual acquisitions is reconstructed, and the final image formed by summing the magnitude of each individual image, better SNR is expected because there is no signal loss from phase differences across the constituent images. However, calculations of the resulting off-resonance profile show that this method is significantly less effective at reducing banding artifact (Figure 4.2(d)). The sum-of-squares technique presented below yields similar SNR to MS-SSFP, but is much more effective at eliminating banding artifact. For this reason, MS-SSFP is omitted from further consideration in this dissertation.

Sum-of-Squares SSFP (SOS-SSFP): A sum-of-squares reconstruction is performed by individually reconstructing each of the N acquisitions. Each image is then squared, the results summed, and the final image formed by taking the square root. A similar method is often employed when combining component images from phased-array coils

[29]. A statistical justification for this technique is presented in *Results*. The resultant profile is shown in Figure 4.2(e).

4.2.2   Statistical Analysis of Multiple-Acquisition SSFP

In this section, a framework for the statistical analysis of multiple-acquisition SSFP that can be applied to all of the techniques considered is presented.

The signal in an SSFP acquisition is proportional to the steady-state transverse magnetization M_{XY} at the echo time TE, which has both a magnitude and phase that vary with β [17, 18, 30]. This is indicated in Figure 4.1.

Consider a reconstructed pixel from a single SSFP acquisition (prior to taking the image magnitude for display). The pixel contains both magnitude and phase information, and is therefore complex valued. To a good approximation, this signal can be modelled as a bivariate Gaussian random variable X with complex mean μ_X and standard deviation σ_X. That is:

$$X = \mu_X + N(0, \sigma_X^2) + iN(0, \sigma_X^2) \tag{4.1}$$

where $N(\mu, \sigma^2)$ represents the Gaussian (or normal) distribution with mean μ and variance σ^2.

If N phase-cycled SSFP acquisitions are performed, a set of N sample points is acquired for each voxel to be reconstructed. Let the bivariate Gaussian random variables $X_1, \ldots, X_N$ represent these samples, and denote their respective means by $\mu_1, \ldots, \mu_N$. Each X_n is expected to have the same standard deviation, denoted here by σ_0, since the noise is a property of the system and scan parameters and will not vary with n. Now suppose that the voxel on which the analysis is performed undergoes an off-resonance free precession of β_0 radians over one TR. The complex mean of the nth sample is then given by:

$$\mu_n = M_{XY,n}(\beta_0), \tag{4.2}$$

where $M_{XY,n}(\beta)$ is the off-resonance profile of a single SSFP acquisition with phase-cycle increment $\Delta\phi = 2\pi n/N$.

When the observations X_n are combined to yield a final reconstructed voxel, the statistical distribution of the reconstructed voxel may be described by a new random variable Y, which is some function of the X_n. That is,

$$Y(\beta_0) = f(X_1, \ldots, X_N). \tag{4.3}$$

The above analysis permits the determination of the statistical distribution of Y for any value of the free-precession angle β. One can then find both $\mu_Y(\beta)$ and $\sigma_Y(\beta)$. Note that $\mu_Y(\beta)$ represents the expected signal at any value of β, and is simply the resulting off-resonance spectrum (or magnetization profile) of the multiple-acquisition technique.

To apply the above framework to predict $\mu_Y(\beta)$ and $\sigma_Y(\beta)$, one needs to know σ_0 in addition to the tissue and scan parameters. Let SNR_{SSFP} denote the SNR expected from a single SSFP acquisition perfectly shimmed to the center of the passband. SNR_{SSFP} is related to σ_0 as:

$$SNR_{SSFP} \equiv \frac{M_{XY,\frac{N}{2}}(\beta = 0)}{\sigma_0}, \tag{4.4}$$

where $M_{XY,\frac{N}{2}}$ is the off-resonance spectrum with phase-cycling $\Delta\phi = \pi$. Note that a phase-cycling value of $\Delta\phi = \pi$ centers the passband around $\beta = 0$, as shown in Figure 4.2. If needed, SNR_{SSFP} can be empirically determined from a single SSFP acquisition in a region close to the center of the passband (as determined by the band structure of the image). As a practical matter, the application of the above analysis to gauge the performance of each multiple-acquisition technique across a range of possible values of SNR_{SSFP} is of more interest. The tradeoffs in scan time, residual banding, contrast, and SNR between the ideal case of a single center-passband SSFP acquisition and each multiple-acquisition technique can then be analyzed. It is therefore more convenient to use SNR_{SSFP} as an input into the analysis than σ_0.

Using this framework, the statistics of a reconstructed voxel in each of the multiple-acquisition techniques are represented as follows:

$$\text{Maximum-intensity SSFP:} \qquad Y_{MI} = \max(|X_1|, \ldots, |X_N|) \qquad (4.5)$$

$$\text{Complex-sum SSFP:} \qquad Y_{CS} = |X_1 + \cdots + X_N| \qquad (4.6)$$

$$\text{Sum-of-squares SSFP:} \qquad Y_{SOS} = \sqrt{|X_1|^2 + \cdots + |X_N|^2} \qquad (4.7)$$

Solving for these distributions determines $\mu_Y(\beta)$ and $\sigma_Y(\beta)$ for each technique, which in turn can be applied to analyze residual banding, SNR, and contrast, as outlined below.

4.2.3 Residual Banding and Contrast

The residual banding of an SSFP combination scheme can be quantified by examining the signal variations across a period of the spectrum. Let S_{max}, S_{min}, and $\langle S \rangle$ denote the maximum, minimum, and mean, respectively, of the spectral profile $\mu_Y(\beta)$. That is,

$$S_{max} = \max(\mu_Y(\beta)) \qquad (4.8)$$

$$S_{min} = \min(\mu_Y(\beta)) \qquad (4.9)$$

$$\langle S \rangle \;\; = \frac{1}{4\pi} \int_0^{4\pi} \mu_Y(\beta) d\beta, \qquad (4.10)$$

as illustrated in Figure 4.3. Implicit is the assumption that any combination technique includes a magnitude operation to form the final image, so that $\mu_Y(\beta)$ is real-valued and positive. The integral defining $\langle S \rangle$ runs from 0 to 4π since SSFP off-resonance profiles have a periodicity in β of 4π[1], and any combined profiles will therefore share at least this periodicity. Angled brackets are used throughout to denote any such average across β.

---

[1]At an echo time TE $=$ TR/2, the magnitude of an SSFP off-resonance profile has a periodicity in β of 2π, while the phase has a periodicity in β of 4π.
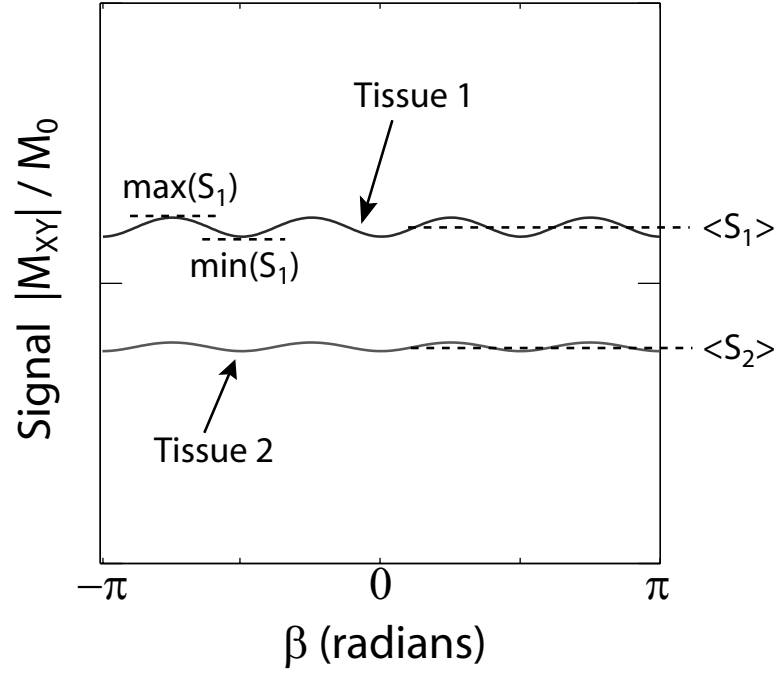
Figure 4.3: None of the combination methods produces a perfectly homogeneous spectral profile. The residual ripple can be predicted by examining the variations in the expected signal profile with free-precession angle β. Likewise, average expected signal (where the average is across β) can be used to predict the contrast resulting from a given combination technique.

Now define the percent ripple across the profile as:

$$\% \text{ ripple} = 100 \times \frac{(S_{max} - S_{min})}{\langle S \rangle}, \tag{4.11}$$

The percent ripple as defined provides a good measure of the ability of an SSFP combination technique to reduce off-resonance banding artifact. Note that the percent ripple will vary considerably with T_1, T_2, and α. Any comparison of multiple-acquisition techniques should examine a range of T_1 and T_2 value pairs expected to be present in the region to be scanned, and should perform the calculations at the appropriate flip angles. The theoretical performance is graphed across a range of tissue parameters for $\alpha = 30°$ and $60°$ in the *Results* section of this work.

The contrast between two tissues is defined as the ratio of the signal difference between the two tissues to their average signal. That is, the contrast between tissues A and B is given by:

$$C_{AB} = 2 \cdot \frac{\langle S_A \rangle - \langle S_B \rangle}{\langle S_A \rangle + \langle S_B \rangle} \tag{4.12}$$

where $\langle S_A \rangle$ and $\langle S_B \rangle$ are the mean signal magnitudes of tissues A and B respectively. Again, all averages denoted by angled brackets are across β (off-resonance free-precession angle per TR).

Note that contrast as defined above does not take into consideration the effect of noise on tissue differentiation. For this reason, a contrast-to-noise ratio (CNR) is often cited, defined as the ratio of the signal difference between two tissues to the standard deviation of the noise. The decrease in SNR efficiency that accompanies each multiple-acquisition technique will clearly reduce the CNR of a multiple-acquisition image when compared with a center-passband SSFP scan of the same duration. However, this information is already captured in an SNR analysis of each technique. The definition of contrast given above instead captures the "fundamental" contrast of a technique, independent of signal gain and noise.

Note that obtaining the mean tissue signal by averaging across β implicitly assumes that the variations in β across the region of interest are evenly distributed across a full period of the spectrum. This is clearly not entirely accurate, but is a convention adopted in order to concisely define contrast and SNR in multiple-acquisition SSFP. The error associated with this definition of average signal decreases as the banding artifact is more effectively removed (leading to less signal variation, or ripple, with variations in β).

4.2.4 SNR and SNR Efficiency

The SNR of a reconstructed voxel with free-precession frequency β is given by

$$SNR_Y(\beta) \equiv \frac{\mu_Y(\beta)}{\sigma_Y(\beta)}, \tag{4.13}$$

where μ_Y and σ_Y denote the mean and standard deviation of Y respectively. However, variations in β across a region of interest are generally not known *a priori*. It is therefore useful to consider the average of $SNR_Y(\beta)$ across one period in β. The off-resonance profile of an individual phase-cycled SSFP acquisition has a period in β of 4π, so $SNR_Y(\beta)$ will share at least this periodicity. Thus,

$$\langle SNR_Y \rangle \equiv \frac{1}{4\pi} \int_0^{4\pi} SNR_Y(\beta)d\beta = \frac{1}{4\pi} \int \frac{\mu_Y(\beta)}{\sigma_Y(\beta)}d\beta \qquad (4.14)$$

Again, the definition of $\langle SNR_Y \rangle$ implicitly assumes an even distribution of β across a full period over the region of interest.

Perhaps a more useful metric when comparing scanning techniques of different lengths is the SNR efficiency, denoted here by η. SNR efficiency is a measure of the SNR normalized by the square root of the total scan time. In the present case, an average SNR efficiency across β is defined as

$$\langle \eta_Y \rangle \equiv \frac{\langle SNR_Y \rangle}{\sqrt{\text{total scan time}}}. \qquad (4.15)$$

Use of SNR efficiency allows a fair SNR comparison between single-acquisition SSFP and multiple-acquisition techniques with N times the total scan time.

Measurements of SNR from actual images generally estimate signal noise from the background noise measured in a region of no signal. Accurate estimation requires the use of a correction factor CF, which relates the signal noise variance to measured background noise variance. CF varies with reconstruction method. *Appendix B* details the computation of CF for each multiple-acquisition technique.

4.3   Methods

4.3.1   Implementation of Framework

A Matlab (*The MathWorks, Inc.*, Natick, MA, USA) function was written to compute the transverse magnetization profile across one period in β as a function of T_1, T_2, proton density ρ, flip angle α, TR, TE, and the phase cycle increment $\Delta\phi$. This function provided the phase-cycled spectra $M_{XY,1}(\beta), \ldots, M_{XY,N}(\beta)$ needed to perform the statistical analysis.

A full analytical analysis would quickly become intractable, so further Matlab functions were written to numerically perform the statistical analysis outlined in *Theory*. For each combination scheme, a function computes the probability density function (PDF) for a reconstructed voxel as a function of tissue parameters, sequence parameters, SNR_{SSFP}, and β. The mean $\mu(\beta)$ and the standard deviation $\sigma(\beta)$ were in each case determined from the PDF.

Further Matlab functions computed residual banding and average SNR from $\mu(\beta)$ and $\sigma(\beta)$, as well as the correction factors CF_{MI} and CF_{SOS} (see *Appendix B*) for the MI-SSFP and SOS-SSFP cases.

A partial verification of the theory (and of the implementation of the statistical computations) was performed by generating simulated SSFP images. Each image contains three tissues ($T_1/T_2 = 300/150$ ms, $300/90$ ms, and $900/90$ ms). Signal levels were computed from the theoretical spectral profiles for each tissue with TR/TE = $10/5$ ms and $\alpha = 60°$. Figure 4.4(a) shows a center-passband SSFP image: that is, tissue signal levels are taken from the center of the spectral passband. Bivariate Gaussian noise was added to the images such that SNR_{SSFP} of the brightest (top) tissue was 15.0. Figure 4.4(b) shows a series of four phase-cycled SSFP images, where a variation in β is applied in the horizontal direction across the images to yield banding. These images were then combined with each combination method.

Theoretical predictions were obtained using the framework for average SNR, contrast, and measurement correction factor for each method. Measurements of average

(a) Single SSFP

	Theoretical	Measured
Tissue 1 <SNR>	15.0	15.0
Tissue 2 <SNR>	11.8	11.8
Tissue 3 <SNR>	5.8	5.9
Contrast 1:2	0.24	0.24
Contrast 1:3	0.89	0.88
Contrast 2:3	0.69	0.68

(b) Phase-cycled SSFP

(c) Max Intensity

	Theoretical	Measured
Tissue 1 <SNR>	20.3	20.5
Tissue 2 <SNR>	15.1	15.3
Tissue 3 <SNR>	7.4	7.6
Contrast 1:2	0.25	0.26
Contrast 1:3	0.89	0.88
Contrast 2:3	0.68	0.67

(d) Complex Sum

	Theoretical	Measured
Tissue 1 <SNR>	19.3	19.5
Tissue 2 <SNR>	14.8	14.9
Tissue 3 <SNR>	6.5	6.7
Contrast 1:2	0.27	0.27
Contrast 1:3	0.99	0.98
Contrast 2:3	0.77	0.77

(e) Sum of Squares

	Theoretical	Measured
Tissue 1 <SNR>	26.8	27.5
Tissue 2 <SNR>	19.8	20.4
Tissue 3 <SNR>	9.0	9.4
Contrast 1:2	0.30	0.30
Contrast 1:3	1.00	0.99
Contrast 2:3	0.76	0.74

Figure 4.4: (a) Simulated center-passband SSFP phantom with three tissues (T_1/T_2 = 300/150, 300/90, and 900/90 ms, $\alpha = 60°$, and TR/TE = 10/5 ms). Bivariate Gaussian noise was added to the complex image data such that $SNR_{SSFP} = 15.0$ for the top tissue. (b) Series of four such simulated phantoms with a variation in β induced in the horizontal direction. (c-e) Images resulting from the combination of four phase-cycled images. In each case, the model was used to predict the expected theoretical average SNR and contrast. The tables compare the theoretical values with those measured from each image.

SNR and contrast were then made on the combined images, and compared with theory. In each case, the measured values of average SNR were corrected by the theoretically predicted measurement correction factor. The theoretical and measured values are compared in the tables in Figure 4.4(c-e), and are in excellent agreement.

It should be noted that this experiment only validates the theory inasmuch as the simulated phantom images correspond to actual phase-cycled SSFP images. In practice, a detailed and accurate empirical verification of the theory is difficult to perform using actual MR images. Accurate values of T_1, T_2, and the flip angle are needed to determine the theoretical signal level and spectral profile for a tissue. While T_1 and T_2 may be known quite accurately, the flip angle can vary significantly across a slice due to an imperfect slice profile and B_1 inhomogeneity. Furthermore, intravoxel dephasing (arising from off-resonance within a voxel) can cause undesired signal loss, leading the measured signal levels to fall short of theory. Finally, an accurate empirical determination of SNR_{SSFP} from actual images can be difficult to obtain. Off-resonance variations often make the measurement of a suitable sample of center-passband voxels challenging.

That said, a simple comparison of average SNR for a tissue of known characteristics can still be performed. Verification that measurements of average SNR are roughly consistent with those predicted by theory is thus obtained. Figure 4.5 shows one such comparison. In (a), a single SSFP acquisition exhibiting banding artifact is seen. A measurement of SNR was performed across a region of muscle deemed to be roughly at center-passband. This value was used for SNR_{SSFP} in a subsequent prediction of muscle SNR using each method for $N = 4$. Phase-cycled images were then combined with each method, and measurements of muscle SNR taken. The theoretical and measured values are compared below each image, and are in reasonably good agreement. Interestingly, the measured and theoretical values are in much better agreement if the predictions are performed assuming a flip angle of 22° rather than the nominal 25°. This is likely the result of B_1 inhomogeneity across the slice.
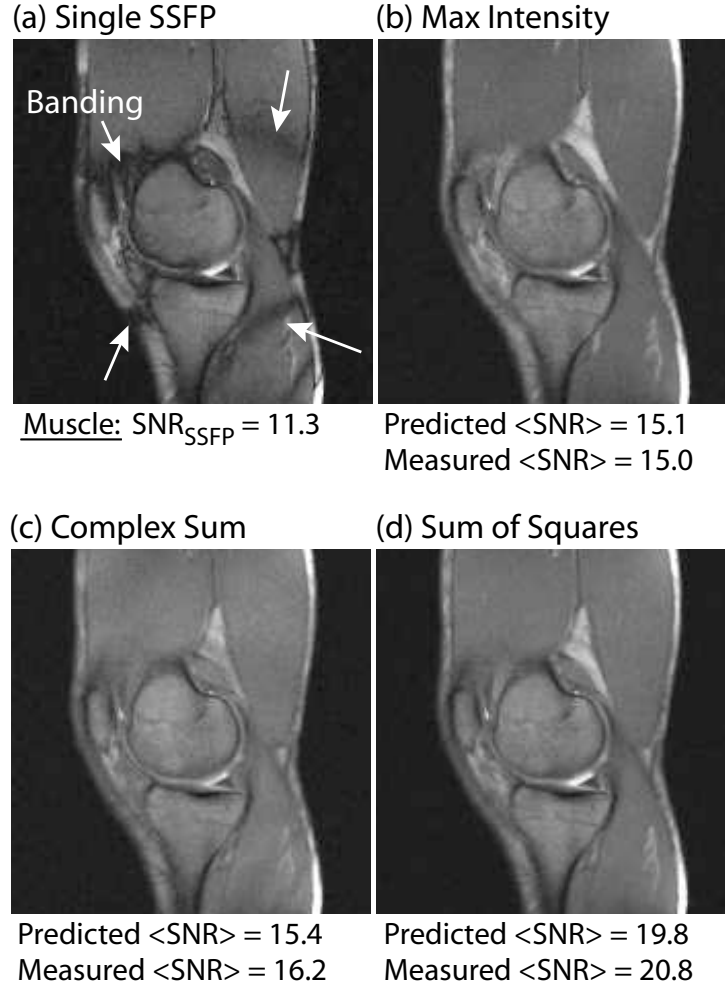
Figure 4.5: (a) Single SSFP acquisition (sagittal knee) exhibiting banding artifact (arrow), TR/TE = 10/5 ms, FOV = 28 cm, $\alpha = 25°$. A measurement was performed in the center-passband region to determine SNR_{SSFP} of muscle. (b-d) show the resultant images when four SSFP acquisitions were combined with each technique ($N = 4$). Predictions of average muscle SNR were in each case performed using muscle $T_1/T_2 = 870/47$ ms and $\alpha = 25°$. Measurements of average muscle SNR were then performed (correcting the measurements with the theoretically predicted correction factors). The results are shown below each image, and are in reasonably good agreement, although the complex-sum and sum-of-squares predictions are somewhat lower than those measured. This is likely due to the actual flip angle across the slice varying slightly from the nominal flip angle of 25°. The measured results are in much better agreement with a prediction based on $\alpha = 22°$.

N	2, 4, 8
α	30º, 60º, 90º
SNR$_{SSFP}$	5, 10, 15, 20, 25
T1	300 - 2300 ms (200 ms increments)
T2	30 - 230 ms (20 ms increments)

Table 4.1: Parameter ranges used for data generation.

4.3.2 Data Generation

To get a better sense of the overall performance of each combination method, the model was applied across a range of tissue and sequence parameters that span those typically arising in practice.

The performance of each technique will clearly depend on the shape of the magnetization profile, which will in turn depend heavily on α and T_1/T_2. It is therefore important to generate data for a variety of values of α, T_1, and T_2. One would also like to know how the performance varies with SNR_{SSFP} and with N. To this end, data were generated for the parameter ranges shown in Table 4.1. For each combination of parameters, residual banding (percent ripple), average SNR ($\langle SNR \rangle$), average signal ($\langle S \rangle$), and measurement correction factor (CF) were calculated.

All simulations employed TR/TE = 10/5 ms. To make the data analysis tractable, variations in TR were not considered. This is justified for TR less than approximately $T_2/4$, where the shape of the off-resonance profile changes very little with changes in TR.

The calculations for each parameter combination were repeated for MI-SSFP, CS-SSFP, and SOS-SSFP. The residual banding and average SNR results allow comparison of the banding artifact reduction and SNR performance of the various techniques across a broad range of parameters. The average signal results were used to perform contrast comparisons. Finally, the average correction factors enable comparison with SNR measurements on actual magnitude images. The salient results are summarized below.
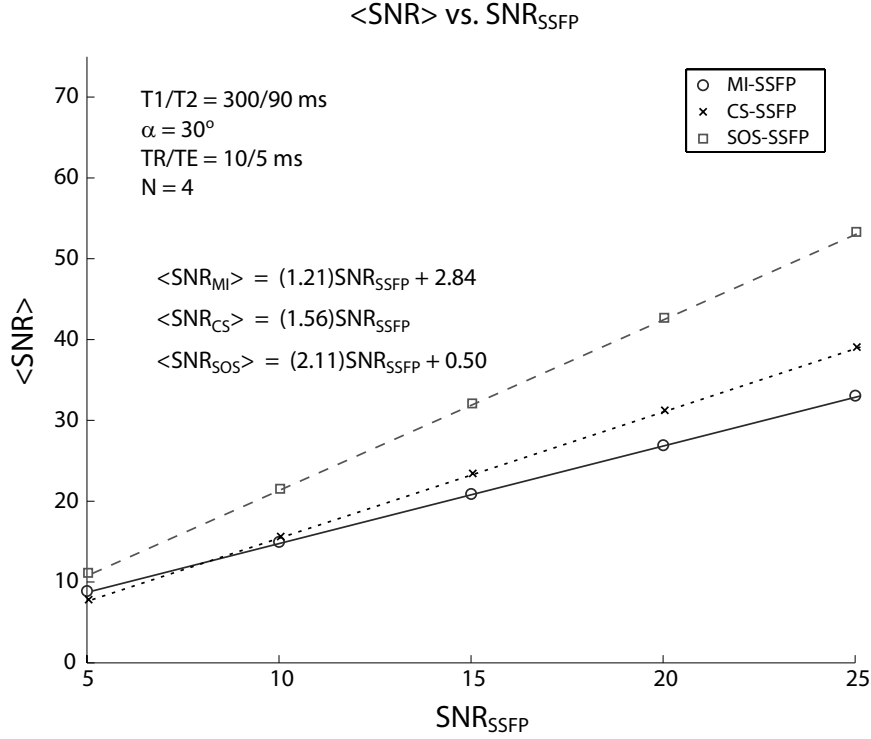
Figure 4.6: Graph of average SNR versus SNR_{SSFP} for each combination method. Average SNR is linear to a very good approximation in SNR_{SSFP}. Although the results for only one tissue and set of sequence parameters are shown, the linear relationship is very accurate across a broad range of T_1, T_2, N, and α.

4.4 Results

To make the interpretation of the large resultant data set tractable, trends were identified that could be generalized across the entire dataset.

First, it was observed that average signal and residual banding do not depend heavily on SNR_{SSFP}. In fact, in the complex-sum case there is virtually no dependence. The dependence is stronger at low SNR for the maximum-intensity SSFP case. However, in the range considered here ($SNR_{SSFP} \geq 5$), the variations are negligible. One therefore need not consider variations in SNR_{SSFP} when discussing band reduction. SNR_{SSFP} only enters into play when predicting average SNR and CNR.
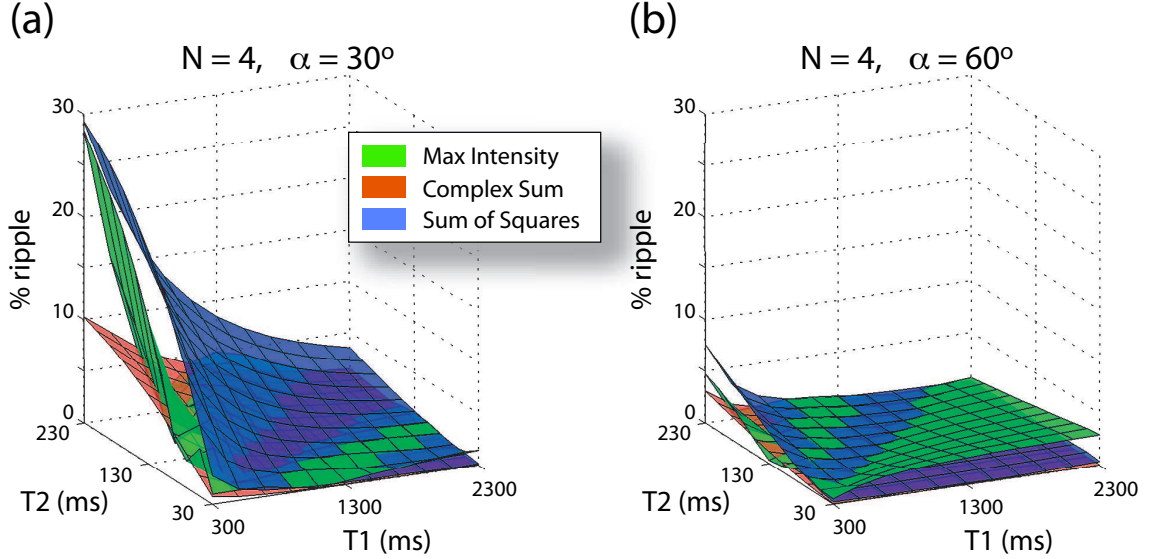
Figure 4.7: Comparison of residual banding as a function of T_1 and T_2. (a) shows the residual banding at $N = 4$ and $\alpha = 30°$, while (b) shows the effect of increasing the flip angle to 60°. Notice that the banding can be very pronounced for tissues with small T_1/T_2 at a low flip angle. While complex sum is the most robust at removing residual banding, in practice the banding reduction achieved with SOS-SSFP at $N = 4$ and $\alpha \geq 30°$ is adequate for most tissues.

A second trend observed is that $\langle SNR \rangle$ for the different combination techniques is linear to an excellent approximation in SNR_{SSFP} for $SNR_{SSFP} \geq 5$. This is illustrated for one set of sequence and tissue parameters in Figure 4.6. For very low values of SNR_{SSFP}, the linearity in the MI-SSFP and SOS-SSFP cases will break down. The slope of the SOS-SSFP line was also uniformly larger than the other two methods. These observations are important in that they enable $\langle SNR \rangle$ to be summarized at a single value of SNR_{SSFP}, expecting that the results will roughly scale with SNR_{SSFP}.

4.4.1 Banding

Figure 4.7 shows   residual banding for the $N = 4$ case as a function of T_1 and T_2

for each combination method. Results are shown for flip angles of 30° and 60°, with $SNR_{SSFP} = 15$ and TR/TE = 10/5 ms. Notice that the banding artifact reduction improves significantly with increasing flip angle for all of the methods. This is due to the change in shape of the off-resonance spectra as flip angle is increased, as illustrated in Figure 4.1. At low flip angles, tissues with small T_1/T_2 are characterized by large "humps" at the edges of the passband. As flip angle is increased, this bimodal shape tends to smooth out into a single hump. The latter shape is much more easily smoothed through combination techniques than the bimodal shape.

The graph shown in Figure 4.7(a) ($\alpha = 30°$) shows quite severe banding (almost 30 percent in the SOS-SSFP case) for some T_1, T_2 combinations (more precisely, for small T_1/T_2). *In vivo*, the residual banding of SOS-SSFP at $N = 4$ is often almost imperceptible, even at $\alpha = 30°$. Most real tissue T_1/T_2 values lie in the low ripple region. This is illustrated in Figure 4.8(a). Axial head images at $\alpha = 30°$ are shown for both normal fluid-suppressed SSFP [31, 32] (left) and $N = 4$ SOS-SSFP (also fluid-suppressed) (right). Signal averaging of four acquisitions was used to form the left image, so as to normalize scan time for the two images. Residual banding can be detected in the SOS-SSFP image, but is not severe.

At higher flip angles ($\alpha \geq 60°$) SOS-SSFP is very good at removing banding (Figure 4.7(b)), and actually outperforms MI-SSFP for most T_1, T_2 combinations. Figure 4.8(b) illustrates the sum-of-squares method at $\alpha = 70°$ (right). Residual banding is virtually imperceptible. The degree of gray/white matter contrast is also increased at this higher flip angle.

4.4.2 SNR Efficiency

Figure 4.9 shows a comparison of average SNR efficiency $\langle \eta \rangle$ as a function of T_1 and T_2 for the $N = 4$ case, at flip angles of 30° and 60°, $SNR_{SSFP} = 15$, and TR/TE = 10/5 ms. In both cases, the average SNR efficiency obtained with SOS-SSFP is significantly higher than the other two cases (often more than 30 percent higher). In fact, SOS-SSFP outperforms the other two methods in SNR efficiency in virtually

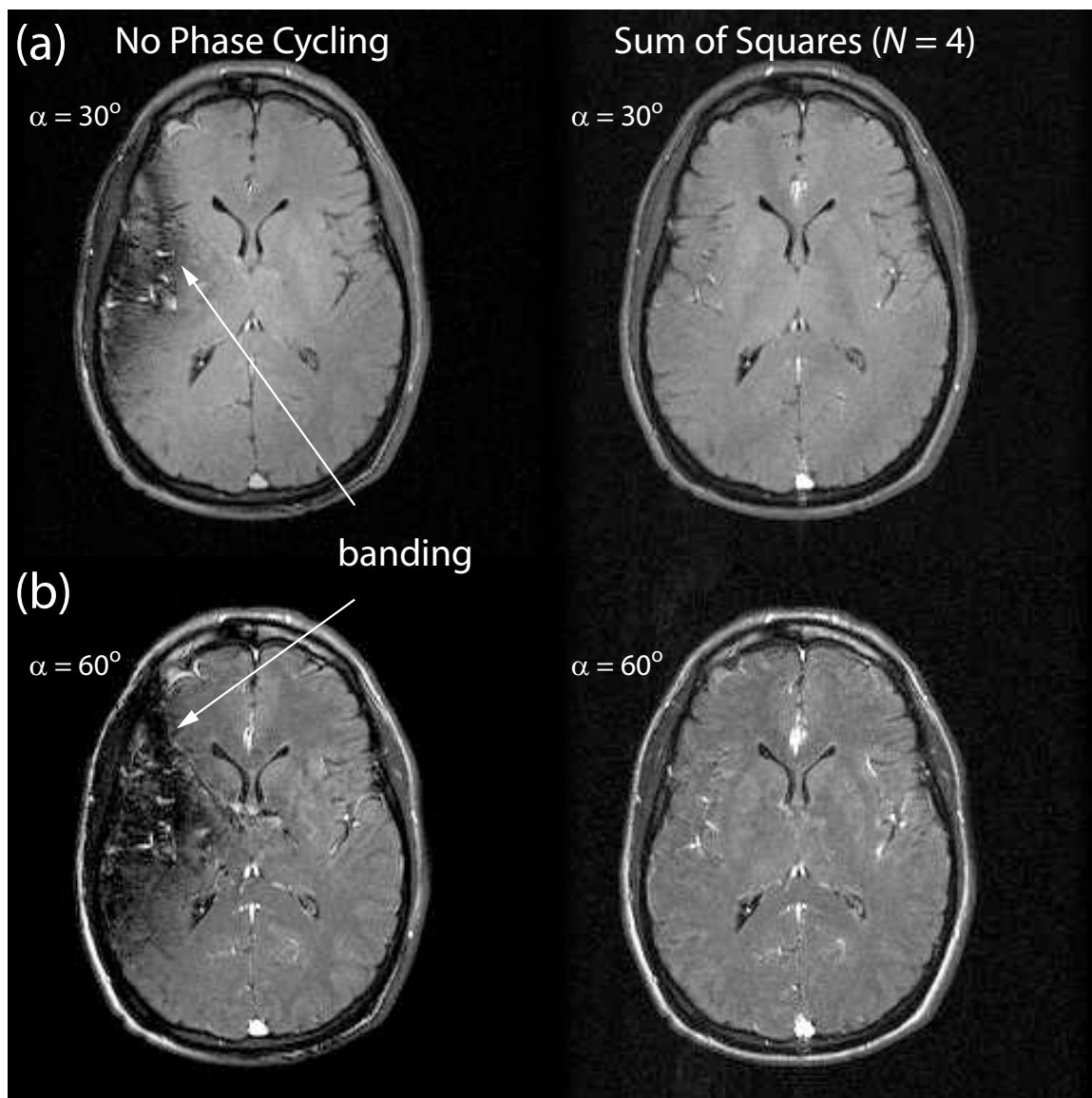Figure 4.8: (a) Axial fluid-suppressed SSFP acquisition of brain (left) and $N = 4$ sum-of-squares combination (right) at $\alpha = 30°$. (b) Same, with flip angle increased to 70°. Signal averaging of four single-acquisition SSFP images was used to produce each of the images on the left, to normalize scan time for all images. TR/TE = 8.0/4.0 ms, TI = 2.0 s, FOV = 24 cm, 256×192 matrix, 5 mm slice thickness.
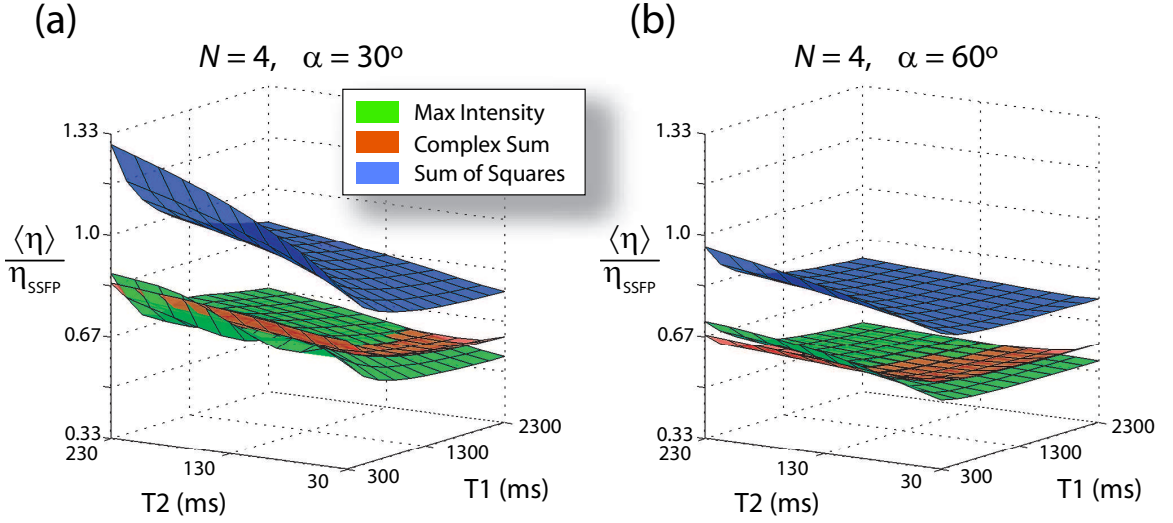
Figure 4.9: Comparison of average SNR efficiency as a function of T_1 and T_2, relative to SNR efficiency of center-passband SSFP (η_{SSFP}). (a) shows average SNR efficiency for each combination method at $N = 4$ and $\alpha = 30°$. (b) shows the effect on average SNR efficiency of increasing the flip angle to 60°. In both cases, the average SNR efficiency obtained with the sum-of-squares method is significantly higher than the other two cases. This result holds across virtually all of the test cases considered.

every one of the test cases (at $N = 2$, 4, and 8, at $\alpha = 30°$, 60°, and 90°, and for the full range of values of SNR_{SSFP} considered).

The SNR performance of MI-SSFP and CS-SSFP at $N = 4$ is similar. For $N = 2$, maximum intensity performed slightly better than complex sum. The opposite was true at $N = 8$, where complex sum outperformed maximum intensity by a slightly better margin. These results are consistent across the range of α and SNR_{SSFP} considered.

4.4.3 Contrast

What effect does each combination scheme have on fundamental image contrast, relative to that expected from center-passband SSFP? To visualize contrast variations,
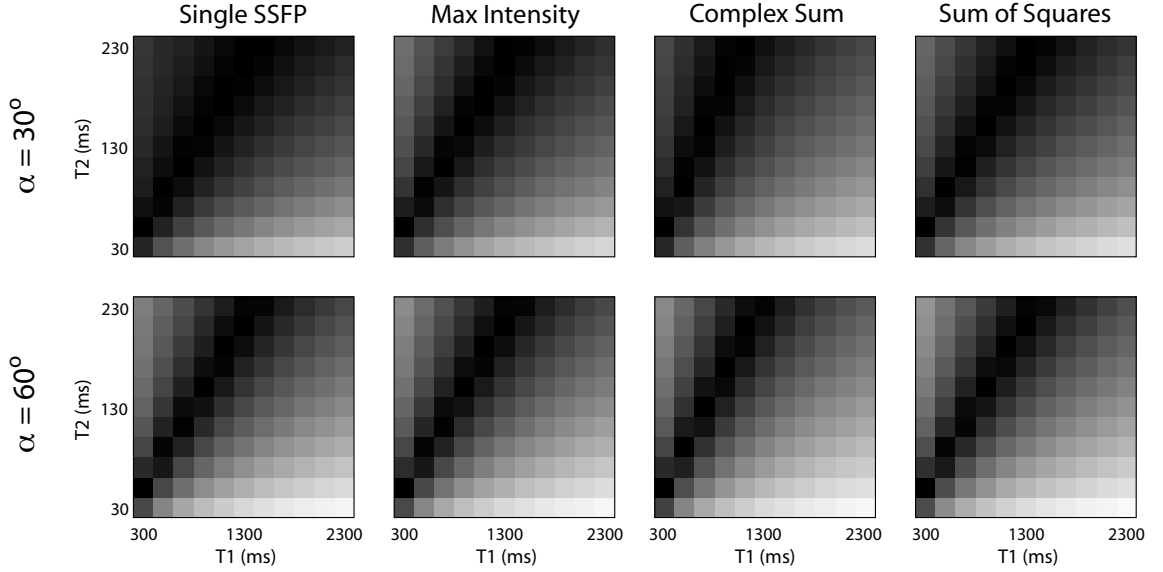
Figure 4.10: (a) shows contrast as a function of T_1 and T_2 for $N = 4$ and $\alpha = 30°$, while (b) plots the same at $N = 4$ and $\alpha = 60°$. The contrast is measured against a reference tissue with $T_1/T_2 = 500/70$ ms. All plots utilize the same grayscale, with black indicating no contrast and white indicating the largest contrast observed. Plots were generated with TR/TE = 10/5 ms and $SNR_{SSFP} = 15$.

contrast as a function of T_1 and T_2 was plotted, with contrast at each T_1, T_2 pair computed against a reference tissue. Graphs of this type for each technique (center-passband, MI-, CS-, and SOS-SSFP) are shown in Figure 4.10 at $N = 4$ for flip angles of 30° and 60°. The reference tissue has $T_1/T_2 = 500/70$ ms.

Very little fundamental contrast variation between each method is observed. The slight variations seen will not have a significant effect on image appearance. For other values of reference tissue, the contrast graphs show similar characteristics: i.e., very little change between the multiple-acquisition methods, and only slight contrast variation from that of center-passband SSFP. Likewise, there are only slight variations at $N = 2$ and $N = 8$.

One can understand the slight variation in contrast for small T_1/T_2 values by looking at the shape of the off-resonance spectra. For small T_1/T_2, the off-resonance spectrum exhibits more pronounced "humps" at the edges of the passband, as discussed

	T1 / T2 (ms)	Tissue (approximate)
1	850 / 52, 54, ..., 90	
2	1000 / 200	blood
3	500 / 45	liver
4	450 / 75	
5	850 / 50	muscle
6	925 / 100	gray matter
7	790 / 95	white matter
8	4000 / 1600	CSF
9	270 / 85	fat
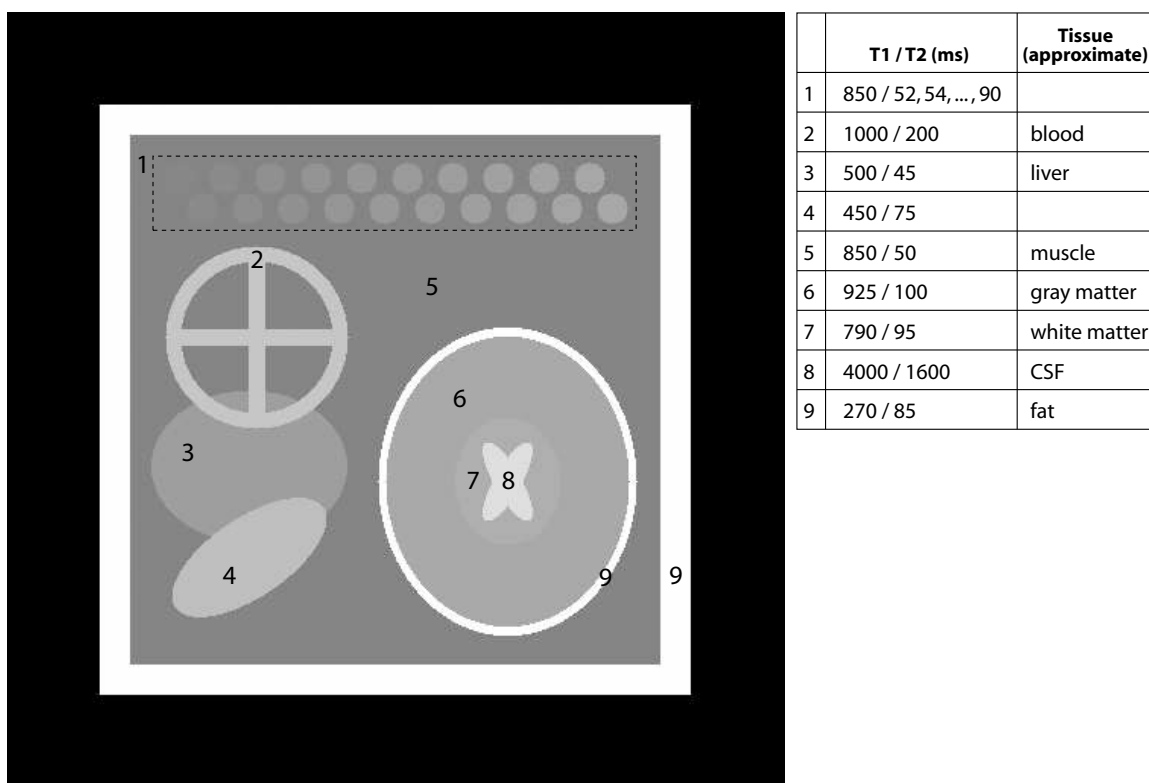
Figure 4.11: Simulated contrast phantom on 512×512 matrix, exhibiting center-of-passband SSFP contrast. Relevant tissue parameters used to generate the phantom are shown.

in the *Banding* subsection. Variations in the magnitude of these humps is much more pronounced with changes in T_1/T_2 than the center-passband signal. Center-passband SSFP only samples the center-passband signal, while the multiple-acquisition techniques derive information from a full period of the off-resonance spectrum.

The fundamental contrast should not be confused with the contrast-to-noise ratio. Each of the multiple-acquisition techniques carries with it a degradation in SNR when compared to a center-passband SSFP scan of the same duration. This will lead to a corresponding degradation in CNR.

To better visualize the contrast effects of each technique, simulated phantom images containing a variety of tissues were generated on a 512×512 matrix. The

simulation allowed the generation of both center-of-passband SSFP images, as well as images exhibiting off-resonance banding (or variations in β across the image). For each tissue, off-resonance spectra were generated, which then were used to generate the phantoms. The phantom generation tool takes as an input TR, TE, flip angle, and the phase cycling value $\Delta\phi$. Fat sections of the phantom were given the appropriate spectral offset, which varies the relative position of the fat and water nulls with TR. A reference tissue SNR_{SSFP} is also passed into the phantom generating tool, from which bivariate Gaussian noise of the appropriate magnitude is generated. A phantom labeled with tissue parameters is shown in Figure 4.11.

Figure 4.12 shows the combination of $N = 4$ simulated phantoms using each technique (TR/TE = 10/5 ms, $\alpha = 60°$, $SNR_{SSFP} = 15.0$ for fat). For reference, a center-passband SSFP image is shown, formed from four center-passband constituent images to make theoretical acquisition time equal in all cases. In these images, some very slight contrast variations can be ascertained. The SNR improvement of SOS-SSFP over MI- and CS-SSFP is also apparent from the simulations.

In summary, the contrast variations between each combination method are small for the range of parameters examined in this study. Fundamental contrast is slightly enhanced with each combination method over the ideal SSFP case.

4.5   Discussion

The results indicate that sum-of-squares SSFP yields significantly higher SNR efficiency than either of the other two methods. A simple intuitive argument can help one understand why this is true. In each method, N signal observations are obtained for any given pixel. Although each of the N observations is measuring the same tissue, the phase-cycling varies from observation to observation. Hence each observation will give a different signal level, depending on where that observation falls on the off-resonance spectrum. If one of the observations falls near the off-resonance null, very low signal is expected. An observation in the pass-band should give relatively high signal.
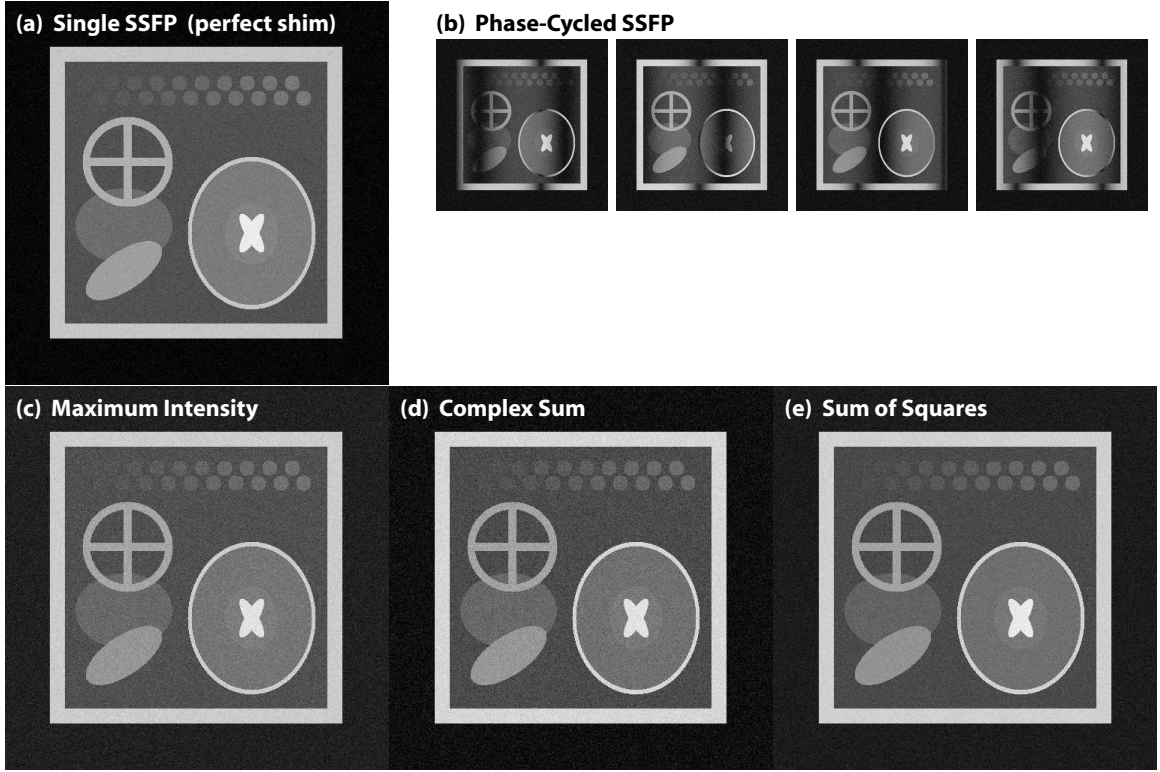
Figure 4.12: Comparison of combination techniques on simulated phantoms at $N = 4$. (a) shows a center-passband SSFP image, formed from four center-passband constituent images. (b) shows the individual phase-cycled acquisitions, with a linear variation in β introduced in the horizontal direction. (c-e) are the images formed from the combination of images shown in (b) using each technique. TR/TE $= 10/5$ ms, $\alpha = 60°$, SNR_{SSFP} of lipid $= 15$.

Despite the signal variations, the same error in each of the N observations is expected. Observations with higher signal will therefore have a higher SNR than observations with lower signal, and should be weighted more if SNR is to be maximized in the reconstructed image. So what should each observation be weighted by? Since noise is constant across observations, a higher observed signal should correspond to a higher weighting in the sum. Each observation is simply weighed by its observed signal, or the constituent acquisitions squared, thereby giving higher weight to observations with higher SNR. The square root operation at the end is needed to normalize contrast.

At this point, one might ask if this is the most optimal solution given the information available. Weighting each observation by its observed value is only optimal if each observation is independent of all the others. However, this is not the case. Off-resonance profiles have a relatively regular shape. Although one does not know *a priori* what off-resonance value corresponds to a given observation, a set of phase-cycled observations taken together could be fit to a computed off-resonance profile shape, yielding both additional off-resonance frequency and tissue T_1/T_2 information. Observations might then be weighted more optimally using the additional information. It is questionable, however, whether the additional complexity would justify any gains in SNR efficiency.

There are several other useful observations and generalizations that follow from the analysis and results. First, total scan time is clearly an issue when using multiple-acquisition techniques. While the SNR efficiency of the sum-of-squares method may approach that of center-passband SSFP, the minimum scan time possible is always N times that of single-acquisition SSFP. Choice of N is therefore constrained by total scan time limits.

If scan time constraints only allow the use of two phase-cycled acquisitions, maximum-intensity SSFP is the most effective at removing SSFP banding. However, for tissues with small T_1/T_2 values or at low flip angles, the percent residual ripple can still exceed 30 percent. At $N = 8$ all of the techniques are quite robust at removing SSFP banding, but scan times can be prohibitively long.

If time allows, the $N = 4$ sum-of-squares case is a good choice. SSFP banding artifact reduction at $N = 4$ with sum-of-squares is quite robust in practice, and the SNR efficiency is significantly higher than the other two combination methods. Relatively quick scan times can still be achieved for many applications. If slightly better band elimination is required, complex-sum SSFP can be used, albeit with an accompanying SNR penalty.

4.6   Conclusion

Many applications could benefit from the contrast and high SNR efficiency of SSFP, but are limited by its high sensitivity to local field variations (seen as bands of signal loss in an image). This sensitivity places an upper limit on the sequence repetition time TR, which can be difficult to comply with at high fields, high resolutions, or when longer excitation and gradient pulses are required.

Multiple phase-cycled SSFP acquisitions can be combined in various ways to eliminate SSFP banding artifact. These include performing a maximum-intensity, complex-sum, or sum-of-squares combination of the constituent acquisitions. If N phase-cycled acquisitions are acquired, the penalty for band elimination is a loss in SNR efficiency and an N-fold increase in total scan time over a single SSFP acquisition. A straightforward statistical analysis can be applied to examine the banding artifact reduction, SNR efficiency, and contrast of each method.

Each of the combination methods has a negligible effect on fundamental image contrast, but they vary in performance with respect to banding artifact suppression and SNR efficiency. Although maximum-intensity and complex-sum SSFP generally yield better band reduction than sum-of-squares SSFP, the sum-of-squares method yields approximately 30% higher SNR efficiency, while still achieving good SSFP band removal, particularly at higher flip angles. Combination of four phase-cycled acquisitions with any of the techniques is sufficient for robust band removal in many applications.

Chapter 5

2D Fluid-Attenuated Inversion Recovery SSFP

5.1 Introduction

Fluid-attenuated neuroimaging techniques offer contrast that is helpful in detecting periventricular and subcortical lesions, particularly in cases of inflammatory, traumatic, and demyelinating diseases [33, 34]. T_2-weighted fluid-suppressed sequences are particularly effective, due to the elevated T_2 of many of these lesions. Without fluid-suppression, strong signal from cerebrospinal fluid (CSF) may hamper the distinction of pathology from normal brain parenchyma. By far the most common imaging modality currently employed in periventricular and subcortical lesion detection is T_2-weighted FLAIR FSE (fluid-attenuated inversion-recovery fast spin-echo), yielding good CSF signal suppression and elevated-T_2 lesion conspicuity.

Fully-refocused steady-state free precession (SSFP) has been gaining popularity as advances in gradient hardware have made possible SSFP sequences with very short repetition time TR [20]. As discussed earlier, short TRs are desirable in SSFP sequences to reduce off-resonance banding artifacts [17, 18]. These sequences yield very high SNR efficiency in short scan times with T_2-like contrast. SSFP has historically

not been used in neuroimaging for several reasons. First, the degree to which TR
can be reduced is limited by RF power deposition, gradient strength and speed, and
peripheral nerve stimulation considerations. Even at the lowest feasible pulse repeti-
tion rates attainable, field inhomogeneity in many regions of interest can still cause
serious banding artifacts. Second, no fluid-attenuated SSFP sequences are available.
The T_2/T_1 contrast of SSFP sequences gives very bright CSF signal, hampering lesion
detection. Lastly, it is not clear that SSFP contrast, even in the presence of good
fluid suppression, is useful for neuroimaging.

Several techniques have been proposed [21, 22, 25] that can be applied to the
first challenge mentioned above: that of off-resonance banding artifact in regions of
high local field variation. These techniques are treated in detail in Chapter 4. The
characteristic SSFP banding artifact appears if the resonant frequency across the field
of view varies by more than about 2/(3TR) [27]. Even after the sequence repetition
rate TR is reduced as far as RF power deposition and peripheral nerve stimulation
considerations will allow, this condition may still not be met. In such cases, multiple
phase-cycled SSFP acquisitions can be combined to reduce banding artifact, albeit
with a concomitant increase in scan time (Chapter 4).

Fluid attenuation in SSFP can be achieved with a widely-used SSFP magnetization-
preparation technique first proposed by Deimling and Heid [7, 35–37]. In SSFP se-
quences, the signal level oscillates significantly after the excitations begin for a period
of time approximately equal to T_1 of the longest T_1 tissue present. Only after the sig-
nal oscillations die down can image acquisition begin without causing serious artifacts.
The transient period in most tissues is long enough that preparation to the initial mag-
netization is lost by the time the signal oscillations die down. Deimling and Heid pro-
posed a method for reducing the duration of the transient oscillations, thereby making
magnetization preparation possible. Fluid-suppressed inversion-recovery SSFP relies
on this "catalyzation" of the steady state.

In the current work, a fast fluid-suppressed 2D multi-slice SSFP sequence is presented (2D multi-slice FLAIR SSFP) [31, 32]. The sequence combines inversion-recovery (IR) prepared SSFP for fluid suppression and a multiple-acquisition technique to eliminate banding artifacts. A contrast analysis was performed, and volunteers were imaged to gauge the effectiveness of the technique.

5.2   Theory

5.2.1   Pulse Sequence

A timing diagram of the FLAIR SSFP sequence is shown in Figure 5.1. The sequence consists of a selective inversion pulse followed by a large G_z gradient lobe to dephase any transverse magnetization. After an inversion time TI, a single $\alpha/2$ pulse is inserted one full TR prior to the beginning of the α excitations. This is similar to the $\alpha/2$, TR/2 pulse proposed by Deimling and Heid [7], but has different off-resonance characteristics. The $\alpha/2$, full TR method does not reduce the near-resonance transient oscillations as well as the TR/2 method, but does reduce the oscillations over a broader range of off-resonance frequencies. Additional methods have been proposed for reducing the transient length over a broader portion of the off-resonance spectrum [9], and could be employed if more robust steady-state catalyzation is desired. Data acquisition starts on the excitation immediately following the $\alpha/2$ catalyzation pulse.

5.2.2   Signal and Contrast

The expected signal from excitation to excitation was simulated in Matlab (*The MathWorks, Inc.*, Natick, MA, USA) for gray matter ($T_1/T_2 = 920/100$ ms, proton density $\rho = 0.75$), white matter ($T_1/T_2 = 790/92$ ms, $\rho = 0.65$), CSF ($T_1/T_2 = 4000/2200$ ms, $\rho = 1.0$), and a lesion with augmented T_2 ($T_1/T_2 = 1300/175$ ms, $\rho = 0.8$). Note that the lesion parameters used are similar to those found in the
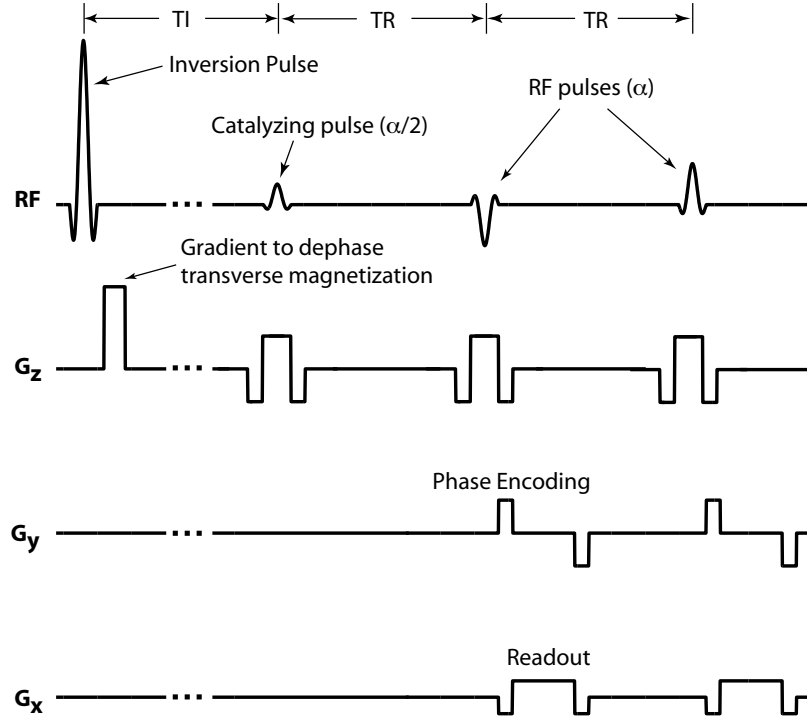
Figure 5.1: Timing diagram of fluid-attenuated SSFP sequence (FLAIR SSFP). The sequence consists of an inversion pulse followed by a large gradient lobe to dephase residual transverse magnetization. After an inversion time TI, a single $\alpha/2$ pulse is inserted one full TR prior to the beginning of fully-refocused SSFP excitations. Imaging commences immediately during the transient period to achieve good fluid suppression.

literature for multiple-sclerosis plaques [33]. Figure 5.2 shows the results of this simulation for TR = 3.6 ms, α = 70°, TI = 2.45 s, and 192 phase encodes for on-resonant spins. Data acquisition begins before the inversion null-point for CSF. The contrast is determined, to a good approximation, by the relative signal levels when the center of k-space is acquired. For short TR (less than approximately 10 ms) the contrast achieved will depend predominantly on flip angle, inversion time TI, and the ordering of the phase encodes. The value of these parameters should be chosen to maximize the contrast of interest while minimizing the CSF signal.
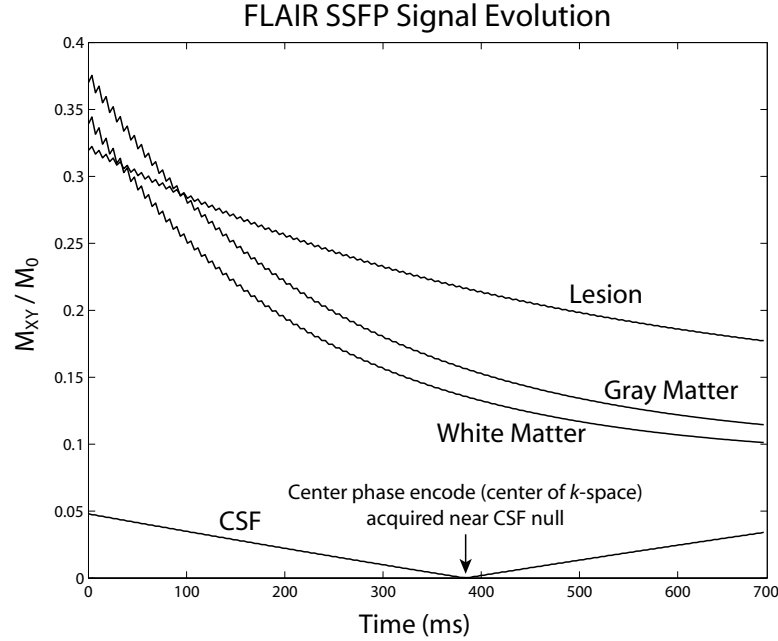
Figure 5.2: Simulated signal evolution from excitation to excitation for the FLAIR SSFP sequence. Signal levels for gray matter, white matter, CSF, and a white matter lesion are plotted. The simulation employed TR = 3.6 ms, flip angle $\alpha = 70°$, TI = 2.45 s, and shows the signal over 192 phase encodes. The center of k-space was acquired halfway through the phase encodes (on the 96th phase encode). As shown in the graph, these parameters yield good white matter/lesion contrast while suppressing the CSF signal.

The two grayscale plots shown in Figure 5.3 illustrate how variations in the flip angle and TI affect both (a) the contrast between white matter and a lesion with the aforementioned parameters, and (b) the ratio of the (suppressed) CSF signal to the steady-state CSF signal in FLAIR SSFP. Here (unlike in Chapter 4) contrast is defined as the magnitude of the signal difference between two tissues of interest. As can be seen, an inversion time TI of approximately 2.5 s yields excellent CSF suppression across a broad range of flip angles. Increasing the flip angle should give increasingly better white matter/lesion contrast.

This dependence of T_2 contrast on flip angle is typical of SSFP sequences. Figure 5.4(a) shows the steady-state SSFP contrast expected between white matter (T_1/T_2
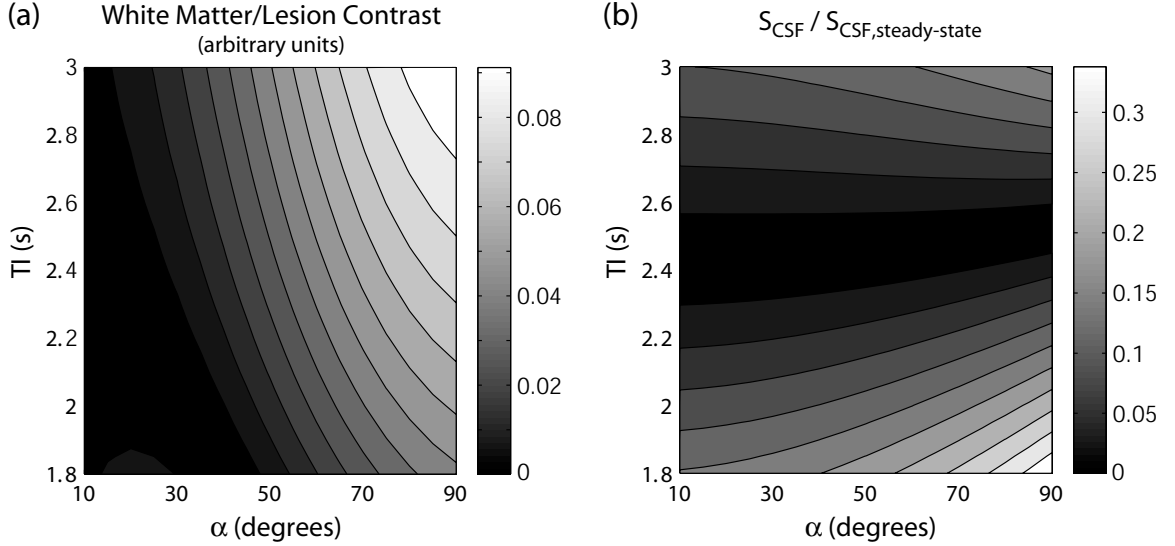
Figure 5.3: (a) Simulated FLAIR SSFP contrast between white matter ($T_1/T_2 = $ 790/92 ms, $\rho = 0.65$) and lesion ($T_1/T_2 = 1300/175$ ms, $\rho = 0.8$) as a function of inversion time TI and flip angle α. (b) Simulated CSF signal (as a fraction of the steady-state CSF signal) plotted for variations in TI and α. Both simulations employed TR = 3.6 ms and 192 phase encodes ordered such that the center of k_y-space was acquired halfway through the scan. As shown in (b), an inversion time of 2.5 s will yield excellent CSF suppression even at high flip angles. From (a), one sees that increasing the flip angle at this TI yields increasingly better lesion conspicuity.

= 790/92 ms, $\rho = 0.65$) and a lesion with T_1 fixed at 1000 ms and $\rho = 0.8$, where both T_2 and flip angle are varied. T_2 varies from 50 to 350 ms, while flip angle varies from 10° to 90°.

The fluid-attenuated SSFP sequence employs an inversion pulse prior to the SSFP excitations, and image acquisition begins before establishment of a steady state. This will clearly have an impact on image contrast. Figure 5.4(b) shows an analogous plot to that shown in Figure 5.4(a) for FLAIR SSFP. The center of k-space is acquired in this simulation on the 96th of 192 phase encodes. Tissue contrast is determined by the signal level when the center of k-space is acquired. At lower flip angles, a slight decrease in the degree of T_2 discrimination is seen as compared to the steady-state case. At higher flip angles a general improvement in T_2 discrimination is seen.
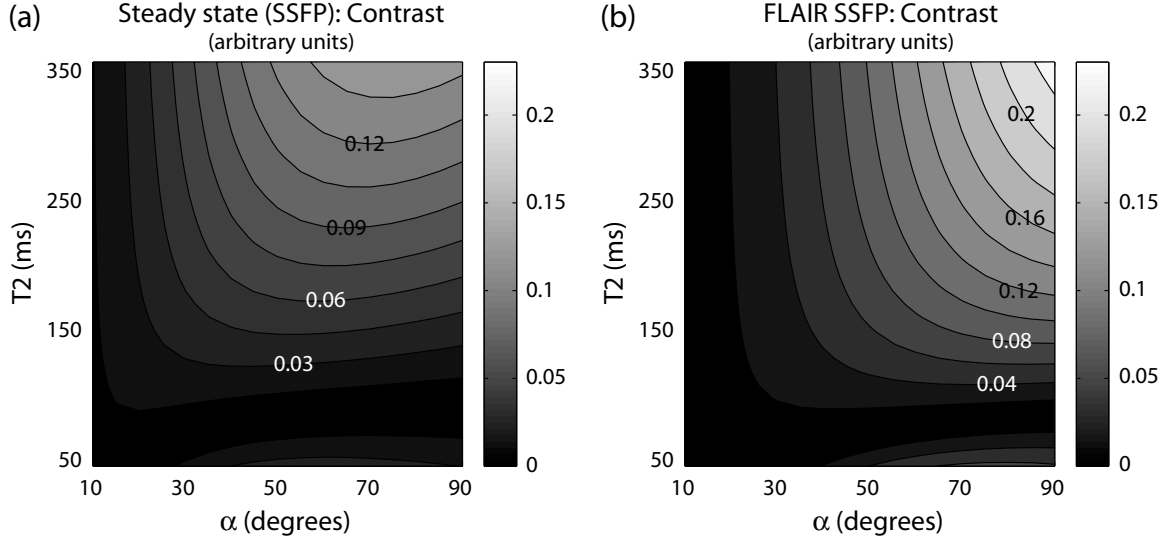
Figure 5.4: (a) Simulated steady-state SSFP contrast between white matter (T_1/T_2 = 790/92 ms, ρ = 0.65) and lesion (T_1 fixed at 1000 ms, ρ = 0.8), as a function of lesion T_2 and flip angle α. (b) White matter/lesion contrast for FLAIR SSFP. Both simulations employed TR = 3.6 ms. The FLAIR SSFP simulation used TI = 2.45 s and 192 phase encodes, with the center of k-space acquired on the 96th phase encode. The signal level was defined as the signal on the 96th phase encode.

It is important to note that these figures can be misleading. Steady-state SSFP signal levels are approximately a function of T_2/T_1 [10]. In the above analysis, a fixed T_1 value was considered, and T_2 allowed to vary. An augmented T_2 may be accompanied by an augmentated T_1, as is the case for MS plaques [38]. The ratio of T_2/T_1 thus varies less than it would were T_1 fixed, and contrast is degraded. Very little contrast between tissues with similar T_2/T_1 is expected, even if the T_2 values are quite different. For this reason, it is a good idea to perform an analysis such as that shown in Figure 5.3(a) to determine the optimal flip angle for a tissue contrast of interest.

5.2.3   Choice of Repetition Time TR

At this point, a discussion of the choice of TR is in order. As TR is shortened, the percentage of time during each TR that can be devoted to readout (or the "readout

duty cycle") is correspondingly reduced. The readout duty cycle is directly related to the overall SNR efficiency of the scan. At longer TR, the readout can occupy a higher percentage of the overall scan time, and SNR efficiency is improved. As the TR is shortened, the excitation and gradient balancing pulses and ramps occupy an increasing fraction of the total scan time, and SNR efficiency suffers. Gradient heating considerations may also place a lower limit on TR.

Increasing the TR to improve SNR efficiency has other undesired consequences. As TR is increased, the SSFP banding artifact becomes more severe. At a certain point, the banding becomes so pronounced that it is difficult to remove even with the multiple-acquisition techniques discussed below. A second obvious consequence of an increase in TR is a corresponding increase in overall scan time. Each of these considerations should be addressed when selecting TR and readout time for a given application.

5.2.4   Multiple Acquisition Techniques

Off-resonance banding artifacts can be a problem in human brain SSFP imaging even at the shortest TRs attainable given hardware and safety limitations. Furthermore, catalyzation of the steady-state does not work as well at certain bands of frequency in the off-resonance spectrum. When a single SSFP acquisition is performed at a low TR, low SNR images that have both significant banding artifact and artifact from transient signal oscillations are often obtained. By repeating the acquisition N times with the phase of the RF pulse cycled appropriately from excitation to excitation (as described in [21, 22, 25]), the position of the banding artifact (and hence the position of the source of the transient oscillation artifact) can be shifted. Combination of several of these RF phase-cycled acquisitions produces high SNR images with flat spectral responses, reducing banding artifacts. Multiple-acquisition techniques are also effective at muting any transient signal oscillation artifact.

As described in Chapter 4, there are several multiple-acquisition combination techniques to choose from, varying only in the manner in which the final component

images are combined. Maximum-intensity [22] and complex-sum combination [25] have very flat responses to off-resonance variations, even when combining only two or three acquisitions, and are thus highly effective at removing off-resonance banding. However, higher SNR can be obtained from the same set of acquisitions using a sum-of-squares combination [39]. The sum-of-squares spectral response will not generally be as flat as the other methods, but resultant SNR is significantly higher. In practice, the sum-of-squares technique is adequate when at least four acquisitions are combined.

5.3   Methods

The fluid-attenuated SSFP sequence was implemented on a GE 1.5 T Signa scanner with CV/i gradients. To make use of the large inversion-recovery null time of CSF (approximately 2.5 s), the sequence interleaves slices, pre-inverting as many slices as possible. The timing and interleaving is optimally calculated by the sequence based on the imaging time per slice and the TI employed. All needed phase encodes are acquired during a single inversion of each slice. No dummy acquisitions are employed after the catalyzing $\alpha/2$ pulse. At a TR of 3.6 ms and 192 phase encodes, a single slice is imaged in approximately 700 ms. Excellent scan time utilization is achieved by employing a TI of about 2.3 s and inverting three slices ahead of the slice readouts. The sequence uses a slice-selective Shinnar-Le Roux inversion pulse [40], with the inverted slice thickness set to three times the slice width to ensure good inversion across the slice.

TRs of both 3.6 and 4.5 ms were successfully employed. The actual readout times were 1 ms and 2 ms for the 3.6 and 4.5 ms TR scans respectively. Operating at a TR of 3.6 ms clearly yields a faster overall scan time than operating at a TR of 4.5 ms. However, the SNR of the TR = 4.5 ms scan is expected to improve by a factor of $\sqrt{2}$ over the TR = 3.6 ms scan, since readout time is doubled from 1 ms to 2 ms. The SNR efficiency of the TR = 4.5 ms scan will be significantly better, as this $\sqrt{2}$ improvement in SNR accompanies an increase in total scan time of only 25%. Note that combination of multiple acquisitions makes the choice of TR flexible.
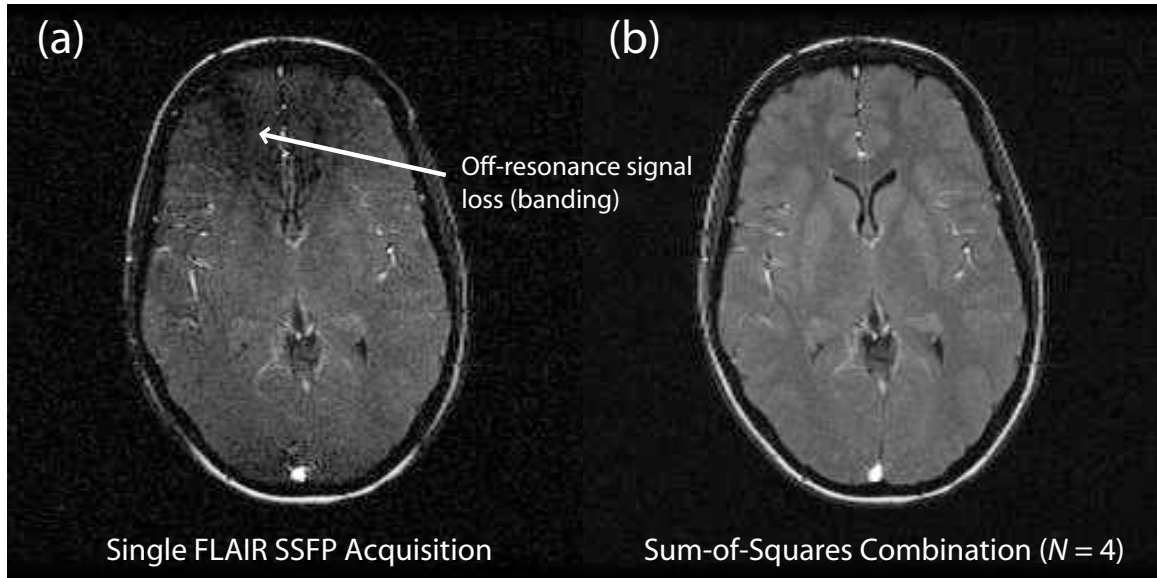
Figure 5.5: (a) Axial brain image formed from a single FLAIR SSFP acquisition. Note the low SNR and characteristic off-resonance banding artifact. (b) The same slice imaged using sum-of-squares combination of four phase-cycled FLAIR SSFP acquisitions. The SNR is boosted, yielding useful contrast, and the off-resonance banding artifact is eliminated. Sequence parameters for both scans were: TR = 4.5 ms, $\alpha = 60°$, TI = 2.25 s, FOV = 24 cm, 256×192 matrix, 5 mm slice thickness.

In practice, performing single 2D acquisitions at short TR (less than 5 ms) yielded inadequate SNR in the brain. In addition to the expected banding and transient artifact, these images contained very little useful contrast given the low SNR and presence of artifacts. An example of a single acquisition is shown in Figure 5.5(a). Combining multiple acquisitions proved to be essential to produce diagnostically useful brain images. The multiple-acquisition techniques were found to be very effective at producing high SNR images with very little artifact, and at bringing out the contrast expected based on signal simulations. Due to the extremely fast scan times of SSFP, the needed acquisitions can be performed while still achieving very low overall scan time.

Figure 5.5(b) shows a sum-of-squares combination of four acquisitions. The sum-of-squares technique adequately removed banding artifacts from the short TR images

when at least four acquisitions were combined. This, and higher SNR, led to its adoption as the method of choice.

A typical full-brain axial FLAIR study acquires twenty 5 mm slices over a 24 cm field of view, with 1.5 or 2.5 mm interslice spacing. With these scan parameters and a TR of 4.5 ms (2 ms readout), a 256×192 matrix, and combination of four acquisitions ($N = 4$), the scan time of the FLAIR SSFP sequence is 1 m 40 s. At a TR of 3.6 ms (1 ms readout) and combination of eight acquisitions ($N = 8$), the scan time is 2 m 18 s. A fast spin-echo FLAIR sequence achieving the same coverage and comparable SNR requires approximately 4 minutes.

5.4   Results and Discussion

Figure 5.6 shows two slices from a series of axial brain images of a normal volunteer for (a) FLAIR fast spin-echo, (b) FLAIR SSFP with $\alpha = 30°$, and (c) FLAIR SSFP with the flip angle increased to 60°. The scan parameters are shown in the figure caption. The FLAIR SSFP images achieve excellent CSF suppression and similar gray-matter SNR to the FSE images in less than half the scan time. While contrast between gray and white matter is not as high in the SSFP images as in the T_2-weighted FSE images, FLAIR SSFP exhibits improved T_2 contrast as the flip angle is increased. FLAIR SSFP has the potential to provide similar contrast and SNR to FLAIR FSE in a shorter scan time. This may allow for higher resolution scans with signal averaging, or 3D imaging. Either may be helpful in diagnosis of periventricular white matter and peripheral subcortical lesions.

Figure 5.7 shows an axial image from a patient with multiple sclerosis (MS). Imaging parameters were FOV = 24 cm, 256×192 matrix, 20 slices, 5 mm slice thickness, 2.5 mm inter-slice gap, TR/TE = 3.6/1.5 ms, flip angle = 30°, TI = 2.25 s, and 2 m 18 s total scan time. Multiple periventricular white matter plaques are seen (arrows) which have high signal intensity rims and low signal intensity central regions. To increase the contrast of these lesions to the underlying white matter, the flip angle could be increased.
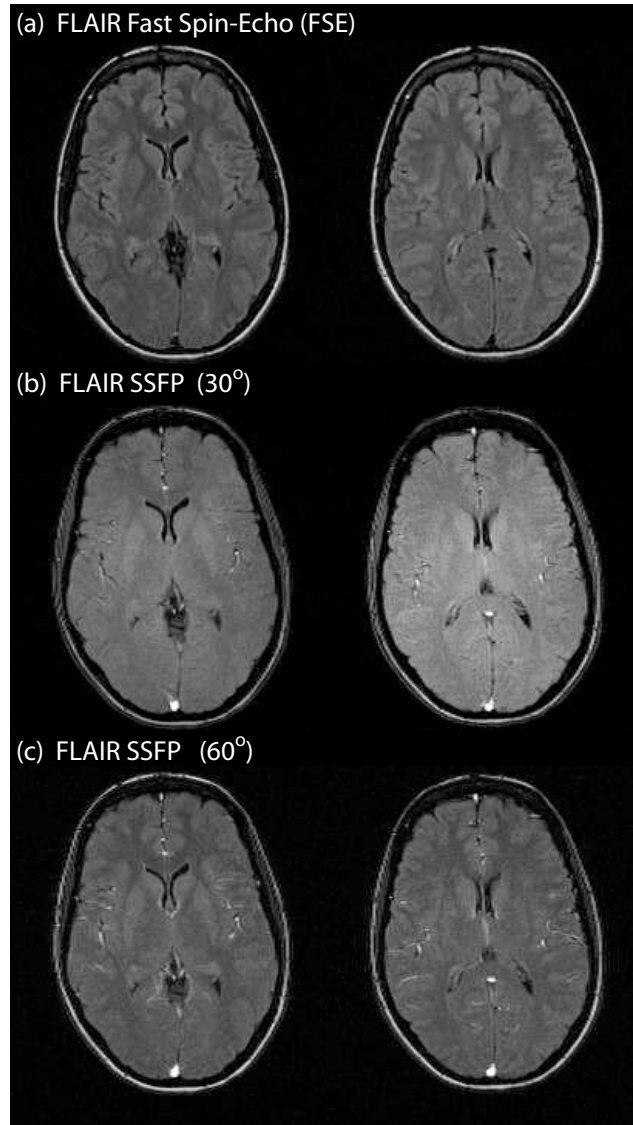
Figure 5.6: (a) Axial 2D FLAIR fast spin-echo (FSE) images of normal human brain (TR/TE = 9000/120 ms, TI = 2200 ms, FOV = 24 cm, 256×192 matrix, 5 mm slice thickness, 20 slices acquired in 4 m 12 s). (b) Corresponding axial FLAIR SSFP images at $\alpha = 30°$ (TR/TE = 4.5/2.4 ms, TI = 2250 ms, FOV = 24 cm, 256×192 matrix, 5 mm slice thickness, 20 slices acquired in 1 m 40 s). (c) FLAIR SSFP at $\alpha = 60°$, other parameters same as (b). FLAIR SSFP images achieve similar gray-matter SNR to FLAIR FSE in less than half the scan time, although gray/white contrast is lower in the SSFP sequences. However, the expected improvement in gray/white contrast is seen with increased flip angle in FLAIR SSFP.

Figure 5.7: FLAIR SSFP images of volunteer with multiple sclerosis. Multiple periventricular white matter plaques are seen (several marked with arrows). The scan employed FOV = 24 cm, 20 slices, 256×192 matrix, 5 mm slice thickness, 2.5 mm inter-slice spacing, TR/TE = 3.6/1.5 ms, flip angle = 30°, TI = 2.25 s, and 2 m 18 s total scan time. MS plaque conspicuity could likely be increased by increasing the flip angle beyond the 30° used.

As discussed in the *Signal and Contrast* subsection, the contrast of FLAIR SSFP as implemented varies mainly with T_2/T_1, although the contrast is somewhat altered from that of steady-state SSFP due to the presence of the inversion pulse and image acquisition during the transient. This can reduce lesion contrast relative to that in a T_2-weighted image when elevations in lesion T_2 are accompanied by elevations in T_1. A heightened degree of T_2 contrast could potentially be achieved with FLAIR SSFP by the insertion of a T_2-preparation pulse [41] following the inversion delay TI, prior to the catalyzing $\alpha/2$ pulse. A centric phase-encode ordering could capture the heightened T_2 contrast during the excitations immediately following the preparation pulse.

Further future work could include the extension of the sequence to 3D. In order to achieve scan time efficiency, a 3D multi-slab approach could be adopted, in which slabs are interleaved and pre-inverted in a way analogous to the 2D multi-slice technique. If needed, reductions in TI could be achieved by using an inversion pulse of less than 180°, reducing the time needed for the CSF signal to null.

5.5   Conclusion

IR-prepared SSFP can be combined with a sum-of-squares combination of phase-cycled SSFP acquisitions to achieve excellent fluid suppression and higher SNR efficiency than typical fast spin-echo FLAIR. This chapter has presented a fast 2D multi-slice implementation of the FLAIR SSFP sequence, which achieves similar gray-matter SNR to a corresponding FLAIR FSE sequence in less than half the scan time.

Axial FLAIR SSFP brain scans on a normal volunteer demonstrate excellent CSF suppression, and very good visualization of brain parenchyma. The contrast exhibited is a slight modification of typical T_2/T_1 SSFP contrast, with the degree of T_2/T_1 discrimination enhanced with increasing flip angle. Axial scans of a patient with multiple sclerosis show clearly visible plaques.

While the sequence demonstrates the feasibility of very fast fluid-suppressed neuroimaging using SSFP, further work is needed to gauge the utility of the resultant contrast in the detection and evaluation of pathology.

Chapter 6

3D Flow-Independent Peripheral Angiography with SSFP

6.1 Introduction

Interest in performing MR angiograms of the peripheral vasculature has increased as surgical bypass procedures have become more common in the infrapopliteal and pedal arteries. While x-ray angiography can provide excellent information for surgical planning in the peripheral vasculature, it is an invasive procedure that can fail to depict clinically significant run-off vessels [42]. Imaging of peripheral vascular structure necessitates high spatial resolution given the small arterial diameters in the extremities. Contrast-enhanced MRA techniques, which capture contrast during the relatively short window of time between arterial and venous enhancement, are limited in the spatial resolution they can achieve.

Flow-independent angiography (FIA) techniques have been shown to be effective at producing high-resolution peripheral angiograms [42–45]. These techniques exploit the inherent differences in tissue T_1, T_2, and chemical shift to generate contrast, rather than relying on parameter changes induced by contrast agents. Various magnetization-preparation techniques are applied to generate the desired contrast.

FIA without contrast enhancement is therefore not limited in spatial resolution by the short period of time between arterial and venous contrast enhancement.

Recent work has shown that the high SNR, short scan times, and flow properties of balanced steady-state free precession (SSFP, True FISP, or FIESTA) make it an excellent candidate for flow-independent angiography [4, 45]. However, the characteristic bright long-T_1 fluid signal of balanced SSFP can obscure vascular structures when long-T_1 fluids, such as edema or synovial fluid, are present in the region of interest. Balanced SSFP angiograms of the pedal arteries, for example, suffer from bright synovial fluid signal between the bones of the foot. Angiograms of the lower leg or extremities in patients with peripheral swelling may be obscured by bright signal from edema.

In this chapter, a fast, magnetization-prepared 3D SSFP sequence for creating high-resolution flow-independent angiograms with long-T_1 fluid suppression is presented. The sequence exploits inversion-recovery/T_2-prep combined with square-spiral centric phase encode ordering for contrast generation. Fat suppression is achieved through phase-sensitive SSFP reconstruction [4]. Scan parameters are optimized to achieve good fluid suppression and high arterial/muscle and arterial/venous contrast, at only a modest scan time penalty over simple 3D SSFP. Results are presented in the lower leg and foot.

6.2   Methods

6.2.1   Pulse Sequence

A diagram of the sequence is shown in Figure 6.1. A non-selective 180_x° inversion pulse is followed by a large gradient spoiler to dephase any residual transverse magnetization. An inversion delay of length TI follows, chosen to attenuate long-T_1 fluids. A TI of approximately 2 s returns both blood ($T_1 \approx 1$ s) and muscle ($T_1 \approx 850$ ms) to near-equilibrium values.
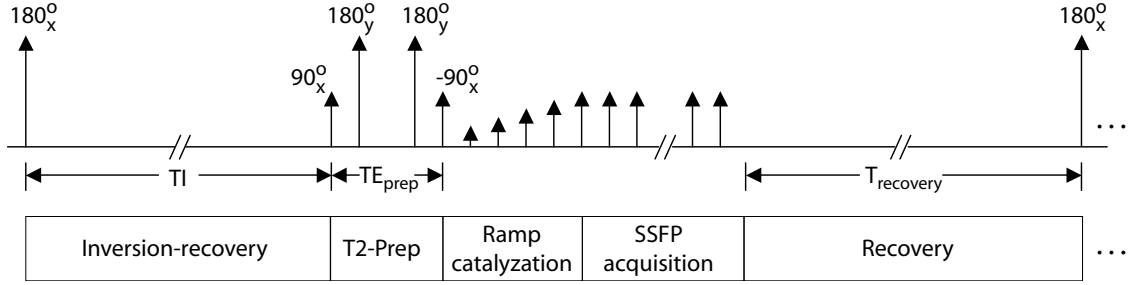
Figure 6.1: A spoiled non-selective inversion is followed by an inversion time TI, after which a T_2-preparation sequence is applied. Immediately following the T_2 preparation, a linear ramp catalyzation is performed to reduce transient signal oscillations. SSFP acquisition then begins, with a centric phase-encode ordering. The whole sequence is then repeated for the desired number of interleaves.

At the end of the inversion delay, a T_2-preparation sequence is played to suppress muscle signal and enhance arterial/muscle and arterial/venous contrast [41]. A centric phase-encode ordering in SSFP results in image contrast exhibiting more proton-density weighting than the steady-state T_2/T_1 contrast typical of SSFP [10]. Use of a T_2-preparation sequence generates the higher T_2 discrimination needed for flow-independent angiography. The sequence presented here employs a simple $90^\circ_x, 180^\circ_y, 180^\circ_y, -90^\circ_x$ preparation, with the echo time TE_{prep} measured between the isocenters of the first pulse (90°_x tip down) and final pulse (-90°_x tip up). The two 180°_y pulses are centered at delays of $TE_{prep}/4$ and $3TE_{prep}/4$ respectively after the initial tip down. All pulses are non-selective. The final tip-up pulse is immediately followed by a gradient spoiler to dephase residual transverse magnetization.

A linear ramp catalyzation is performed to reduce transient oscillations immediately prior to SSFP data acquisition [8]. Square-spiral phase encode ordering is used to capture the prepared contrast at low spatial frequencies [46]. The square-spiral ordering was chosen for ease of implementation; an elliptical centric ordering [47] may also be used, but should not yield significantly different results when the FOV in each of the two phase-encode directions is similar.
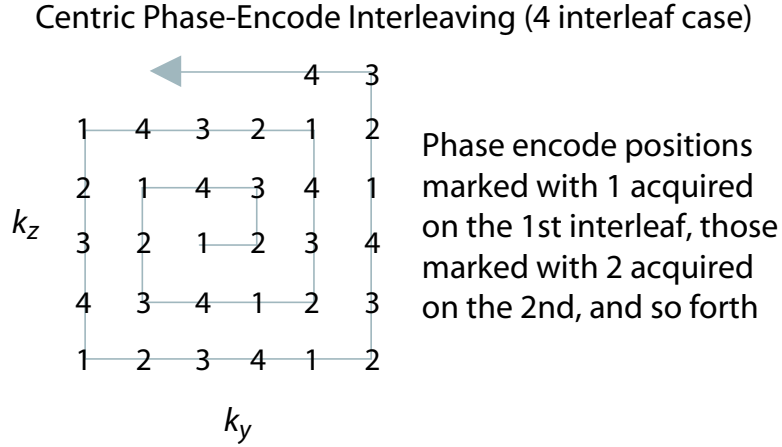
Centric Phase-Encode Interleaving (4 interleaf case)

k_z

k_y

Phase encode positions marked with 1 acquired on the 1st interleaf, those marked with 2 acquired on the 2nd, and so forth

Figure 6.2: If more than one magnetization preparation is required to achieve good fluid suppression or T_2 contrast, the square-spiral phase encodes are interleaved (as shown for the four interleaf case above).

The above series (IR, T_2-prep, catalyzation, balanced SSFP acquisition) may need to be repeated several times during acquisition of the volume of interest, as the magnetization-prepared signal levels evolve to the steady-state. In particular, high spatial frequency artifact from long-T_1 fluids is more severe as the total number of magnetization-preparation steps is decreased. When multiple repetitions are used, the sequence interleaves the square-spiral phase encodes as shown in Figure 6.2. This effectively increases the extent of k-space acquired before signal levels evolve from their magnetization-prepared state to the steady state, decreasing high spatial frequency artifact. A recovery time of at least several seconds is required between each set of acquisitions to allow the volume to reach near equilibrium prior to the subsequent inversion. Thus, increasing the number of interleaves carries a concomitant penalty in scan time.

6.2.2   Postprocessing

Phase-sensitive fat detection, as described in Chapter 3, is used in the angiography sequence presented here to null fat pixels. However, to be effective, off-resonance
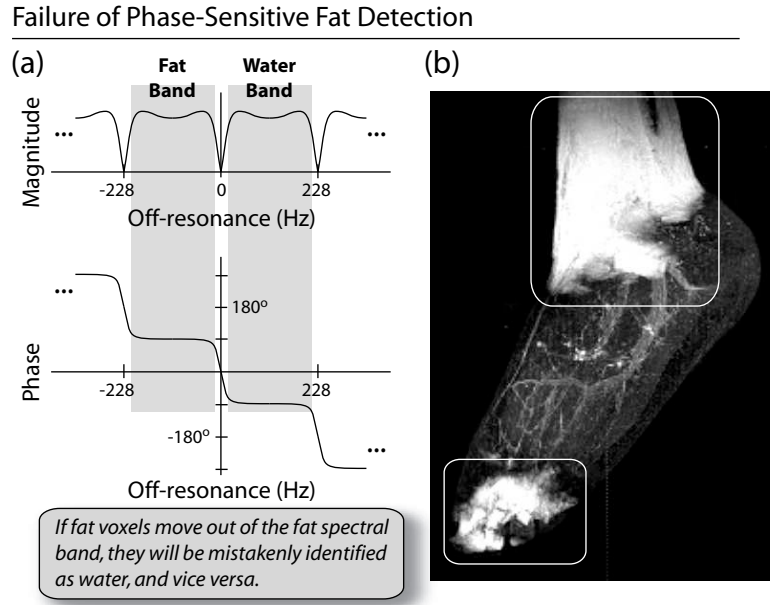
Figure 6.3: Off-resonance variations across an image need to be limited to the passbands shown in (a) above for phase-sensitive fat detection to properly identify fat voxels. If off-resonance is severe enough, fat detection fails, yielding images such as the maximum-intensity projection (MIP) image shown in (b).

variations must be limited to the passbands shown in Figure 6.3(a). Otherwise fat pixels may drift into the water passband, and have phase indistinguishable from water pixels. This is a particular problem in the foot, where irregular geometry leads to large susceptibility-induced field variations. While at times the shim can be adequate, it often is not, leading to images such as that shown in Figure 6.3(b).

Once again phase-cycled SSFP can lend a hand. The complex sum of two phase-cycled SSFP acquisitions, one with $\Delta\phi = 0°$ and one with $\Delta\phi = 180°$, has the almost linear phase profile shown in Figure 6.4(a). For TR = 4.4 ms, fat and water pixels at *any* off-resonance value will be 180° out of phase. If a water or fat pixel is manually identified in the reconstructed complex-sum data set, a region-growing phase-detection algorithm can be used to correct off-resonance phase variations. The problem of fat pixels migrating into the water passband (or vice versa) is solved because near-neighbor fat and water pixels always exhibit the 180° relative phase
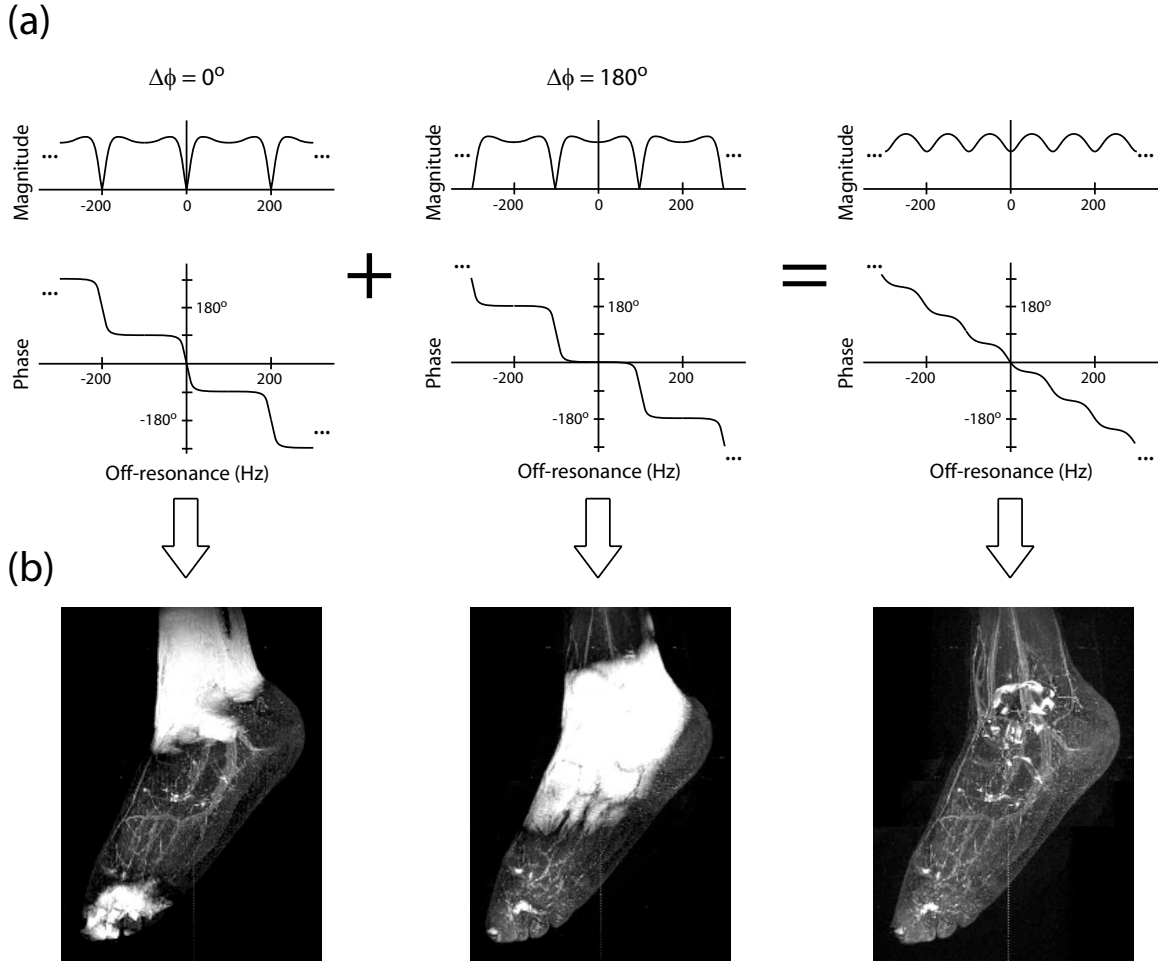
Figure 6.4: The complex sum of two phase-cycled SSFP acquisitions, one with $\Delta\phi = 0°$ and one with $\Delta\phi = 180°$, has an almost linear phase profile, as shown in (a). Provided spatial field variations are not too rapid, near-neighbor fat and water pixels will always be approximately $180°$ out of phase. This allows more robust phase-sensitive fat detection in the presence of off-resonance, as demonstrated in (b).

shift. Figure 6.4(b) illustrates the correction of the image in Figure 6.3(b) using complex-sum phase-detection[1].

6.2.3 Parameter Optimization

Bloch simulations of the SSFP signal evolution are shown in Figure 6.5 for a variety of cases. In (a) the signal evolution with a simple catalyzation but no magnetization-preparation is shown. The addition of inversion-recovery prior to SSFP excitations yields the signal evolution shown in (b). Signal progression after a T_2-preparation pulse (with no inversion-recovery) is shown in (c), while the combination of inversion-recovery and T_2-prep yields (d). T1 and T2 values assumed in the simulation are shown in the table adjacent to Figure 6.5.

From these graphs it is clear that the signal evolves during the course of image acquisition. The dominant contrast, however, will be given by the signal levels when the center of k-space is sampled. The sequence under consideration (catalyzed IR/T_2-prep SSFP) makes use of a centric phase-encode ordering, as mentioned above. Contrast is therefore roughly defined by the initial signal values in the graph shown in Figure 6.5(d). Variations in inversion time TI, T_2-prep echo time TE_{prep}, and flip angle α all affect the initial signal values. Examples are shown at several combinations of α and TE_{prep} in Figure 6.6. These simulations assumed TR/TE = 4.6/2.3 ms, and TI = 2.4 s.

By examining the arterial/muscle and arterial/venous contrast as a function of these parameters (TI, TE_{prep}, and α), more optimal sequence parameter combinations can be discovered. Bloch simulations were performed to ascertain the initial contrast-defining signal levels for various combinations of TI, TE_{prep}, and α. The results are shown in Figure 6.7. Note that higher flip angles tend to yield better contrast, with optimal TE_{prep} values lying between about 60 and 120 ms. Simulations were performed at TR/TE = 4.6/2.3 ms.

---

[1]The author acknowledges the work of Brian Hargreaves in proposing the complex-sum phase-sensitive fat detection approach described above. However, no published work currently exists to appropriately cite.

(a) Catalyzed SSFP signal

(b) Catalyzed SSFP with inversion-recovery (IR)

(c) Catalyzed SSFP with T2-Prep

(d) Catalyzed SSFP with IR and T2-Prep

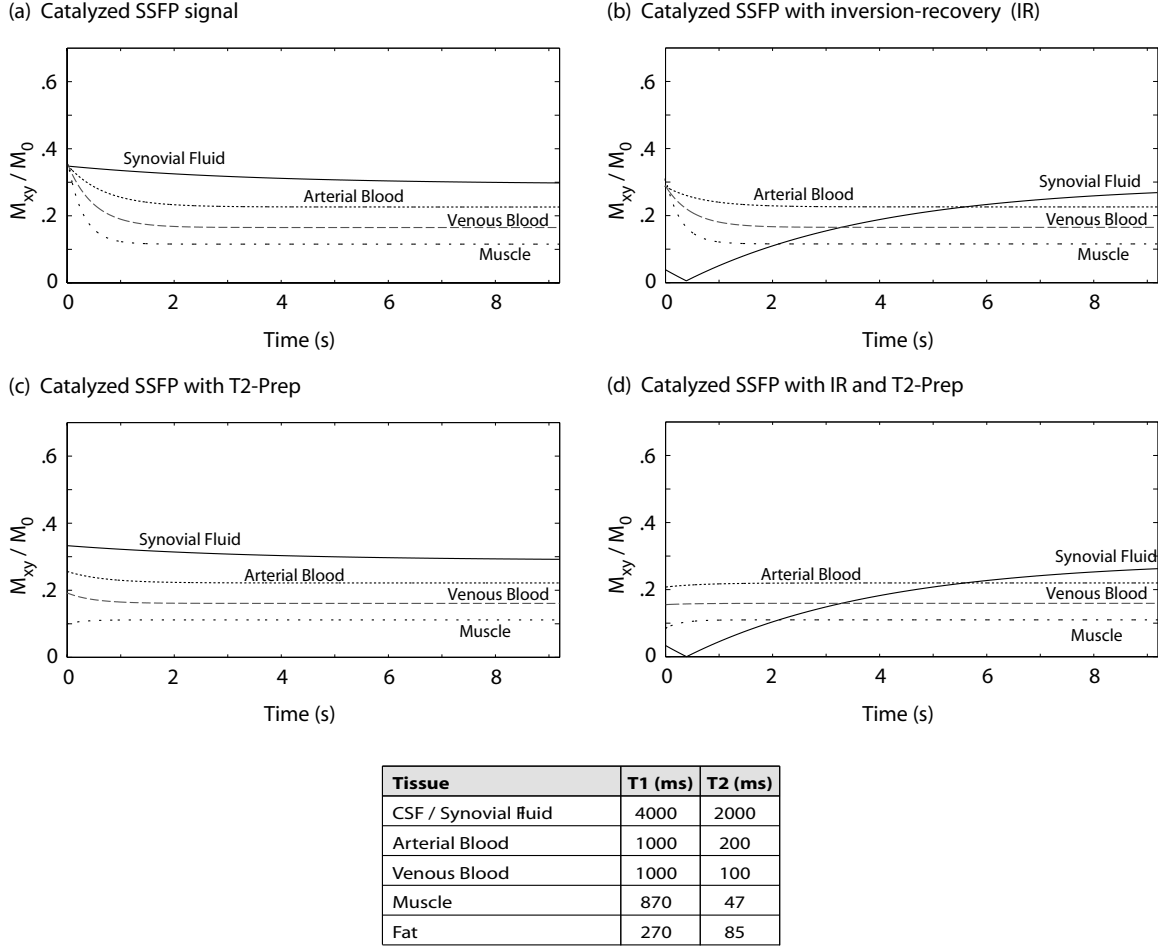| Tissue	T1 (ms)	T2 (ms)
CSF / Synovial fluid	4000	2000
Arterial Blood	1000	200
Venous Blood	1000	100
Muscle	870	47
Fat	270	85

Figure 6.5: (a) Bloch simulation of SSFP signal evolution with a catalyzation sequence but no magnetization-preparation. (b) Signal evolution with the addition of an IR pulse prior to catalyzation and SSFP excitations, (c) same with a T_2 preparation pulse rather than an IR pulse, and (d) signal evolution with a combined IR/T_2-prep pulse.

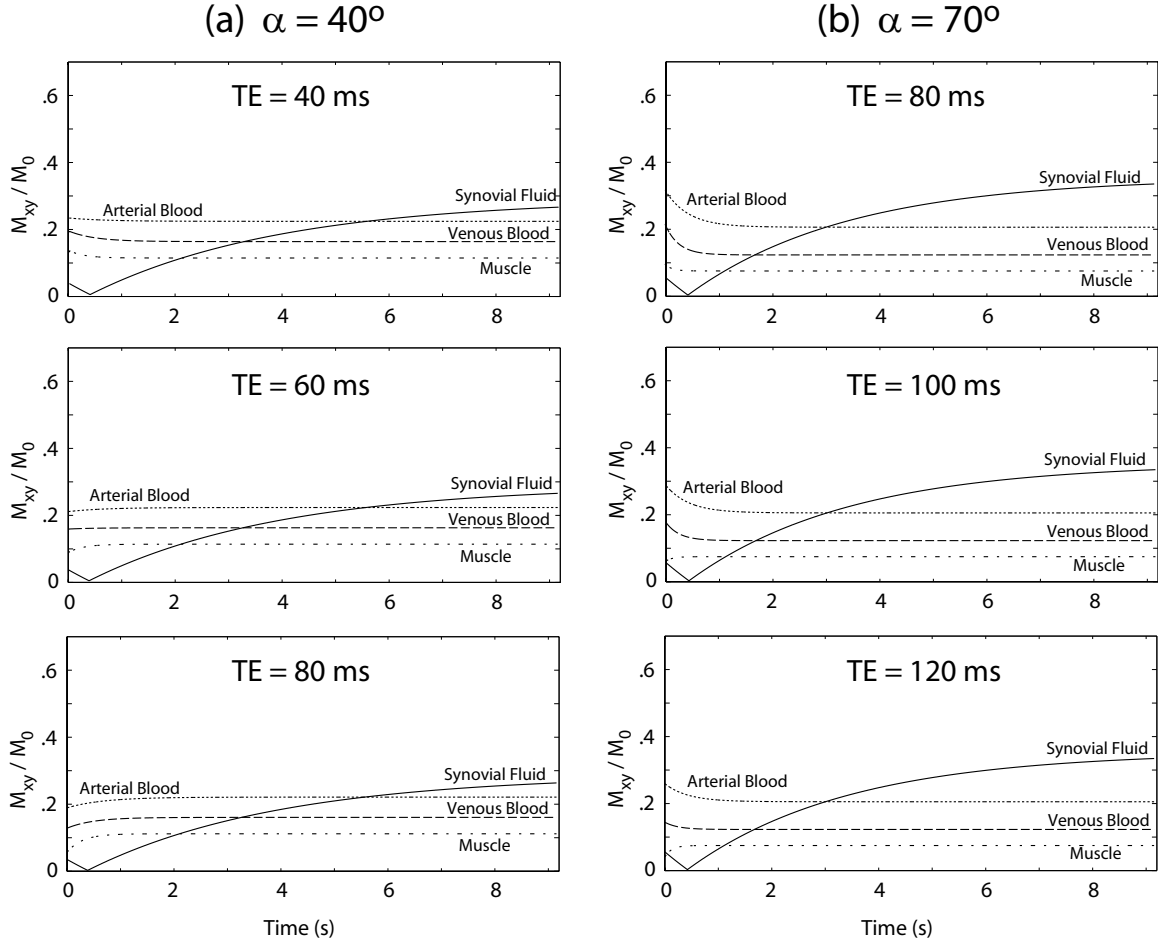Figure 6.6: IR/T_2-prep SSFP signal evolutions are shown in (a) for a 40° flip angle at various T_2-prep echo times, and in (b) for a 70° flip angle. A square spiral centric phase-encode ordering is used, so the dominant contrast is given by the initial signal levels shown in each graph. At larger flip angles, a longer T_2-prep echo time is required for good muscle suppression and arterial/venous contrast.
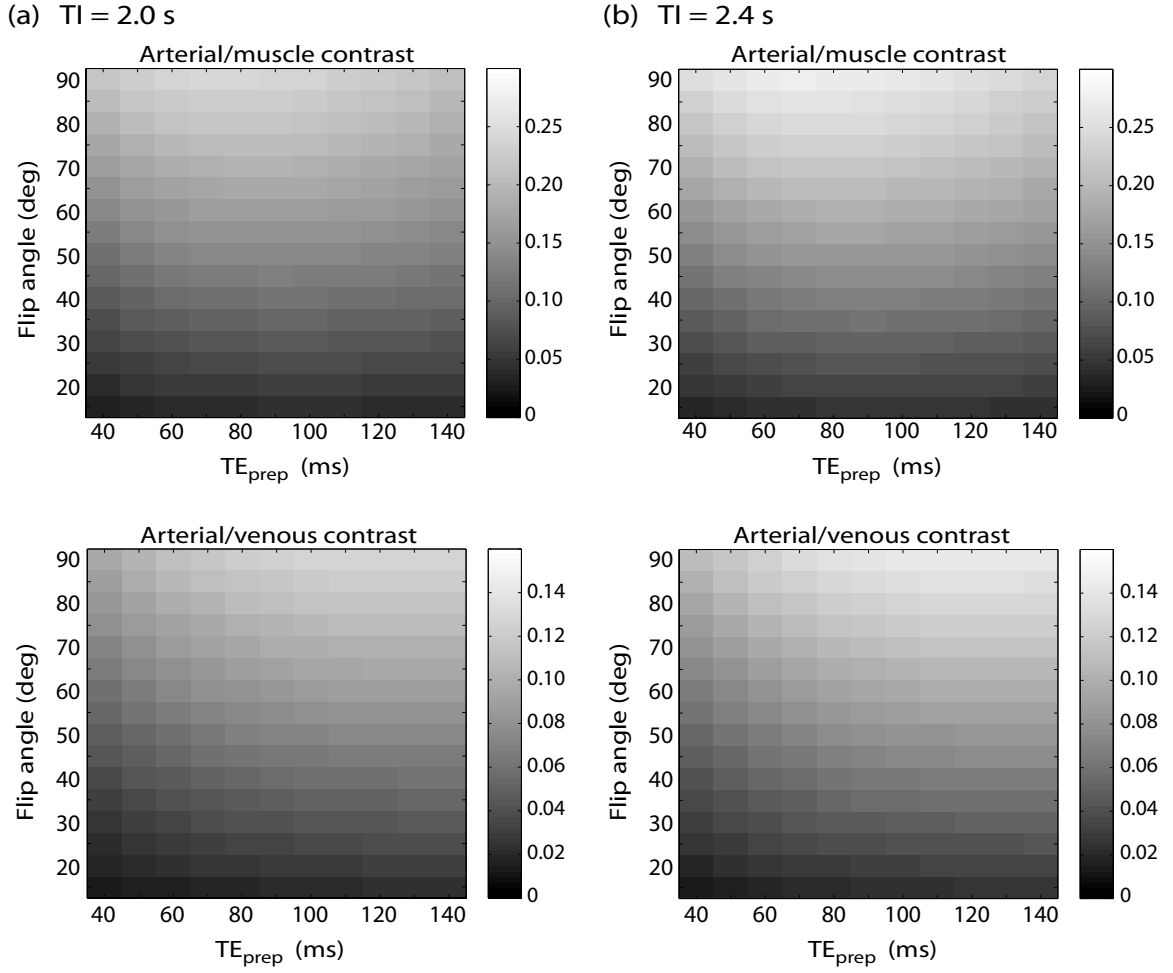
Figure 6.7: The contrast achieved in IR/T_2-prep SSFP is a function of the inversion time TI, the T_2-prep echo time TE_{prep}, and the flip angle α. In (a), arterial/muscle and arterial/venous signal difference are plotted as a function of TE_{prep} and α at TI = 2.0 s. In (b), corresponding graphs are shown for TI = 2.4 s. Simulations assumed TR/TE = 4.6/2.3 ms.

6.3 Results

The sequence was implemented on a 1.5 T GE scanner with CV/i gradients. A protocol suitable for the lower leg and foot was prescribed with the following scan parameters: TR/TE = 4.6/2.3 ms, $\alpha = 70°$, $384 \times 128 \times 128$ matrix, 1 mm isotropic resolution, TI = 2 s, $TE_{prep} = 80$ ms, and a 10 excitation linear ramp catalyzation. Four interleaves were performed (i.e., four magnetization preparations were applied over the course of the scan). Total scan time for the protocol was 1:55 (including a long $T_{recovery}$ of 10 s to avoid gradient overheating), compared with a normal balanced SSFP scan time with the same parameters of 1:15.

Figure 6.8 shows results in a normal foot. The image on the left (Figure 6.8(a)) was acquired with only the T_2-prep pulse, eliminating

the inversion-recovery section. Bright synovial fluid signal is seen in the joints of the foot, obscuring vascular structure. Figure 6.8(b) shows the corresponding result when both the inversion-recovery and T_2-prep were applied. Synovial fluid signal is well suppressed, allowing much better visualization of the vessels. High arterial/venous contrast is also achieved. Note that the shim was adequate in this case for single-acquisition phase-sensitive fat detection to be effective.

Figure 6.9 shows the IR/T_2-prep sequence applied in the lower leg, with the same parameters as in Figure 6.8(b). The popliteal trifurcation is clearly visualized, although no edema is present in this normal volunteer to hamper visualization. Again, the shim was adequate to necessitate only a single acquisition for adequate fat suppression.

Figure 6.10 demonstrates the use of complex-sum phase-sensitive fat detection. The complex data from two normal 3D SSFP acquisitions, one without phase cycling and one with $\Delta\phi = 180°$, were summed. Phase-sensitive fat detection was then performed, yielding excellent fat suppression. The scan achieves 0.8 mm isotropic resolution on a $384 \times 160 \times 160$ matrix, in a total scan time of 1:58, with TR/TE = 4.6/2.3 ms and $\alpha = 70°$. The corresponding scans using both T_2-prep and IR/T_2-prep were also performed. These made use of six square-spiral interleaves, with a 10 s delay
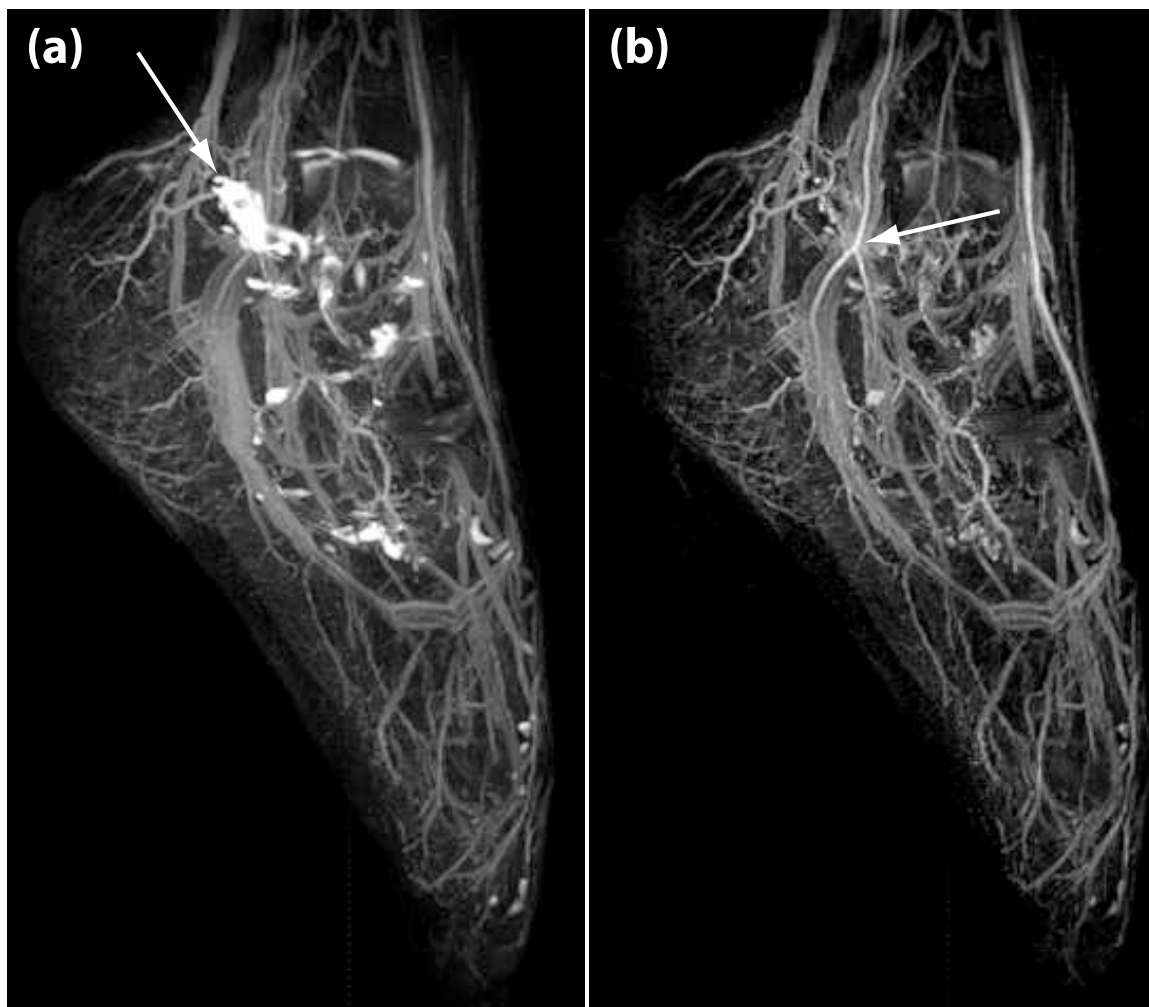
Figure 6.8: Maximum-intensity projection of 3D T_2-Prep balanced SSFP flow-independent angiograms of the foot at 1.5 T. Phase-sensitive SSFP reconstruction was used for fat suppression. (a) Angiogram without the IR preparation (T_2-prep only), showing high signal from synovial fluid in the foot joints (arrow). (b) IR and T_2-prep angiogram, showing good synovial fluid suppression and high arterial/venous contrast (arrow). Both sequences employed four interleaves and achieve 1 mm isotropic resolution on a $384 \times 128 \times 128$ matrix. Scan times were 1:47 for (a) and 1:55 for (b).

Figure 6.9: Popliteal trifurcation (cropped to show detail) in a normal using IR/T_2-prep SSFP with four square spiral interleaves. TR/TE = 4.6/2.3 ms, TI = 2 s, $\alpha = 70°$, TE$_{prep}$ = 80 ms, 1 mm isotropic resolution, and total scan time 1:55.

Figure 6.10: Maximum-intensity projection of a high resolution balanced SSFP flow-independent angiogram of the foot at 1.5 T. Complex-sum phase-sensitive SSFP reconstruction was used for fat suppression. Two simple SSFP acquisition were employed (no IR or T_2-prep), one without phase cycling and one with a phase increment of 180° from excitation to excitation. Excellent fat suppression and vessel visualization is achieved, at 0.8 mm isotropic resolution on a $384 \times 160 \times 160$ matrix. Total scan time was 1:58.

between each interleaf. While achieving good vessel contrast, a significant degradation in SNR was observed in the magnetization-prepared scans when compared with the SSFP scan shown. Further investigation and scan parameter optimization at these higher resolutions is warranted.

6.4   Conclusion

Balanced SSFP sequences show promise for rapid 3D flow-independent angiography of the peripheral vasculature. High-resolution volumetric scans can be achieved in under two minutes, with phase-sensitive fat detection suppressing fat signal. In regions with significant off-resonance, complex-sum phase-sensitive fat detection has been demonstrated to be effective at eliminating signal from fat voxels.

In the presence of long-T_1 fluids, a combination IR/T_2-prep 3D balanced SSFP sequence with square-spiral centric phase encode ordering can be combined with phase-sensitive fat suppression to produce high-resolution flow-independent angiograms. Good long-T_1 suppression can be achieved with as few as four magnetization preparations for the entire 3D volume, only modestly increasing the scan time over a simple 3D balanced SSFP acquisition.

Chapter 7

Summary and Recommendations

7.1 Summary

The focus of the work presented in this dissertation is the development of balanced steady-state free precession (SSFP) MRI techniques with reduced artifact and enhanced contrast for various applications. Specifically, a statistical analysis framework for studying banding artifact reduction techniques in SSFP has been presented and applied, and a more SNR efficient method proposed and analyzed. Two new magnetization prepared sequences have been presented, one for CSF-suppressed neuroimaging and the other for peripheral angiography.

A summary of the major contributions follows:

- Development of a statistical analysis framework for evaluating the SNR efficiency, contrast, and banding artifact reduction of multiple-acquisition techniques. Analysis of maximum-intensity SSFP, complex-sum SSFP, and the new sum-of-squares technique (below) using the statistical framework.

- Proposal of a new sum-of-squares technique for eliminating SSFP banding artifact. Analysis shows the sum-of-squares technique yields significantly higher

SNR efficiency than either maximum-intensity SSFP or complex-sum SSFP, while robustly removing banding artifacts.

- Development of a fast 2D magnetization-prepared SSFP technique for CSF-suppressed neurological imaging. The technique exhibits comparable SNR images to corresponding CSF-suppressed fast spin-echo images requiring nearly twice the scan time. Tests in normals exhibited good gray/white matter contrast, and a test in a patient with multiple sclerosis showed reasonable lesion conspicuity.

- Development of a fast 3D magnetization-prepared SSFP sequence for peripheral angiography. The sequence suppresses edema and synovial fluid using inversion-recovery, and generates enhanced arterial/venous suppression and muscle suppression with a T2-preparation sequence. The sequence was successfully applied in the lower leg and foot, yielding rapid high-resolution volumetric scans with excellent vascular visualization.

- Demonstration of the feasibility of oscillating-equilibrium SSFP sequence synthesis using complex optimization techniques and normal desktop hardware (Appendix A).

7.2 Recommendations

7.2.1 Multiple-Acquisition SSFP

Each of the multiple-acquisition SSFP techniques discussed in this dissertation requires the complete acquisition of $N \geq 2$ images. The combination of these acquisitions to form the final image is very sensitive to misregistration arising from motion. In long scans, or in regions where motion is expected (e.g., the chest or abdomen), image misregistration between acquisitions can be a serious problem.

One way of potentially reducing this sensitivity to motion is to temporally localize the acquisition of the center of k-space for each of the component images. [48] presents

a method for the $N = 2$ case. The phase-encode order is an elliptical-centric spiral inward on the first acquisition, followed by a spiral outward for the second acquisition. This allows the center of k-space of the second acquisition to be acquired immediately after the center of k-space for the first image.

Other methods of interleaving the acquisitions to temporally localize the centers of k-space may be possible, and merit exploration. Catalyzation into and out of the steady state may enable more efficient interleaving. The possibility of creating oscillating-equilibrium sequences (Appendix A), where the N equilibrium spectra yield images that can be combined to eliminate banding artifact, is particularly intriguing. The N component acquisitions would then be performed in parallel—a near best-case scenario for limiting sensitivity to motion.

Another area that deserves exploration is the development of more optimal combination schemes, from an SNR efficiency perspective, than sum-of-squares. The sum-of-squares technique only makes optimal use of the information acquired if each of the N observations for a given pixel is independent of the others. As discussed, this is not the case. While more complex combination schemes may yield such small gains in SNR that they are not worth the additional complexity, they are nonetheless worthy of further consideration.

Lastly, many current uses of SSFP could benefit from their combination with the sum-of-squares technique. These include both high-field and high-resolution imaging.

7.2.2   2D Fluid-Attenuated Inversion Recovery SSFP

The fluid-attenuated inversion recovery SSFP sequence presented in this dissertation, while achieving rapid scan times and good contrast, does not appear to achieve the same degree of elevated-T_2 lesion conspicuity and gray/white matter contrast as fast spin-echo sequences. Part of this may be due to the non-optimal scan parameters used for the multiple sclerosis patient. A tip angle of 30° was used, while optimizations performed later indicated that higher tip angles would yield better contrast. Trials at higher tip angles should be performed. Further methods of enhancing contrast,

such as through the use of other magnetization-preparation sequences, ought also to be explored.

7.2.3   3D Flow-Independent Angiography with SSFP

The application of rapid magnetization-prepared 3D SSFP techniques to peripheral angiography is still largely unexplored. Fluid-suppression has been demonstrated on synovial fluid in the bones of the foot. However, further clinical tests are imperative to gauge its efficacy on patients with peripheral edema and other pathology.

Likewise, the combination of a T_2-preparation sequence with centric 3D SSFP acquisition has been shown effective at enhancing arterial/venous contrast and suppressing muscle signal. However, a more thorough optimization could help determine optimal T_2-prep echo times, particularly when the T_2-prep is combined with inversion-recovery for fluid suppression.

Application of the 3D fluid-suppressed SSFP sequence at 3 Tesla (and higher fields) should yield higher SNR and better contrast. At higher fields, alternate methods for suppressing fat will be needed, as the phase-sensitive method is not practical beyond 1.5 Tesla when considerable field inhomogeneity is expected. Application of the sequence at both higher fields and higher resolutions is recommended.

Appendix A

Sequence Synthesis using Complex Optimization

A.1 Introduction

Refocused SSFP sequences typically utilize the same flip angle from excitation to excitation, with a possible linear increment in the flip phase to shift the off-resonance profile (Chapter 3). Several sequences have been proposed that make use of periodic variations in the flip angle and phase, resulting in an oscillating steady state [11, 15]. As noted at the end of Chapter 3, an effective method was proposed in [16] to synthesize oscillating-equilibrium sequences with a desired magnetization profile using the Shinnar-Le Roux (SLR) transform. This approach is very fast, and avoids the computational difficulty of the general optimization problem.

In this appendix, the more general optimization problem of steady-state sequence synthesis is addressed. In addition to periodic variations in flip angle and phase, the synthesis algorithm allows variations in the sequence repetition time TR in a periodic manner, essentially varying the amount of precession per TR (as discussed in [16]. A general methodology for synthesizing oscillating steady-state sequences with magnetization profiles possessing some set of characteristics, as defined by an

objective function, is presented. A fast implementation of the approach is presented, and its performance analyzed with a simple test case.

A.2 Theory and Methods

Let α_n, ϕ_n, and TR_n denote the nth flip angle, flip phase, and TR respectively in an N-periodic oscillating equilibrium sequence ($n = 1...N$). Let $\mathbf{M_n}(\omega)$ denote the nth steady-state magnetization vector immediately prior to the subsequent excitation, where ω is the off-resonance frequency. Then

$$\mathbf{M_n}(\omega) = \mathbf{P_n}\mathbf{E_n}\mathbf{R_n}\mathbf{M_{n-1}} + (\mathbf{I} - \mathbf{E_n})\mathbf{M_0} \tag{A.1}$$

for $n = 1...N$, where $\mathbf{P_n}$ is the rotation matrix representing off-resonance precession, $\mathbf{E_n}$ is the exponential relaxation matrix, and $\mathbf{R_n}$ is the flip rotation matrix. $\mathbf{P_n}$, $\mathbf{E_n}$, and $\mathbf{R_n}$ are given by:

$$\mathbf{P_n} = \begin{bmatrix} \cos(\omega TR_n) & \sin(\omega TR_n) & 0 \\ -\sin(\omega TR_n) & \cos(\omega TR_n) & 0 \\ 0 & 0 & 1 \end{bmatrix} \tag{A.2}$$

$$\mathbf{E_n} = \begin{bmatrix} e^{-TR_n/T2} & 0 & 0 \\ 0 & e^{-TR_n/T2} & 0 \\ 0 & 0 & e^{-TR_n/T1} \end{bmatrix} \tag{A.3}$$

$$\mathbf{R_n} = \begin{bmatrix} \cos(\alpha_n)\sin^2(\phi_n) + \cos^2(\phi_n) & (1-\cos(\alpha_n))\cos(\phi_n)\sin(\phi_n) & -\sin(\alpha_n)\sin(\phi_n) \\ (1-\cos(\alpha_n))\cos(\phi_n)\sin(\phi_n) & \cos(\alpha_n)\cos^2(\phi_n) + \sin^2(\phi_n) & \sin(\alpha_n)\cos(\phi_n) \\ \sin(\alpha_n)\sin(\phi_n) & -\sin(\alpha_n)\cos(\phi_n) & \cos(\alpha_n) \end{bmatrix}. \tag{A.4}$$

As each magnetization vector $\mathbf{M_n}$ has three components, this is simply a set of $3N$ linear equations in $3N$ unknowns, and can be represented by a $3N$ by $3N + 1$ matrix

$\mathbf{A}$[1]. The coefficients are non-linear functions of the parameters α_n, ϕ_n, and TR_n. One can numerically solve for the steady states $\mathbf{M_n}(\omega)$ by diagonalizing $\mathbf{A}$ at a set of discrete values of ω across the frequency range of interest. Note that one matrix diagonalization is needed for each discrete value of ω. In order to make sequence optimization tractable, this matrix diagonalization must be done very rapidly. $\mathbf{A}$ is fortunately sparse and of very regular form. It can be diagonalized very rapidly using a Gauss-Jordan technique designed to minimize the number of floating point operations for matrices of the form $\mathbf{A}$.

Once equipped with the ability to rapidly evaluate $\mathbf{M_n}(\omega)$, a multidimensional minimization technique may be used to optimize the parameters α_n, ϕ_n, and TR_n. This requires the design of an objective function that compares a set of $\mathbf{M_n}(\omega)$ to a set of desired magnetization profiles $\mathbf{M_{n-ideal}}(\omega)$. Note that one is typically only interested in the projection of $\mathbf{M_n}(\omega)$ into the xy plane.

The design of this objective function is very flexible, and therein lies the potential power of SSFP sequence synthesis. One might be interested in matching only 1 of the N steady-state spectra to a desired profile, allowing the others to vary to give a better match. The objective function could be as simple as measuring the mean-squared error between the ideal and simulated signal magnitudes and/or phases across any of the N steady-state spectra for any range of off-resonance frequency. More complicated objective functions might perform a least squares fit of all N steady-state profiles to a single desired spectral profile and return the resultant error. A linear-combination oscillating equilibrium sequence might then be synthesized yielding a desired spectral profile.

As a test case, a sequence synthesis algorithm following the above framework was implemented in C++ on the Linux platform. The objective function was chosen to simply measure the mean-squared error between the synthesized and ideal signal

---

[1]The first 3N columns of $\mathbf{A}$ represent the coefficients of the components of $\mathbf{M_n}$, while the final column represents the non-coefficient scalars in the system of linear equations. Such a representation makes solution of the system of equations straightforward through diagonalization of the $3N$ by $3N$ portion of the matrix.

N	Diagonalization Rate (1000 / s)	Convergence to FEMR (s)
2	500	< 1
4	200	3
6	135	9
8	98	24
16	44	---

Table A.1: Performance of the diagonalization routine for $N = 2$, 4, 8, and 16, and overall sequence synthesis algorithm's convergence time to FEMR for $N = 2$, 4, and 8. On simple desktop hardware, optimization of $N = 16$ oscillating-equilibrium sequences becomes intractable. A single-processor AMD Athlon computer with 512 MB RAM was used for the tests.

magnitudes across a range of frequencies, ignoring the phase. Multidimensional minimization was done using a *Numerical Recipes in C++* implementation of Powell's method [49].

A.3   Results

The performance of the diagonalization routine was measured by determining how many diagonalizations of **A** the implementation could perform per second. This test was performed to gauge whether optimization would be tractable: if evaluation of the objective function is too time consuming, the complex optimization problem could require an unrealistic amount of time to converge. The diagonalization rates for N = 2, 4, 8, and 16 are shown in Table A.1.

As a test case, the desired signal profiles shown in Figure A.1(a) were used in the objective function, evaluated at 100 discrete values of ω. The algorithm was allowed to vary TR, but a minimum TR of π/ω_{max} was imposed. The reason for limiting the minimum TR was to test the algorithms convergence to the FEMR profile, shown in Figure A.1(b). If TR has a lower limit of π/ω_{max}, FEMR is the optimal solution (in the least squared error sense tested by the objective function) to the square profile

shown in Figure A.1(a). If, however, TR is allowed to vary below π/ω_{max}, other solutions can be found by reducing TR that are more optimal across the frequency range of interest (Figure A.1(c). These solutions are of limited practical interest, since the optimal FEMR TR at 1.5 Tesla is already a very low (and usually unattainable) 2.2 ms.

As expected, the optimization routine did converge to FEMR when the minimum TR limitation was imposed. Convergence to FEMR was verified for the $N = 2$, 4, and 8 cases[2]. The speeds of convergence are listed in Table A.1.

A.4   Conclusion

The synthesis of oscillating steady-state sequences using multidimensional optimization techniques appears to be tractable using modern desktop computers. In addition to flip angle and phase variations, periodic variations in TR can provide interesting spectral profiles. This technique is very flexible, and gives the optimization algorithm great latitude in choosing sequence parameters.

This appendix has demonstrated feasibility of the complex optimization method for small N. Future work on the appropriate design of objective function could yield new oscillating equilibrium SSFP sequences with novel and useful signal and/or phase profiles.

---

[2]While FEMR is simply a dual-equilibrium sequence ($N = 2$), any even-valued N may be used, with phase alternating between 0 and 90°.
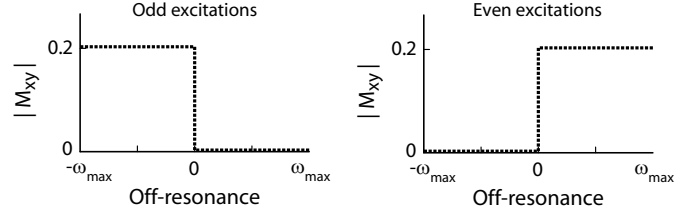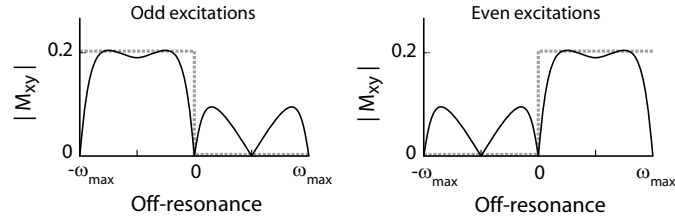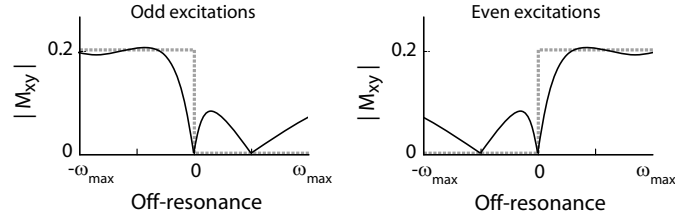
Figure A.1: (a) The ideal signal magnitude profile for sequence synthesis test case was designed to have a perfectly flat passband and stopband, each of width ω_{max}. (b) The FEMR magnitude profile is optimal in a least-squared error sense if the profile is required to be periodic with period $2\omega_{max}$. (c) If the period is not constrained to match the interval $[-\omega_{max}, \omega_{max}]$, other profiles more closely match the desired profile. However, these are of little practical interest.

Appendix B

SNR Measurement from Combination Images

Denote the mean signal of a region of interest (ROI) within an image by μ_{ROI}, and let σ_{ROI} denote the standard deviation of the signal in that region. The SNR within the region is then given by:

$$SNR_{ROI} \equiv \frac{\mu_{ROI}}{\sigma_{ROI}}. \tag{B.1}$$

The following procedure is commonly used to empirically measure SNR in magnitude images. First, the average signal over the ROI is measured, giving μ_{ROI}. A region is then chosen in the background (i.e., in a region where no signal is expected from the body) and the standard deviation σ_{BG} measured. It is tempting to simply assume that $\sigma_{BG} = \sigma_{ROI}$ and conclude that SNR_{ROI} is given by μ_{ROI}/σ_{BG}. However, this is actually incorrect and overstates the true SNR_{ROI}, as explained below.

Prior to the magnitude operation, pixels in the background are expected to be zero mean bivariate Gaussian in distribution, with a standard deviation we define as σ_0. Following the magnitude operation, the noise is no longer zero mean, and the bivariate Gaussian distribution becomes a univariate Rayleigh distribution with standard deviation $\sigma_{BG} = \sqrt{2 - \frac{\pi}{2}} \cdot \sigma_0 \approx 0.6551 \cdot \sigma_0$.

What about the noise in the region of interest? Prior to the magnitude operation, pixels in the ROI are also bivariate Gaussian in distribution with standard deviation σ_0, but are not zero mean. The magnitude operation in this case transforms the bivariate Gaussian distribution into a univariate Rician distribution. If μ_{ROI} is large with respect to σ_0, the Rician distribution can be approximated by a univariate Gaussian distribution with standard deviation

$$\sigma_{ROI} \approx \sigma_0 = \frac{\sigma_{BG}}{\sqrt{2 - \frac{\pi}{2}}}. \tag{B.2}$$

It then follows that:

$$SNR_{ROI} = \frac{\mu_{ROI}}{\sigma_{ROI}} \approx \frac{\sqrt{2 - \frac{\pi}{2}} \cdot \mu_{ROI}}{\sigma_{BG}}. \tag{B.3}$$

The correction factor $\sqrt{2 - \frac{\pi}{2}} \approx 0.6551$ applied to an SNR measurement on a simple magnitude image is also approximately correct when applied to a CS-SSFP image. However, the situation is more complex with MI-SSFP or SOS-SSFP images.

Consider the random variables Y_{MI} and Y_{SOS} defined in Equations 4.6 and 4.7, which describe the statistics of a reconstructed voxel in MI-SSFP and SOS-SSFP respectively. Given the nature of maximum-intensity and sum-of-squares combination, the standard deviations of Y_{MI} and Y_{SOS} will be functions of the voxel's local off-resonance free-precession angle β. The relationship between σ_{BG} and σ_{ROI} is therefore not a simple constant, and the SNR of a voxel will vary with β.

We can, however, perform an analysis analogous to the one presented in the SNR analysis section to determine σ_{BG} in either the MI or SOS case. Armed with this information, and assuming that our region of interest contains a uniform distribution of values of β, we can define an average correction factor CF. Let Y represent either Y_{MI} or Y_{SSFP}. Then

$$CF = \frac{\langle SNR_Y \rangle}{\langle \frac{\mu_Y}{\sigma_{BG}} \rangle}, \tag{B.4}$$

where all averages are across β, $\langle SNR_Y \rangle$ denotes average predicted SNR, and μ_Y and σ_Y denote the mean and variance of Y respectively.

The correction factor CF can be used to approximately correct SNR measurements of a given tissue for maximum-intensity and sum-of-squares SSFP images. That is,

$$SNR_{ROI} \approx CF \cdot \frac{\mu_{ROI}}{\sigma_{BG}}. \tag{B.5}$$

Bibliography

[1] Liang ZP, Lauterbur PC, "Principles of Magnetic Resonance Imaging: A Signal Processing Perspective". Wiley-IEEE Computer Society PR, 1st ed., 1999.

[2] Haacke EM, Brown RW, Thompson MR, Venkatesan R, "Magnetic Resonance Imaging: Physical Principles and Sequence Design". John Wiley and Sons, 1st ed., 1999.

[3] Nishimura D. Principles of magnetic resonance imaging. Stanford University EE369B Course Notes, 1996.

[4] Hargreaves BA, Vasanawala SS, Nayak KS, Hu BS, Nishimura DG. Fat-suppressed steady-state free precession imaging using phase detection. Magn Reson Med 2003; 50:210.

[5] Vasanawala SS, Hargreaves BA, Nayak KS, Gold GE, Pauly JM, Nishimura DG. Musculoskeletal imaging with phase-sensitive SSFP. In: Proceedings of the 11th Annual Meeting of ISMRM, Toronto, 2003. Accepted.

[6] Miller KL, de Charms RC, Lee J, Ress D, Hargreaves BA, Pauly JM. Functional brain imaging using a blood oxygenation sensitive steady-state. Magn Reson Med 2003; 50:675.

[7] Deimling M, Heid O. Magnetization prepared True FISP imaging. In: Proceedings of the 2nd Annual Meeting of SMR, San Francisco, 1994. p. 495.

[8] Nishimura DG, Vasanawala SS. Analysis and reduction of the transient response in SSFP imaging. In: Proceedings of the 8th Annual Meeting of ISMRM, Denver, 2000. p. 301.

[9] Hargreaves BA, Vasanawala SS, Pauly JM, Nishimura DG. Characterization and reduction of the transient response in steady-state MR imaging. Magn Reson Med 2001; 46:149.

[10] Huang TY, Huang IJ, Chen CY, Scheffler K, Chung HW, Cheng HC. Are True-FISP images T2/T1-weighted? Magn Reson Med 2002; 48:684.

[11] Vasanawala SS, Pauly JM, Nishimura DG. Fluctuating equilibrium MRI. Magn Reson Med 1999; 42:876.

[12] Gold GE, Hargreaves BA, Shimakawa A, Vasanwawala S, Castillo V, Brittain J, Nishimura D, Beaulieu C. High resolution imaging of articular cartilage with FEMR. In: Proceedings of the 10th Annual Meeting of ISMRM, Honolulu, 2002. p. 1865.

[13] Vasanawala SS, Pauly JM, Nishimura DG, Gold GE. MR imaging of knee cartilage with FEMR. Skeletal Radiol 2002; 31:574.

[14] Vasanawala SS, Gold GE, Pauly JM, Nishimura DG. Rapid high resolution cartilage imaging with FEMR. In: Proceedings of the 9th Annual Meeting of ISMRM, Glasgow, 2001. p. 82.

[15] Overall WR, Conolly SM, Nishimura DG, Hu BS. Oscillating dual-equilibrium steady-state angiography. Magn Reson Med 2002; 47:513.

[16] Overall WR, Nishimura DG, Hu BS. Steady-state sequence synthesis and its applications to efficient fat-suppressed imaging. Magn Reson Med 2003; 50:550.

[17] Carr HY. Steady-state free precession in nuclear magnetic resonance. Phys Rev 1958; 112:1693.

[18] Freeman R, Hill HDW. Phase and intensity anomalies in Fourier transform NMR. J Magn Reson 1971; 4:366.

[19] Schwenk A. NMR pulse techniques with high sensitivity for slowly relaxing systems. J Magn Reson 1971; 5:376.

[20] Oppelt A, Graumann R, Barfuss H, Fischer H, Hartl W, Shajor W. FISP – a new fast MRI sequence. Electromedica 1986; 54:15.

[21] Zur Y, Stokar S, Bendel P. An analysis of fast imaging sequences with steady-state transverse magnetization refocusing. Magn Reson Med 1988; 6:175.

[22] Haacke EM, Wielopolski PA, Tkach JA, Modic MT. Steady-state free precession imaging in the presence of motion: Application for improved visualization of the cerebrospinal fluid. Radiology 1990; 175:545.

[23] Zur Y, Wood ML, Neuringer LJ. Motion-insensitive, steady-state free precession imaging. Magn Reson Med 1990; 16:444.

[24] Duerk JL, Lewin JS, Wendt M, Petersilge C. Remember true FISP? a high SNR near 1-second imaging method for T_2-like contrast in interventional MRI at .2 T. J Magn Reson Imaging 1998; 8:203.

[25] Vasanawala SS, Pauly JM, Nishimura DG. Linear combination steady-state free precession MRI. Magn Reson Med 2000; 43:82.

[26] Foxall DL. Frequency-modulated steady-state free precession imaging. Magn Reson Med 2002; 48:502.

[27] Scheffler K, Heid O, Hennig J. Magnetization preparation during the steady-state: Fat-saturated 3D true FISP. Magn Reson Med 2001; 45:1075.

[28] Bangerter NK, Vasanawala SS, Nishimura DG. SNR analysis of multiple acquisition SSFP. In: Proceedings of the 10th Annual Meeting of ISMRM, Honolulu, 2002. p. 475.

[29] Roemer PB, Edelstein WA, Hayes CE, Souza SP, Mueller OM. The NMR phased array. Magn Reson Med 1990; 16:192.

[30] Buxton RB, Fisel CR, Chien D, Brady TJ. Signal intensity in fast NMR imaging with short repetition times. J Magn Reson 1989; 83:576.

[31] Bangerter NK, Vasanawala SS, Nishimura DG. Fluid-attenuated SSFP imaging. In: Proceedings of the 9th Annual Meeting of ISMRM, Glasgow, 2001. p. 1780.

[32] Stucker DT, Bangerter NK, Nishimura DG, Lane B, Gold GE. SSFP FLAIR imaging: Comparison with FSE FLAIR in normal brain. In: Proceedings of the 10th Annual Meeting of ISMRM, Honolulu, 2002. p. 2358.

[33] Rydberg JN, Riederer SJ, Rydberg CH, Jack CR. Contrast optimization of fluid-attenuated inversion recovery (FLAIR) imaging. Magn Reson Med 1995; 34:868.

[34] DeCoene B, Hajnal JV, Gatehouse P. MR of the brain using fluid-attenuated inversion recovery (FLAIR) pulse sequences. AJNR 1992; 13:1555.

[35] Scheffler K, Hennig J. T_1 quantification with inversion recovery TrueFISP. Magn Reson Med 2001; 45:720.

[36] Shea SM, Deshpande VS, Chung YC, Li D. Three-dimensional True-FISP imaging of the coronary arteries: Improved contrast with T2-preparation. J Magn Reson Imaging 2002; 15:597.

[37] Deshpande VS, Shea SM, Laub G, Simonetti OP, Finn JP, Li D. 3D magnetization-prepared True-FISP: A new technique for imaging coronary arteries. Magn Reson Med 2001; 46:494.

[38] Larsson HBW, Frederiksen J, Kjaer L, Henriksen O, Olesen J. *In Vivo* determination of T1 and T2 in the brain of patients with severe but stable multiple sclerosis. Magn Reson Med 1988; 7:43.

[39] Bangerter N, Hargreaves B, Nishimura D. General framework for the SNR analysis of multiple-acquisition SSFP. In: Proceedings of the 11th Annual Meeting of ISMRM, Toronto, 2003. p. 995.

[40] Pauly J, Le Roux P, Nishimura D, Macovski A. Parameter relations for the Shinnar-Le Roux selective excitation pulse design algorithm. IEEE Trans Med Imaging 1991; 10:53.

[41] Brittain JH, Hu BS, Wright GA, Meyer CH, Macovski A, Nishimura DG. Coronary angiography with magnetization-prepared T_2 contrast. Magn Reson Med 1995; 33:689.

[42] Brittain JH, Olcott EW, Szuba A, Gold GE, Wright GA, Irarrazaval P, Nishimura DG. Three-dimensional flow-independent peripheral angiography. Magn Reson Med 1997; 38:343.

[43] Wright GA, Hu BS, Macovski A. 1991 i.i. rabi award. estimating oxygen saturation of blood in vivo with MR imaging at 1.5 T. J Magn Reson Imaging 1991; 1:275.

[44] Gronas R, Kalman PG, Kucey DS, Wright GA. Flow-independent angiography for peripheral vascular disease: Initial *in vivo* results. J Magn Reson Imaging 1997; 7:637.

[45] Brittain JH, Shimakawa A, Wright GA, Hargreaves BA, Han E, Stainsby JA, Hu BS. Non-contrast-enhanced flow-independent, 3D peripheral angiography using steady-state free precession at 3T. In: Proceedings of the 11th Annual Meeting of ISMRM, Toronto, 2003. p. 1801.

[46] Korin HW, Riederer SJ, Bampton AEH, Ehman RL. Altered phase encoding order for reduced sensitivity to motion corruption in 3DFT MR imaging. J Magn Reson Imaging 1992; 2:687.

[47] Wilman AH, Riederer SJ. Improved centric phase encoding orders for three-dimensional magnetization-prepared MR angiography. Magn Reson Med 1996; 36:384.

[48] Ward HA, Polzin JA, Bernstein MA, Hoppel BE. In/out elliptic centric view ordering and modulated phase-cycling for reduced motion artifact in phase-cycled ssfp. In: Proceedings of the 11th Annual Meeting of ISMRM, Toronto, 2003. Accepted.

[49] Press WH, Teukolsky SA, Vetterling WT, Flannery BP, "Numerical Recipes in C++". Cambridge University Press, New York, NY, 2nd ed., 2002.